Karlsruher Institut für Technologie

Superradiant Terahertz Sources and their Applications in Accelerator Diagnostics and Ultra-fast Science

Zur Erlangung des akademischen Grades eines
DOKTORS DER NATURWISSENSCHAFTEN
von der Fakultät für Physik
des Karlsruher Institutes für Technologie (KIT)
genehmigte Dissertation
von

Bertram Green

Erstgutachter:	Prof. Dr. Anke-Susanne Müller
Zweitgutachter:	Prof. Dr. Thomas Cowan
Betreuender Mitarbeiter:	Dr. Michael Gensch

Tag der mündlichen Prüfung: 28 April 2017

Part of this thesis is based on the following publications:

1. Peer reviewed journal articles:

S. Kovalev, B. Green, T. Golz, N. Stojanovic, A. S. Fisher, T. Kampfrath, M. Gensch. Probing ultra-fast processes with high dynamic range at 4th generation lightsources. *Struct. Dynam.*, 4:024031, 2017

N. Awari, S. Kovalev, C. Fowley, K. Rode, R. A. Gallardo, Y.-C. Lau, D. Betto, N. Thiyagarajah, B. Green, O. Yildirim, J. Lindner, J. Fassbender, J. M. D. Coey, A. M. Deac, M. Gensch. Narrow-band tunable terahertz emission from ferrimagnetic Mn(3-x)Ga thin films. *Appl. Phys. Lett.*, 109:032403, 2016

B. Green, S. Kovalev, V. Asgekar, G. Geloni, U. Lehnert, T. Golz, M. Kuntzsch, C. Bauer, J. Hauser, J. Voigtlaender, B. Wustmann, I. Koesterke, M. Schwarz, M. Freitag, A. Arnold, J. Teichert, M. Justus, W. Seidel, C. Ilgner, N. Awari, D. Nicoletti, S. Kaiser, Y. Laplace, S. Rajasekaran, L. Zhang, S. Winnerl, H. Schneider, G. Schay, I. Lorincz, A. A. Rauscher, I. Radu, S. Mährlein, T. H. Kim, J. S. Lee, T. Kampfrath, S. Wall, J. Heberle, A. Malnasi-Csizmadia, A. Steiger, A. S. Müller, M. Helm, U. Schramm, T. Cowan, P. Michel, A. Cavalleri, A. S. Fisher, N. Stojanovic, M. Gensch. High-Field High-Repetition-Rate Sources for the Coherent THz Control of Matter. *Sci. Rep.*, 6:22256, 2016

T. A. Miller, R. W. Chajlany, L. Tagliacozzo, B. Green, S. Kovalev, D. Prabhakaran, M. Lewenstein, M. Gensch, S. Wall. Terahertz field control of in-plane orbital order in La0.5Sr1.5MnO4. *Nat. Comm.*, 6:8175, 2015

F. Kuschewski, S. C. Kehr, B. Green, C. Bauer, M. Gensch, L. M. Eng. Optical nanoscopy of transient states in condensed matter. *Sci. Rep.*, 5:12582, 2015

2. Selected conference proceedings:

S. Kovalev, B. Green, M. Gensch. (2015) Super-radiant High-field THz Sources Operating at Quasi-CW Repetition Rates. *Proceedings of SPIE Vol. 9512*, Advances in X-ray Free-Electron Lasers Instrumentation III, 95121F, Prague, Czech Republic

M. Gensch, B. Green, S. Kovalev, M. Kuntzsch, J. Hauser, R. Schurig, U. Lehnert, P. Michel, A. Al-Shemmary, V. Asgekar, T. Golz, S. Vilcins, H. Schlarb, N. Stojanovic, A. S. Fisher, M. Schwarz, A.-S. Müller, N. Neumann, D. Plettemeier, G. A. Geloni. (2014) THz Facility at ELBE: A Versatile Test Facility for Electron

Bunch Diagnostics on Quasi-CW Electron Beams. *Proceedings of IPAC2014*. 933:934 Dresden, Germany

N. Neumann, M. Laabs, M. Schiselski, D. Plettemeier, B. Green, S. Kovalev, M. Gensch. (2014) Compact Integrated THz Spectrometer in GaAs Technology for Electron Compression Monitor. *Proceedings of IPAC2014,* 3489:3491 Dresden, Germany

Contents

Chapter 1

Introduction

The terahertz (THz) frequency range lies between the frequency range of radio and infrared. The exact limits are not well defined and depend on the scientific community. The most recent "2017 Terahertz Science and Technology Roadmap" sets the THz frequency range to between 0.1 and 30 THz [1]. The development of suitable detectors, detection techniques, and sources for this frequency range has seen tremendous progress over the past decade [1]. The arrival of commercial femtosecond (fs) laser systems has enabled new, background-free THz time domain spectroscopy [2], and both laser-driven and accelerator-driven THz sources are currently producing pulse energies in the μJ, and even mJ, range [3] [4] [5]. This thesis describes the characterization of a new class of accelerator-based light sources, which open up opportunities to provide a unique combination of high pulse energies and high repetition rates. The foreseen applications of these types of sources, coined "superradiant THz sources", lie in the area of time-resolved (nonlinear) spectroscopy [6]. One of the first results of this thesis is the observation that the THz pulses from the prototype facility TELBE exhibit large pulse-to-pulse fluctuations in arrivaltime and intensity. These types of instabilities render the intended applications of TELBE for real-world nonlinear THz spectroscopy experiments impossible. As part of this thesis a pulse resolved data acquisition and analysis scheme has therefore been devised which enables the correction of these instabilities and now allows performance of time-resolved THz spectroscopy measurements with sub-30 femtosecond (fs) (FHWM) time resolution with excellent dynamic range up to 10^6 [7].

The thesis is organized as follows: the first chapter introduces the fundamental principles and techniques utilized in this work. The second chapter presents the results, starting with the diagnostic developments, followed by a thorough characterization of the THz source properties and ending with the presentation of two benchmark THz-pump laser-probe experiments. After summarizing the results, foreseeable future development and upgrades, e.g. towards sub-1-fs resolution, are discussed. It should be noted that the techniques developed within the framework of this thesis have been in continuous use since July 2016 in friendly user experiments at the TELBE facility.

Chapter 2

Basics and Methods

2.1 SRF electron accelerators

Superconducting radio frequency (SRF) accelerators make use of accelerator cavities that are manufactured from superconducting materials, most commonly pure niobium [8]. This material is generally preferred over other, higher T_c (critical temperature) materials because it is important to reduce flux pinning. This helps the cavity achieve a high-quality internal RF field [8]. In comparison to normal-conducting accelerator cavities, most commonly from pure copper, these superconducting cavities have a much higher quality factor, also known as a Q value. The Q value is defined as:

$$Q = \frac{\omega U}{P} \tag{2.1}$$

where ω is the angular frequency of radio frequency (RF) power ($\omega = 2\pi f$), U is the energy stored in the cavity, and P is the power dissipated in the cavity walls [9]. The Q value is a dimensionless number used to describe how under-damped an oscillator is. In terms of accelerator cavities it describes how much power from the driving AC electric field is lost in the cavity walls. A standard pure copper RF cavity has a Q value of 17000-20000, and a niobium superconducting cavity has a Q value on the order of 10^{10} [10], which means energy loss within the cavities is about 6 orders of magnitude lower. Figure 2.1 a shows a typical layout for an SRF accelerator being utilized as a THz light source driver. Bunches of electrons are generated in the electron injector, accelerated to relativistic energies, then compressed into sub-ps long bunches and passed through various light generating beam elements, in this case a coherent diffraction screen and an undulator. SRF accelerators are capable, because of the high Q value, of going to much higher repetition rates than normal-conducting accelerators. The high repetition rate is one of the main advantages of SRF technology. For superradiant THz sources based on SRF technology this means that new types of repetition-rate-hungry experiments, such as pump-probe experiments, are made possible. As shown in Figure 2.1.b, the TELBE facility exceeds all other existing THz sources in its performance for repetition rates beyond 10 kHz.

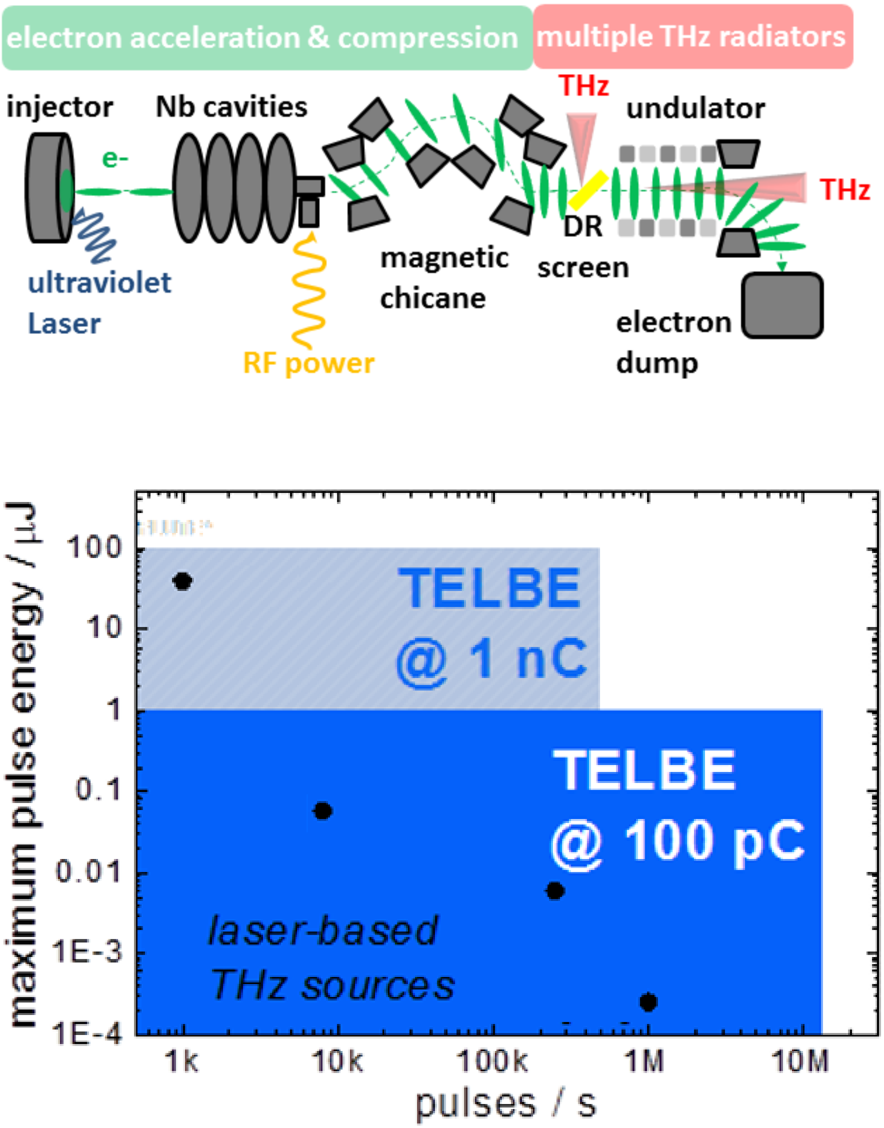

(a)

(b)

Figure 2.1: (a) Schematic of a compact SRF accelerator-driven THz source and comparison of pulse energies with record pulse energies of laser-driven sources. Electron bunches are extracted from a solid, accelerated to relativistic energies and compressed to sub-ps duration in a compact SRF linac with a chicane bunch compressor. The electron bunches can emit THz pulses in different types of radiators. At TELBE, repetition rates up to 13 MHz are feasible. THz pulses are generated by a diffraction radiator (DR) and one undulator. (b) Comparison between laser-based sources (black dots) and TELBE. Laser-based sources operating higher than 10 kHz repetition rate are limited to pulse energies <10 nJ, at repetition rates above 250 kHz to <0.25 nJ. TELBE currently exceeds these values by more than 2 orders of magnitude (blue-shaded). The high charge mode of operation will enable pulse energies of 100 μJ (light-blue-shaded). Taken from [6].

2.1.1 Advantages over normal-conducting accelerators

A high Q value means low losses in the cavity walls, which means less heat is generated. This leads to the ability to run at higher repetition rates, or even generate continuous-wave bunch trains. Copper accelerating cavities would generate too much heat to run in continuous wave (cw) mode, even with a robust cooling system in place. For this reason they are generally run at lower duty cycles [11]. This means that a light source driven by SRF accelerators is able to run at a higher duty cycle than one driven by a normal conducting accelerator. Superradiant THz sources based on SRF technology can also generate orders of magnitude higher repetition rates than any tabletop laser-based source [6] (see Figure 2.1). This is especially useful for repetition-rate hungry techniques, such as pump-probe experiments. Quasi-cw repetition rates also facilitate more efficient schemes in accelerator control and more advanced feedbacks, as there are no long pauses between bunches. When such feedbacks are implemented it allows the electron bunches to effectively see an accelerator that is essentially in a quasi-equilibrium state [12]. Synchronization by beam-based feedbacks to a sub-100 fs (FWHM) level has recently been demonstrated at the FLASH FEL [13].

2.1.2 Challenges

Despite these advantages, SRF accelerating cavities do have some challenges to consider compared to traditional copper cavities. For instance, the superconducting material must be kept at cryogenic temperatures, which requires expensive infrastructure to handle the liquid helium. Furthermore, the cavities must be very clean on the inside, as any particles and remnant gas in the chamber can ionize and can hit the cavity wall, which can lead to damage in the superconducting layer. This can cause flaws which will warp or destroy the accelerating field. Also, Niobium superconductors can only support small accelerating gradients compared to copper because of the relatively low critical field [8] [14]. Because of the high repetition rates, the data generated in even a short time can easily be in the terabyte (TB) range, creating challenges in data acquisition, handling, storage, and analysis. Specialized systems are required to be able to read and store data at high data rates, including both hardware and software. Finally, on the accelerator end, the high-repetition quasi-cw nature of the electron beam means that there is a high current that can damage beamline components very quickly. This requires a fast machine interlock system to prevent damage upon detection of beam loss.

2.1.3 The ELBE compact superconducting accelerator

The *Electron Linac for beams with high Brilliance and low Emittance* (ELBE) superconducting radiofrequency (SRF) accelerator [15] is a facility at the Helmholtz-Zentrum Dresden-Rossendorf. It was built to be a driver for various secondary radiation sources, which currently includes an FEL (FELBE) [16], positron sources (pELBE) [17], neutron sources (nELBE) [18], Compton scattering (γELBE) [19], and superradiant THz sources (TELBE) [6]. The current layout of the ELBE - Center for High Power Radiation Sources is shown in Figure 2.2. ELBE is operated on a 24/7 schedule as a user facility, with users from all over the world utilizing the facility. The SRF technology used in its design makes it capable of high repetition rate quasi-cw operation. The main electron beam driving the light sources has a maximum energy of 40 MeV and a maximum current of 1.6 mA. Depending on the mode of operation required there are two available injectors in use at the ELBE. The first is the thermionic injector, which is used for regular operating modes and supports repetition rates up to 13 MHz and bunch charges up to 100 pC. The second is the SRF photocathode injector, which shall be used for experiments that may require lower emittance or higher bunch charges of up to 1 nC [15]. It has a maximum repetition rate of 13 MHz which can be adjusted to lower rates if desired, also including different macropulse modes of operation. The SRF injector, however, was not available for operation during the course of this work. The typical repetition rate for the operation of the TELBE facility is currently 101 kHz, which is the 128th division of the base 13 MHz repetition rate. A diagram showing the relative positions of the sources and the TELBE lab is shown in Figure 2.3, as well as a diagram of the lab itself with the positions of the various endstations shown.

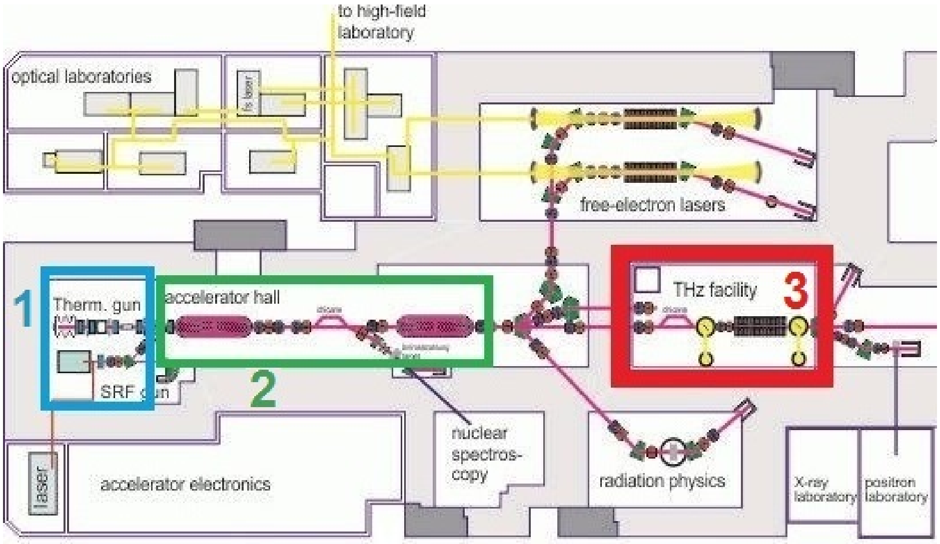

Figure 2.2: Layout of the superconducting electron accelerator facility ELBE. Area 1 (blue) shows the two electron injectors, the thermionic and the SRF. Either injector can provide electrons and are chosen based on the desired electron bunch properties. Area 2 (green) is the location of the superconducting accelerator cavities, where the electrons are boosted to the required energy of up to 40 MeV. The second cavity can also be used to compress the bunches if so desired. Area 3 (red) are the TELBE sources, with the coherent diffraction radiator source coming before the undulator in the direction of electron travel. Two beamlines direct the emitted THz radiation into the TELBE lab above the generation hall [20].

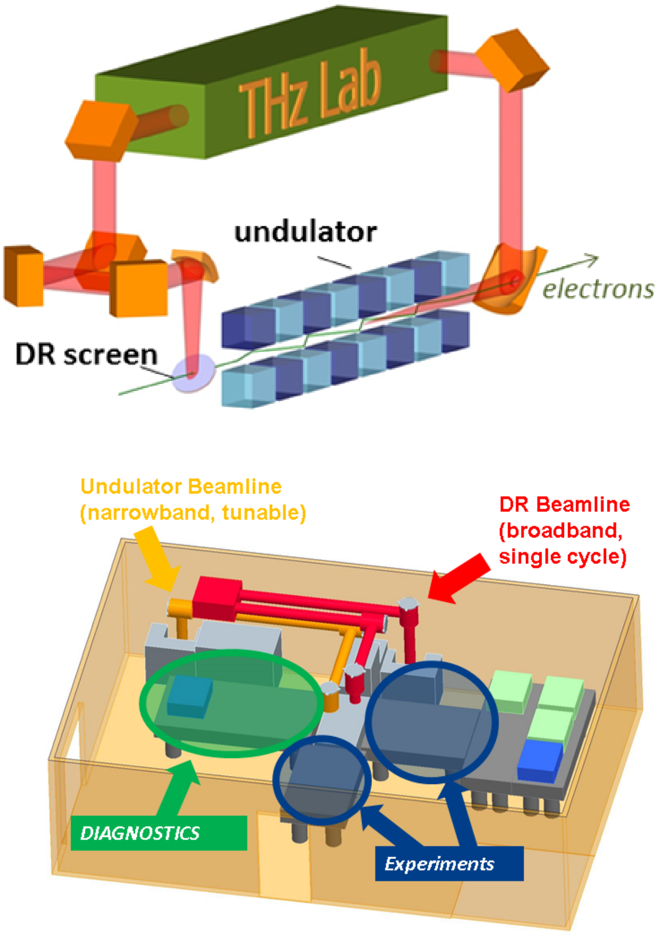

(a)

(b)

Figure 2.3: (a) Diagram of the layout of the superradiant THz sources. The beamlines lead upward from the generation hall to the lab, which is positioned above the generation area. The electrons first pass through the CDR screen, then continue on into the undulator. This allows both sources to be run in parallel. (b) Layout of the TELBE lab, showing the incoming THz undulator (orange) and CDR (red) beamlines, as well as the diagnostics table and the two user experiment tables. The CDR beamline is laid out in such a way as to have the CDR pulses arrive at the same time as the undulator pulses by adding an extension to the beampipe, because the CDR pulses are generated first. The box on the left at the turn around point is a mechanical delay stage. The table to the far right holds the fs-laser system.

2.1.4 Instabilities

Bunch charge and beam energy

Instabilities in beam and/or bunch parameters, such as bunch charge or beam energy, can be the source of noise in the various secondary sources driven by the electron beam. There are many possible origins for these instabilities and it can be difficult because of this to determine the exact causes. Some types of instabilities can originate in the injector. In the case of the thermionic injector, for example, instabilities in the buncher can cause variations in the bunch charge. Other instabilities, such as beam energy, can be caused by changes in, for instance, the phase or amplitude of the accelerating field in the RF cavities. Figure 2.4 shows a measurement of the stability of the high voltage power source that drives the thermionic injector at ELBE [21]. This power supply provides high-voltage DC at 235 kV to the thermionic injector which is used to pull electrons from a barium cathode (CPI EIMAC Y-845 Dispenser Cathode Assembly [22]) [23]. The observed changes in this voltage can cause changes in the current of the electron beam provided to the buncher, which could affect the bunch charge. Beam energy is also likely affected, but because of the small relative change (±500 V in a 235 kV DC potential, or about 0.2%) any possible instabilities would be difficult to detect [24]. Bunch charge fluctuations lead to intensity instabilities in the superradiant THz sources. Instabilities in the beam energy would, among other things, affect the superradiant THz spectrum (e.g. the center frequency of the undulator radiation). As part of this work a pulse-resolved intensity measurement has been developed that allows for correction of intensity instabilities.

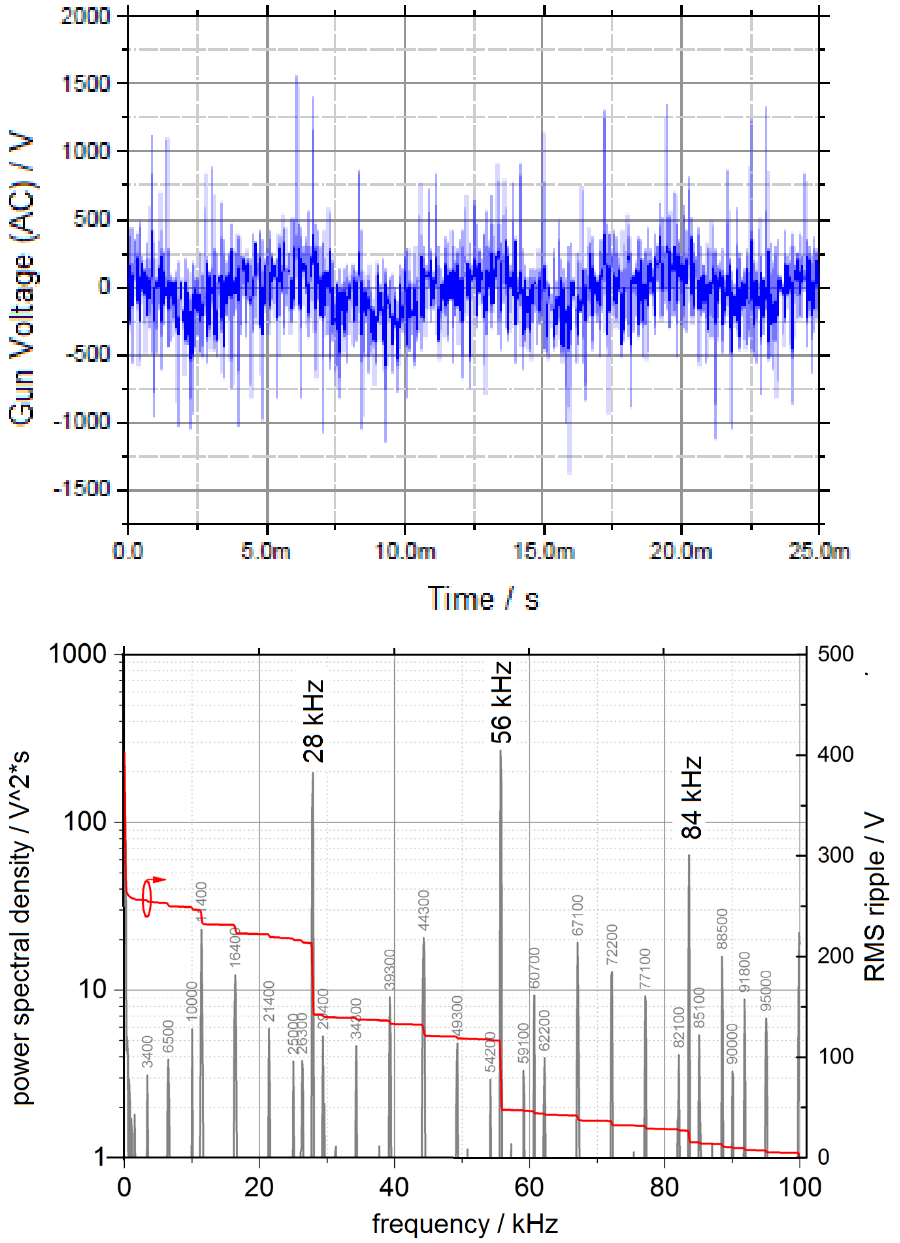

(a)

(b)

Figure 2.4: (a) Measurement of fluctuations in the high-voltage power supply of the thermionic injector at the ELBE accelerator, for a period of 25 ms. (b) Spectral density of power fluctuations, with the integration for determining the RMS value of the fluctuations. This power supply operated at a nominally stable voltage of 235 kV. These plots show the AC instabilities in the supplied voltage. This type of instability can cause fluctuations in the electron beam energy and bunch charge when the thermionic injector is in use by causing small variations in the electron beam current that the injector provides before it is separated into bunches. Ripple is any unwanted periodic change in a DC electric field, and the integral shows the amplitude of each frequency component contributes to this. Data was taken with a Rohde and Schwarz FSUP26 Signal Source Analyzer [21] [24].

Arrivaltime

The arrivaltime of radiation pulses is a critical value to know for the time-resolved experiments in this work. It is important to keep in mind, then, that accelerator driven radiation sources suffer from arrivaltime instabilities that make it difficult to perform time-resolved measurements without first accounting for this. One differentiates between two timescales of the instability here, to be known from here on as jitter and drift. Jitter is defined as pulse-to-pulse changes in arrivaltime on timescales of less than 1 second. Drift is defined as variations on longer time scales of more than 1 second. Currently the jitter at ELBE is in the few picosedonds (ps) (FWHM) range, and the drift over long periods of a day or more is on the few 10 ps (FWHM) range. One possible source of this type of instability is the actual arrivaltime of the electron bunch. If there are any instabilities in the timing system used to inject the electrons it would show up as this type of jitter. Jitter that is present at this point will be present at every location downstream in the accelerator. After that there are the instabilities in the RF sources, which are either klystrons or, in newer generations of machines such as the ELBE, solid-state RF sources [25]. Changes in phase of the accelerating field within the accelerator cavities lead to fluctuations in beam energy. Fluctuations in beam energy can translate into arrivaltime differences in all dispersive elements of the accelerator. Finally, changes in temperature and humidity can affect how accurately the timing and clock signal is distributed to external systems, such as the lasers which are used in the TELBE lab. Any jitter between these external systems and the accelerator master clock will also show up as timing jitter in any experiment which involves both of those systems working in concert. As a part of this work, a pulse-resolved arrivaltime monitor has been developed to measure and correct the arrivaltime value on a timescale of 30 fs (FWHM).

Beam position

Changes in the position of the electron bunches within the accelerator can be caused by instabilities of the magnetic fields in various beamline components, such as sleeves, dipole, or quadrupole magnets. Instabilities in beam position can affect the performance of certain secondary radiation sources, such as the diffraction radiator, of the TELBE facility. Figure 2.5 shows the spectral components of a measurement of beam position jitter in the ELBE accelerator. The measurement was taken at a position between the two main accelerator modules with the beam at this point having an energy of 12 MeV. The detector was a commercial beam position monitor from Libera, called the Spark [26]. The data was taken on individual bunches at 400 Hz, with the beam having a repetition rate of 1.625 MHz. The beam was shown to move more in the x direction, with a movement FWHM of 149.4 μm as compared to a movement FWHM of 51.4 μm in the y direction. Beam position shifts may result in an increase in intensity from the diffraction radiator source, due to the emission of transition radiation [27] caused by electrons impinging on the diffraction screen. This causes an observable increase in overall intensity and high-frequency spectral content.

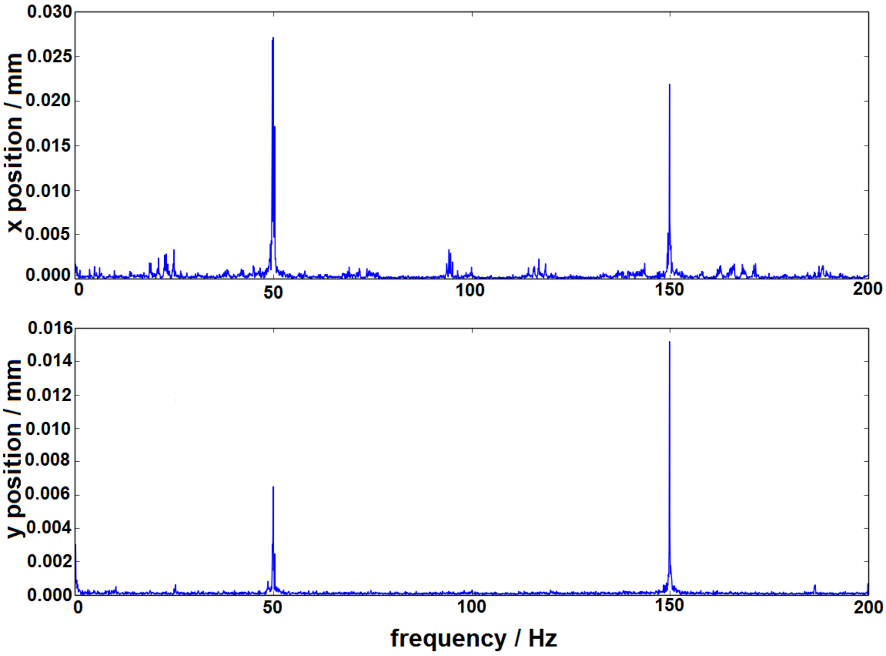

Figure 2.5: Spectrum of beam position changes measured at ELBE with a Libera Spark beam position monitor positioned between the two main accelerating modules of the accelerator. The top plot shows the changes in the horizontal position, with an FWHM of 149.4 μm, and the bottom plot shows the vertical jitter, with a FWHM of 51.4 μm jitter. Data taken with a beam energy of 12 MeV (total beam energy was 34 MeV, but data was taken after only the first accelerator module so the beam measured was at 12 MeV), bunch charge of 46 pC, using the thermionic injector, at a repetition rate of 1.625 MHz [28].

2.2 Superradiant THz sources

2.2.1 Superradiant principle

The superradiant principle states that the intensity of radiation from emitters increases as the square of the number of emitters, I $\propto$ (number of emitters)^2, for certain cases. The requirement is that the area the emitters radiate from must be sufficiently small compared to the wavelength of the emitted radiation [29]. For example, a bunch of electrons emitting in phase less than 300 microns from each other will have extremely enhanced emissions for wavelengths below 1 THz. This can be described as shown:

$$W_{bunch} = \left[(1-f)N_{electron} + fN_{electron}^2\right] W_{electron} \tag{2.2}$$

where N is the number of emitters (in this case electrons), $W_{electron}$ is the emission of a single electron, and f is known as the formfactor, here shown for an electron bunch with a Gaussian density distribution:

$$f(\nu) = e^{-0.5(2\pi\nu)^2(\frac{\tau}{2.35})^2} \tag{2.3}$$

where ν is the wavelength and τ is the FWHM (full width half max) of the bunch density distribution. This basic principle is what allows electron accelerator driven light sources to act as high-intensity, high repetition rate light sources given the electron bunches can be compressed to sufficiently short durations [6]. Once the bunches are short and highly charged any radiator type can be utilized, and hence an enormous variety of pulse forms can be generated. An illustration of the changes to the formfactor for various electron bunch lengths is shown in Figure 2.6.

2.2.2 Radiator types

Transition Radiation

Transition radiation was first theoretically described by V. L. Ginzburg and I. Frank in 1945 [30]. This is the radiation that is emitted when a charged particle travels between two materials with differing dielectric constants. The following equation analytically describes the intensity distribution of transition radiation on a detector screen:

$$\frac{d^2U}{d\omega d\Omega} = \frac{e^2}{4\pi^3\epsilon_0 c} \cdot \frac{\beta^2 \sin^2\theta}{(1-\beta^2\cos^2\theta)^2} \tag{2.4}$$

where e is electron charge, ϵ_0 is the dielectric constant in vacuum, β is the ratio of the speed of a particle to the speed of light ($\beta = \frac{v}{c}$), and θ is the angle from the

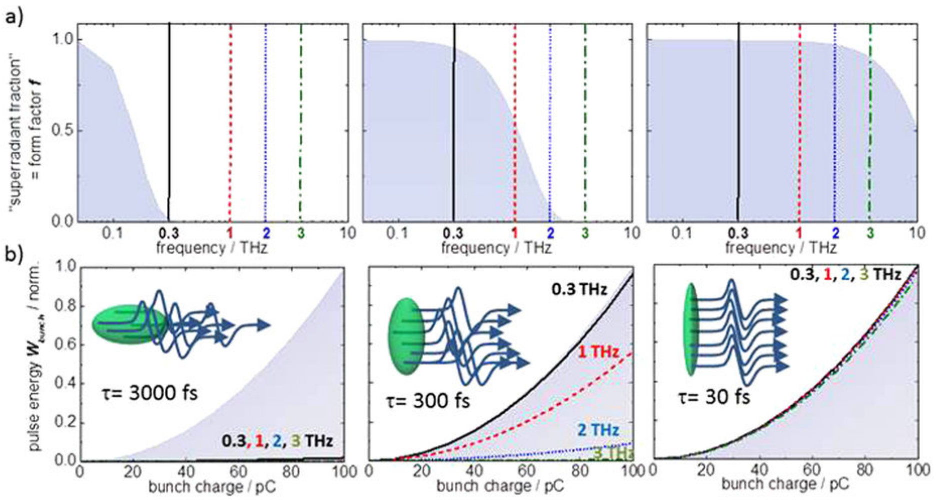

Figure 2.6: Superradiant emission from electron bunches becomes significant for frequencies sufficiently lower than the inverse of the bunch duration τ. Following equation 2.2 the emission scales quadratically with the charge at low enough frequencies but diminishes at higher frequencies when a smaller fraction of the charge fits within the wavelength. This behavior can be described by the dimensionless form factor f. (a) Form factors plotted for an assumed Gaussian bunch form with duration (FWHM) of 3000 fs (FWHM), 300 fs (FWHM) and 30 fs (FWHM) (grey-shaded). (b) Corresponding dependence of the pulse energies at THz frequencies of 0.3 THz (black solid), 1 THz (red-dashed), 2 THz (blue-dotted) and 3 THz (green-dash-dot) on the bunch charge. For simplicity a "white" radiator with a frequency independent emission characteristic is assumed. The upper edge of the blue-shaded area corresponds to the case of a form factor equal to 1. Taken from [6].

source to a point on the detector, Ω is the solid angle of the detector, ω is angular frequency, and U is pulse energy. Specifically, Equation 2.4 gives the intensity distribution of the radiation emitted by a single electron passing from vacuum into an infinite metal sheet that is perpendicular to the path of the electron, with an example of the result in Figure 2.7. The electric field of the particle changes when the dielectric constant changes, and the difference is "shaken off" as transition radiation. This equation includes only a first order approximation for the distance between the emitting screen and the detector, which means so-called "near-field" radiation is neglected, so this is only valid in the far field. The intensity of the radiation emitted is proportional to log(γ) of the particle, which sparked interest in transition radiation as a tool to measure relativistic particle energies [6]. Equation 2.4 makes several assumptions which should be addressed. It describes an infinite metal plane, it shows the intensity distribution from a single electron, and it is only valid for the far field. The far field condition is $D > \gamma^2\lambda$, where D is the distance, γ is the electron energy, and λ is the wavelength. The far-field distance

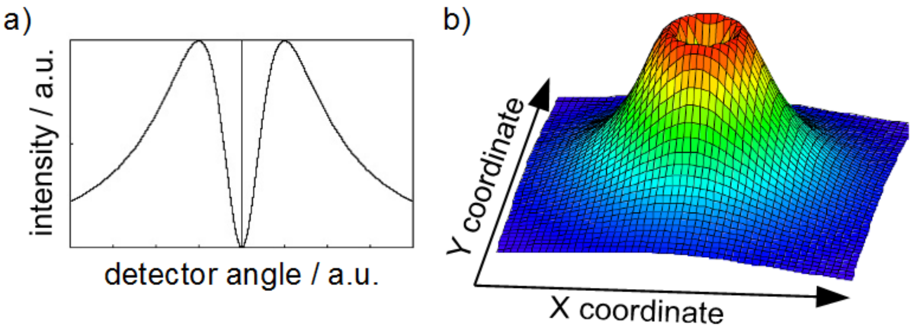

Figure 2.7: Illustration of calculated transition radiation distribution from an infinite screen on a far-field detector. a) A cross section of the intensity distribution across the detector, showing the result calculated by the Ginzburg-Frank equation. b) a 3D representation of the intensity distribution, showing the donut-shaped intensity distribution on the detector, which is given by taking the Gizburg-Frank result and applying it to the entire detector surface. Adapted from TESLA Report 2005 [27]

described is wavelength dependent. The limit comes from the Fresnel diffraction equations, and is essentially defining where only the first term is contributing. To account for electrons in bunches, instead of single electrons, one can introduce the formfactor term mentioned earlier. This still does not solve the problem of a single electron emitting up to infinitely high frequencies, as this is clearly not physical. The upper limit is generally defined by the plasma frequency of the metal the radiator is made from. One can ignore this in this work because the plasma frequencies are generally in the infrared, which is far higher than it is possible to radiate with the moderately short electron bunches at TELBE. One can account for a finite metal radiator by using a numerically solvable equation that can be derived with the virtual-photon method [31]. The parameterization used in the following equations is shown in Figure 2.8.

The first step gives up an equation which, when the radiator radius approaches infinity, returns the Ginzburg-Frank equation. This is known as the modified Ginzburg-Frank Equation [27]:

$$\frac{d^2U}{d\omega d\Omega} = \frac{e^2}{4\pi\epsilon_0 c} \cdot \frac{\beta^2 \sin^2\theta}{(1-\beta^2\cos^2\theta)^2}\left[1-T(\theta,\omega)\right]^2 \tag{2.5}$$

where $T(\theta,\omega)$ is the correction factor which addresses the finite radiator, written in terms of θ and ω:

$$T(\theta,\omega) = \frac{\omega a}{c\beta\gamma} J_0\left(\frac{\omega a \sin\theta}{c}\right) K_1\left(\frac{\omega a}{c\beta\gamma}\right) + \frac{\omega a}{c\beta^2\gamma^2 \sin\theta} J_1\left(\frac{\omega a \sin\theta}{c}\right) K_0\left(\frac{\omega a}{c\beta\gamma}\right) \tag{2.6}$$

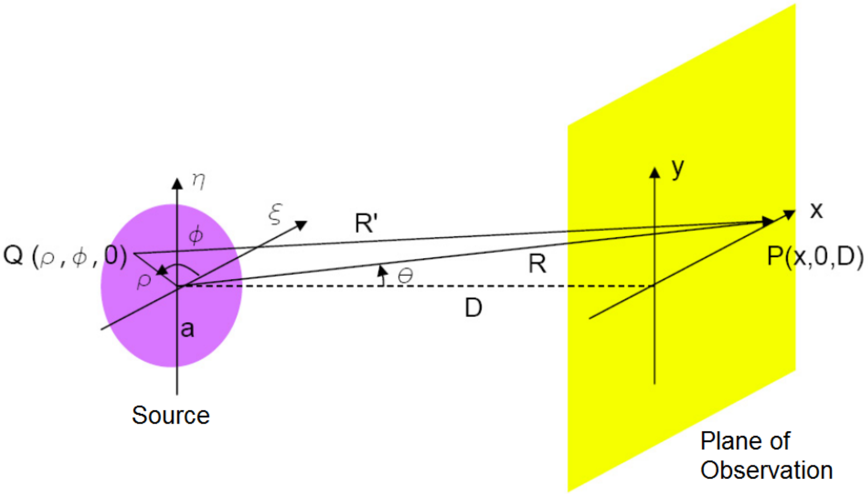

Figure 2.8: Schematic showing the parametrization used in the differential equations calculating diffraction radiation. This diagram illustrates the meaning of the various parameters used in the Ginzburg-Frank equation, with $Q(\rho, \phi, 0)$ representing the coordinate on the source screen in radial coordinates, and $P(x, 0, D)$ being the radial coordinate on the detector. In both cases the 0 is the height coordinate, making them two-dimensional. D is the distance between the centers of the source and the detector, R is the distance between the center of the source and an arbitrary point on the detector, and R' is the distance between an arbitrary point on the source and an arbitrary point on the detector. Taken from [27]

In these equations e is electron charge, ϵ_0 is the permittivity of vacuum, c is the speed of light, β is the ratio of electron speed to c, θ is the angle from the center of the radiator to the observation point on the detector, ω is the wavenumber, γ is the Lorentz factor of the electron, a is the radius of the metal radiator, J_0 and J_1 are Bessel functions of the first kind, and K_0 and K_1 are modified Bessel functions. To check the validity of this equation one can increase the radius a to the limit of infinity. For this case the terms in the correction factor are:

$$\lim_{a\to\infty} T(\theta,\omega) = 1 J_0\left(\frac{\omega a \sin\theta}{c}\right) K_1\left(\frac{\omega a}{c\beta\gamma}\right) = 0 \tag{2.7}$$

$$\lim_{a\to\infty} J_1\left(\frac{\omega a \sin\theta}{c}\right) K_0\left(\frac{\omega a}{c\beta\gamma}\right) = 0 \tag{2.8}$$

On the other end of the spectrum, an infinitely small radiator, one would expect to have no radiation. In this case:

$$\lim_{a\to 0} T(\theta,\omega) = 1 \tag{2.9}$$

which shows there is nothing radiated in this case.

At this point the equation describes the spectral density of DR radiation on a given point on a screen some distance away from the source, but is only valid where the far-field condition given earlier is still true. In order to get an equation that works in near-field as well one needs to revisit the derivation of this equation, which uses a first order approximation of the distance between the radiator and the detector. If a second order approximation is used, the far-field condition is no longer required to get a good solution, but it becomes unsolvable by analytic means, so a numerical calculation must be utilized. The distance R' from an arbitrary spot on the radiator to an arbitrary spot on the detector is:

$$R' = \sqrt{D^2 + (x - \rho\cos\phi)^2 + (\rho\sin\phi)^2} \approx R - \frac{x\rho\cos\phi}{R} + \frac{\rho^2}{2R} \tag{2.10}$$

R is the distance from the center to the diffraction source to the center of the detector, ρ is the radius of an arbitrary point on the diffraction radiator, ϕ is the azimuthal angle to the point on the diffraction radiator, and x is the point on the detector. Taking the three terms shown, one can derive the following equation for the spectral density. This equation leaves off the scaling factor, but is otherwise a more accurate version of Eq. 2.5 above.

$$\frac{d^2U}{d\omega d\Omega} \propto \left| \int_0^a J_1(k\rho\sin\theta) K_1\left(\frac{k\rho}{\beta\gamma}\right) exp\left(ik\frac{\rho^2}{2R}\right)\rho d\rho \right| \tag{2.11}$$

Taking the first order approximation of Eq. 2.11 and performing the integration on it yields the original Ginzburg-Frank.

Diffraction Radiation

Diffraction radiation is generated when an electron bunch passes near, but not through, a conducting material. This is usually accomplished by taking a transition radiation source and inserting a small aperture which the charged particles can pass through, making a so-called diffraction radiator. This is illustrated in Figure 2.9. The electric field still experiences a change in dielectric constant even if the particle itself does not pass directly through the material. It is very similar to transition radiation in both the procedure to generate it and the pulse characteristics. The main difference is a loss of some of the higher frequency components which is dependent on the aperture size, with larger apertures losing more higher frequency components than screens with smaller apertures.

From a calculation standpoint it is possible to get the intensity distribution by starting with the diffraction radiation equation, and subtracting out the contribution of a small disc of metal in the center, in what will become the aperture. This

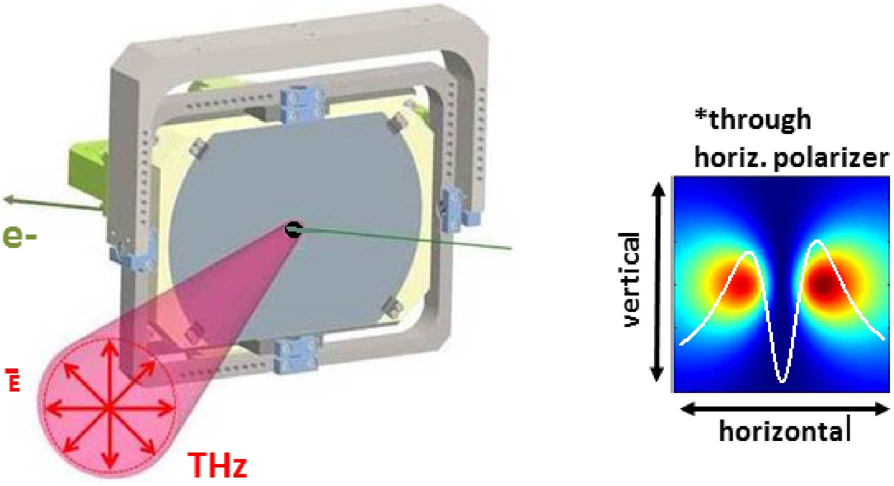

Figure 2.9: Working principle of a diffraction radiator (DR) and a simulated beam profile for the horizontal polarization component. Left: This image is a diagram of the diffraction radiator installed at ELBE, with the grey truncated circle in the center being the screen itself. The lighter grey support structure surrounding it is used to adjust the position and angle of the screen in relation to the incoming electron beam, which is shown as a green line passing through the aperture in the middle of the screen. The resulting radially polarized THz pulse is shown in red. Right: A simulated diffraction radiation pulse profile, shown after polarization. The two lobes are the horizontally polarized portion of the radially polarized original pulse. Taken from [6]

gives an equation which looks like this:

$$\frac{d^2U}{d\omega d\Omega} = \frac{e^2}{4\pi\epsilon_0 c} \cdot \frac{\beta^2 \sin^2\theta}{(1-\beta^2\cos^2\theta)^2} \left[T_b(\theta,\omega) - T_a(\theta,\omega)\right]^2 \tag{2.12}$$

$$T_a(\theta,\omega) = \frac{\omega a}{c\beta\gamma} J_0\left(\frac{\omega a \sin\theta}{c}\right) K_1\left(\frac{\omega a}{c\beta\gamma}\right) + \frac{\omega a}{c\beta^2\gamma^2\sin\theta} J_1\left(\frac{\omega a \sin\theta}{c}\right) K_0\left(\frac{\omega a}{c\beta\gamma}\right) \tag{2.13}$$

$$T_b(\theta,\omega) = \frac{\omega b}{c\beta\gamma} J_0\left(\frac{\omega b \sin\theta}{c}\right) K_1\left(\frac{\omega b}{c\beta\gamma}\right) + \frac{\omega b}{c\beta^2\gamma^2\sin\theta} J_1\left(\frac{\omega b \sin\theta}{c}\right) K_0\left(\frac{\omega b}{c\beta\gamma}\right) \tag{2.14}$$

The variables are the same as in equation 2.5, with the addition that a is the radius of the screen, and b is the radius of the aperture in the screen. The modified Ginzburg-Frank can be recovered if one takes the limit as $a \to \infty$ and the limit as $b \to 0$.

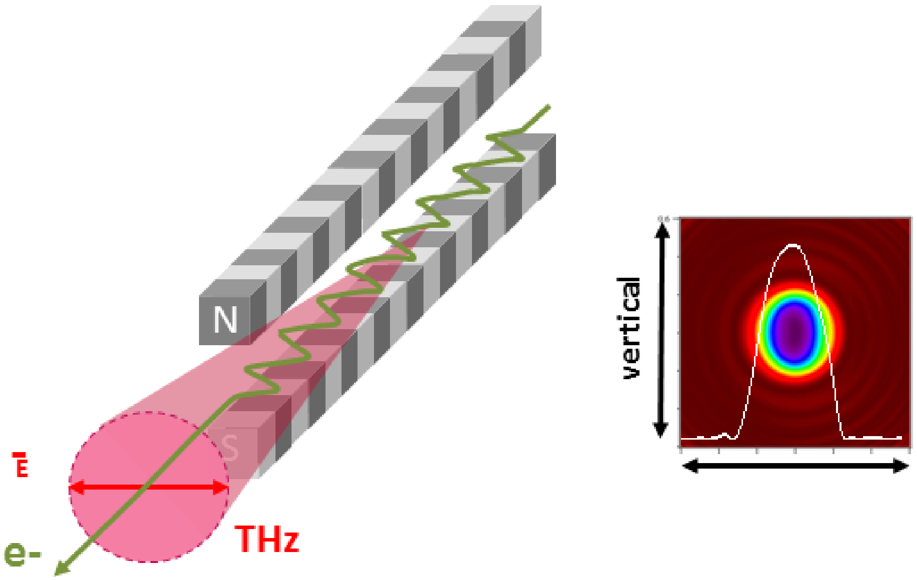

Figure 2.10: Illustration of the concept behind undulator radiation, showing the radiation as coming from a point source in the center of the undulator (left) and a calculation of the intensity distribution of a 1 THz tuned undulator in the fundamental frequency, which shares a characteristic bell shape with higher odd numbered harmonics (right) Taken from [6].

Undulators

The principles of the undulator were described by V. L. Ginzburg in 1947 [32]. It is a device based on synchrotron radiation, which was observed for the first time that same year, at the General Electron Synchrotron accelerator [33]. The first undulator was constructed by H. Motz in 1952 [34] at Stanford University. By placing multiple bending magnets in a row in order to create a sinusoidal beam path for a charged particle (shown in Figure 2.10) it is possible to create a narrow bandwidth, high intensity light source that can be tuned to range of frequencies which are set by the physical characteristics of the undulator and the electron bunch properties of the accelerator that powers it. The wavelength of undulator radiation can be controlled by varying the strength of the magnetic field and the intensity by the energy and charge of the electron bunches passing through it. The output wavelength is

$$\lambda = \frac{\lambda_u}{2\gamma^2}\left(1 + \frac{K^2}{2} + \gamma^2\theta^2\right) \tag{2.15}$$

where λ_u is the undulator period length, γ is the electron energy, θ is the output angle, K is the K-parameter (see 2.17). The bandwidth is given by $\Delta\nu = 1/N$ where N is the number of periods [35].

Undulators emit radiation in a cone whose size depends on the wavelength of a given harmonic. The following equation describes this relationship:

$$\sigma_{r'} = \sqrt{\frac{\lambda_n}{2N\lambda_u}} \tag{2.16}$$

where $\sigma_{r'}$ is the solid angle of the radiation cone, λ_n is the wavelength of the nth harmonic, N is the number of undulator periods, and λ_u is the length of one undulator period [36]. Beam intensity is concentrated in a theoretically circular beam profile, with the center of the beam containing the fundamental and higher harmonics appearing towards the edges of the beam profile. The circular beam profile depends on an electron bunch with no angular distribution. In practice, however, the bunches will not be perfect, leading to small changes in the beam profile resulting in a shape that is more oblong [36]. Figure 2.10 shows a calculated beam profile (right) which illustrates this, showing a typical distribution of intensity for a 1 THz undulator beam.

The number of harmonics generated is dependent on the so-called K parameter:

$$K = \frac{ecB_0}{m_e c^2}\frac{\lambda_p}{2\pi} \tag{2.17}$$

where e is the fundamental electron charge, c is the speed of light, B_0 is the undulator magnetic field strength in Tesla (T), m_e is electron mass, and λ_p is the undulator period length in cm. The higher this number is, the more fundamentals appear in the spectrum. As this number becomes much greater than one ($K \gg 1$) the source is typically referred to as a wiggler instead of an undulator. As with DR sources, undulators can be used in the superradiant regime, and the emitted intensity will increase as bunch charge squared as the bunch length approaches the fundamental wavelength. In contrast to DR sources, undulators are dispersive beam elements and the duration of chirped electron bunches may change as they pass through them.

2.3 THz radiation detection

Detecting THz radiation can sometimes be problematic because it occupies a position in the electromagnetic spectrum between optical and microwave wavelengths. There are many different approaches to detecting THz, utilizing a variety of physical phenomena. The ability to detect THz is critical to this work, as this is a necessary prerequisite to using it in meaningful experiments and diagnostic setups. As is shown in this work, it is important to be able to see the intensity of single pulses, to get a reliable measurement of the average power, and to analyze the beam profile. Some experiments require information on the longitudinal (in the time domain) shape of individual pulses, or even their actual waveform. The following sections deal with the different THz detection schemes and detectors utilized at TELBE to characterize the TELBE THz radiation.

2.3.1 Pyroelectric detectors

The pyroelectric effect is a phenomenon that occurs when so called pyroelectric materials change temperature. The earliest mention of this effect comes from the 3rd century BC by a Greek named Theophrasutus [37]. He noted that tourmaline would attract ash or small bits of metal when heated. The effect was later rediscovered in the 18th century, and finally named in 1824 by David Brewster [38]. Changes in temperature cause a change of the electrical polarization which induces a voltage across the material [39]. This voltage then gradually decreases due to leakage current, either through the material itself or through an outside path. Pyroelectric materials can therefore be used to detect radiation from the THz to x-ray range by measuring voltage across them. Any change in voltage is caused by heat being deposited in the material by a light pulse. Thus, the appearance of a detected light pulse is two spikes in voltage, of opposite polarity. The first spike appears when the material is warmed by the light pulse, the second spike is caused when the material cools back to its original temperature after the pulse has passed, while a continuous radiation beam would not lead to a detectable signal. Front end electronics have been developed at DESY that take these two pulses and output them as a single pulse to make analyzing the detected pulses easier [40]. A diagram of a basic pyroelectric detector is given in Figure 2.11.

Pyrodetectors work at room temperature and can be operated at repetition rates in the 100 kHz regime. This type of detector has been most frequently used at TELBE to date because it allows pulse to pulse intensity detection at the typical operating repetition rate of 100 kHz. It is also easy to convert the signal to a quantitative measure of the pulse energy because the intensity response is linear. There are a few major problems, though, with this type of detector. The frequencies of interest in THz are generally difficult to absorb with the standard materials used in pyroelectric detectors. These materials can be transparent to some frequencies in the THz range which of course make it difficult to detect them. Any frequencies that pass through the absorber material are not measured in the detector, leading to possibly lower readings than the actual beam power. There is also a problem with linearity at high intensities. The special fast detectors that were developed at DESY have a linear response up to a signal value of 1 V, so it is important to limit incoming intensity so that the signal is less than 1 V in order to stay in the linear regime. In addition the base noise level is high (±50 mV). This leads to a large error bar in the few 10% range in single pulse intensity measurements. Finally, pyroelectric detectors are too slow to resolve the actual pulse duration, which is

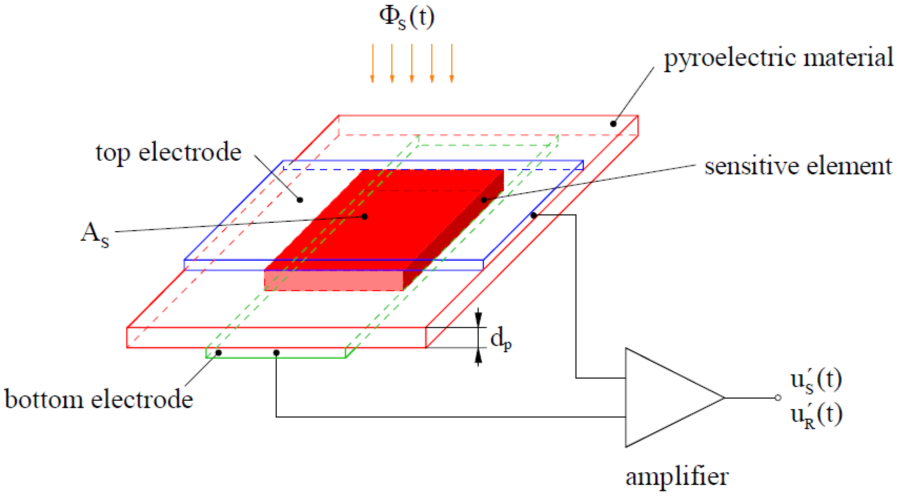

Figure 2.11: Diagram of a pyroelectric detector. $\Phi(s)_t$ is the incoming light pulse, d_p is the thickness of the pyroelectric material, A_s is the surface area of the radiation sensitive element (where the pyroelectric material is between the two electrodes) which has some absorption factor dependent on the incoming wavelength. The output signal voltage is μ'_s and the noise voltage is μ'_r. Taken from [41].

in the few ps (FWHM) regime.

2.3.2 Schottky Diode

Schottky diodes are diodes formed with a metal-semiconductor junction, as opposed to the semiconductor-semiconductor junction that regular diodes use. Schottky diodes have a lower turn-on voltage, which is the voltage needed to allow current to flow through, and a faster response time than either regular diodes or pyroelectric detectors, with a bandwidth in the GHz range [42]. These detectors work by rectifying and demodulating signals, converting them into a DC voltage. Like pyroelectric detectors, they can be used as broadband detectors, or tuned to specific wavelengths with varying bandwidths by coupling them with different, carefully designed antennas [43]. Because of the small size and simplicity of construction, it is possible to mount several detectors with different antennas on a single chip, creating a single-chip spectrometer. Because of the speed of the detectors, higher repetition rates into the tens of MHz range can be utilized while maintaining single-pulse measurement capability [44]. One such spectrometer is being developed under the BMBF project InSEL and an early version is shown in Figure 2.12 [45]. However, Schottky diode detectors remain too slow to measure the actual pulse form of a ps-range THz pulse.

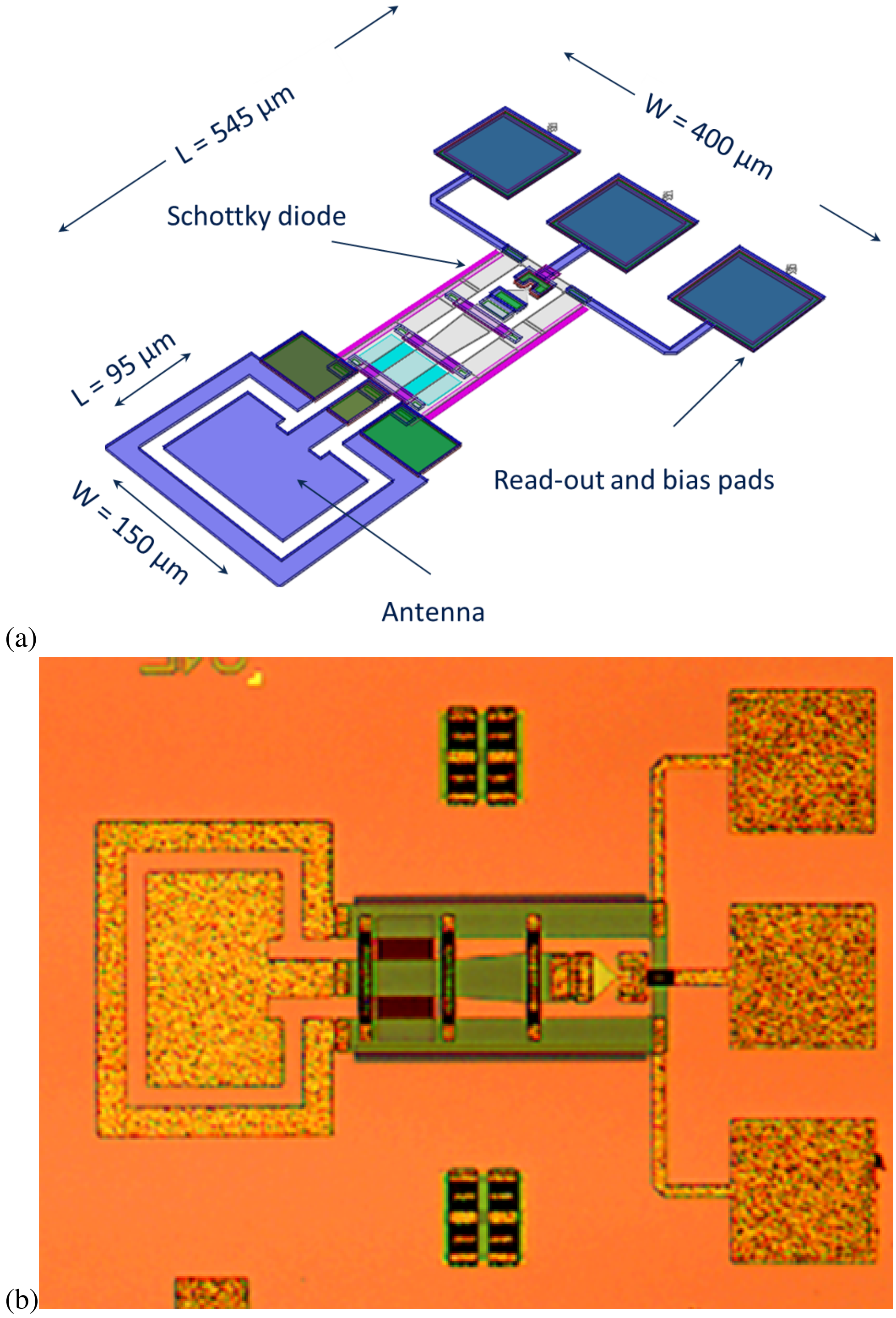

Figure 2.12: (a) Integrated on-chip THz detector with patch antenna, Schottky diode, matching, biasing and read-out circuitry in a coplanar waveguide layout. (b) Chip photograph of THz detector manufactured in UMS BES GaAs process. [44]

Material	EO coefficient (pm/V) at (μm)	Index of refraction at (μm)	Dielectric constant	GVM (ps/mm)
ZnTe	$r_{41} = 4.04$ at 0.633	$n = 2.853$ at 0.800	$\epsilon = 10.1$	1.1
CdTe	$r_{41} = 4.5$ at 1.000	$n = 2.84$ at 0.800	$\epsilon = 9.4$	0.75
GaAs	$r_{41} = 1.43$ at 1.150	$n = 3.61$ at 0.886	$\epsilon = 13$	0.015
$LiTaO_3$	$r_{33} = 30.5$ at 0.633	$n_0 = 2.176$ at 0.633	$\epsilon_{1,2} = 41$	14.1
	$r_{13} = 8.4$ at 0.644	$n_e = 2.180$ at 0.633	$\epsilon_3 = 43$	
$LiNbO_3$	$r_{33} = 30.9$ at 0.633	$n_0 = 2.286$ at 0.633	$\epsilon_{1,2} = 43$	14.2
	$r_{13} = 32.6$ at 0.644	$n_e = 2.200$ at 0.633	$\epsilon_3 = 28$	

Figure 2.13: Table of common electro-optic materials and their properties. An ideal material has a high EO coefficient for the probing wavelength (800 nm for TELBE) and a low group velocity mismatch (GVM). Taken from [47].

2.3.3 Electro-optic detection

Electro-optic effect

The electro-optic effect is an interaction between certain materials and applied electric fields which results in the an induced birefringence. Only materials that lack inversion symmetry can exhibit this effect, which limits it to certain types of crystals, such as ZnTe, GaP, and $LiNbO_3$. It is a second order nonlinear optical effect, and its nonlinear polarization $P_i^{(2)}$ can be described by the equation:

$$P_i^{(2)} = \epsilon_0 \sum_{j,k=x,y,z} \chi_{ijk}^{(2)} \varepsilon_j \varepsilon_k \tag{2.18}$$

where ϵ_0 is the permittivity of free space, $\chi_{ijk}^{(2)}$ is the second order nonlinear susceptibility tensor, and ε_j and ε_k are the electric field components [46, Chapter W]. However, a more common formulation is:

$$\Delta \left(\frac{1}{n^2} \right)_i = \sum_{j=1}^{3} r_{ij} \varepsilon_j \tag{2.19}$$

where ε_j is the electric field component. The tensor r_{ij} is known as the electro-optic tensor (where the coefficients of Eq. 2.18 are called the piezoelectric coefficients). These tensor elements depend on the crystal symmetry group of the EO crystal. For example, ZnTe and GaP have a zincblende structure. This symmetry means that most of the coefficients are zero, so in zincblende only $r_{14} = r_{25} = r_{36}$ are non-zero. Values of these non-zero coefficients for common EO materials range from a few 10 pm/V to a few 10 pm/V (see Figure 2.13).

Electro-optic sampling

Electro-optic sampling system is most commonly used to measure the time domain form of THz pulses. They work by altering the polarization of a probe beam that propagates through the electro-optic crystal co-linear with a THz pulse. This effect is quasi-simultaneous and can be used to detect signals on femtosecond timescales. This makes it possible, therefore, to detect and analyze the actual THz waveform. The slowly (relative to the probe pulse) oscillating THz electric field induces a birefringence in the crystal, which is subsequently probed by measuring the polarization state of a fs-laser pulse that is passed through it. This altered polarization can be detected by putting the probe beam through a Wollaston prism and comparing the intensity of the resulting two beams of orthogonal polarization. An illustration of a typical electro-optic sampling setup can be seen in Figure 2.14. By delaying the probe pulse with respect to the THz pulse, one can take multiple readings and reconstruct the electric field of the THz pulse. It is also important to make sure the phase matching condition is fulfilled in order to get efficient interaction between the THz pulses and the fs-lase probe pulses. Meeting this condition means that the group velocity of the optical pulse is the same as the phase velocity of the THz pulse. For ZnTe the condition is met for THz pulses by using an 800 nm probe pulse. Another parameter of importance is the group velocity mismatch (GVM). This is the difference in group velocity between the THz pulse and the probe pulse. For instance, in ZnTe using an 800 nm probe there is a GVM of about 1 ps/mm. That means that while using an 800 nm laser and ZnTe it is important to have crystals that are sufficiently thinner than 1 mm or the GVM will cause the setup to be insensitive to higher THz frequencies.

Of less importance, but still a useful optimization, is the orientation between the azimuthal angle of the crystal and the polarization of the THz and probe beam [48]. This refers to the relative angles of the polarization of the (linearly polarized) probe and THz beam, and the lattice orientation of the EO crystal. Various combinations of orientation can yield either a strong signal or no signal at all, given all other factors are the same. Finally, there are two readout configurations that are possible. First, there is “cross-polarized”. This is when the THz-induced changes to polarization are measured as transmission through a cross-polarized prism, and residual birefringence of the EOS crystal is compensated with a quarter-wave plate (QWP) or Babinet compensator.

When THz is present it rotates the polarization so that some of the beam is able to pass through the polarizer, showing up as a signal on the detector. The other possibility is known as a standard ellipsometry configuration. This involves making the beam elliptical after the EO crystal, and measuring the induced ellipticity. This allows a negative electric field to be detected when the probe beam split in a polarizing beam splitter, with the two subsequent beams subtracted from each other. The response here is linear with electric field, showing all positive and negative components at the final readout. While electro-optic sampling in this configuration is fast enough to detect the longitudinal pulse profile, and even the waveform, it is still necessary to integrate over many pulses.

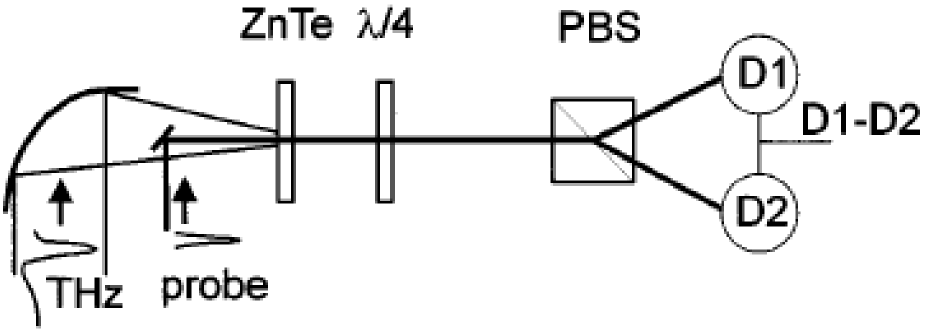

Figure 2.14: Electro-optic sampling setup. The THz pulse is focused onto an electro-optic crystal, ZnTe in this example, with an off-axis parabola. The probe laser is passed collinearly through the same spot on the crystal. A quarter waveplate ($\lambda/4$) is then used to adjust for any changes to the probe beam caused by the dispersion of the electro-optic crystal. The probe beam is then analyzed by passing it through a polarizing beam splitter (PBS), and the two resulting beams are sent into two detectors (D1 and D2) where the signals are subtracted (D1-D2) to get the final measurement of the THz pulse. Not shown is a mechanical delay stage to move the relative arrivaltime of the probe pulse to different parts of the THz pulse in order to sample the whole pulse. Taken from [48].

Single shot THz detection

In addition to the basic EOS setup, which uses multiple THz pulses to create an image of the average pulse form, there are single shot methods which allow the imaging of a single THz pulse all at once. One such method, which is in use at TELBE, is called spectral decoding (or alternately spectral encoding) [49]. This is a method where a pulse from a fs-laser is taken and stretched, making the resulting pulse much longer temporally and with a linear spread of spectral components in time (which is referred to as a chirped pulse). Then this pulse is passed collinearly through an EO crystal with the THz. This results in the temporal profile of the THz pulse being transferred to the spectrum of the probe pulse. The resulting image of the THz pulse can then be read out by a line-array CCD coupled to a spectrometer, as illustrated in Figure 2.15. The temporal resolution of this setup depends on the how far the pulse is stretched and the characteristics of the spectrometer and readout camera.

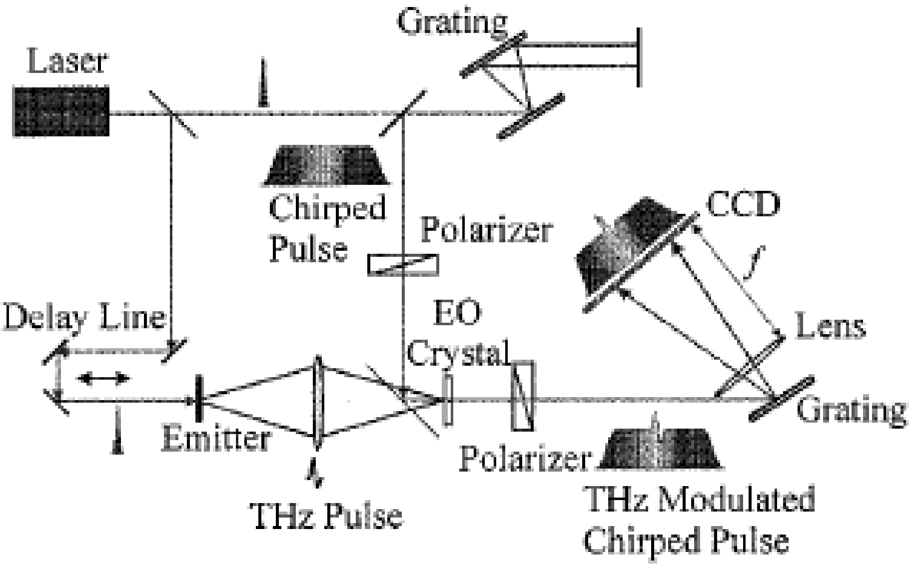

Figure 2.15: Spectral decoding setup. A fs-laser pulse is passed through a stretcher, lengthening it to a multi-ps long pulse. It is then passed through a polarizer to eliminate any unwanted polarizations. Next it is sent through an electro-optic crystal collinear with the THz pulse being measured. In this case, the THz pulse is generated by the same laser, but in TELBE the THz would originate in the CDR or undulator. The laser pulse is once again passed through a polarizer, this time to remove the original polarization, leaving only the light that was rotated by the THz pulse. Finally, it is passed through a spectrometer and read by a CCD. This scheme was adapted to the requirements of the TELBE facility as part of this work. The setup is able to achieve a time resolution of 30 fs (FWHM). It also allows the imaging of the waveform of individual THz pulses. Taken from [49].

2.3.4 PyroCam

Using the same physical process as the previously described pyroelectric detectors, a company called OPHIR produces a THz beam profiler named the PyroCam [50] that uses a 2D array of 80 μm sized pyroelectric detectors arranged as pixels. This camera can display beam profiles from the visible to the THz range for use in focusing and beam profiling. One drawback is the varying frequency response, as described earlier in the pyroelectric detector section. For longer wavelengths in particular it is possible the PyroCam is insensitive, and the beam profile image that appears might only contain a subset of the frequencies, in this case higher THz, that make up the beam. It is then possible that the spatial profile of the various frequency components of a THz beam can differ, leading to beam profiles that might not be accurate for the entire beam, or might show changes in profile or intensity for beams with different narrowband frequencies even when the beam shape itself has not changed.

2.3.5 Terahertz Powermeter

Accurate measurements of beam power are problematic in the THz range [51]. Ophir Optics manufactures a power sensor that is claimed to be calibrated for 0.3 THz to 10 THz, making it a useful tool for the characterization of the TELBE THz beams [52]. It consists of a thermopile detector utilizing a volume absorber made of neutral density (ND) glass, which has a diameter of 12 mm. A thermopile is a collection of thermocouples (a metal-metal junction) connected in series, and each thermocouple generates a current based on the thermoelectric effect, which itself is caused by the electron energy levels in the two metals being shifted by different amounts as the temperature changes [39]. The use of a volume absorber helps to prevent too much power from depositing in a small volume (as in a surface absorber) and damaging the sensor. Because the power measurement depends on deposited heat, and that heat can take several seconds to dissipate, these power meters are most useful for measuring average power, not single pulse power. TELBE uses an Ophir Optics 3A-P-THz sensor, which has a range of 15 μW to 3 W, with a 4 μW noise level. The sensor is read out by an Ophir Optics Vega powermeter. The calibration has been verified by the Phyikalisch-Technische Bundesanstalt (PTB) for THz frequencies between 1 and 5 THz [51] as well as for 0.7 THz.

Chapter 3

Results

3.1 Diagnostic developments

TELBE is the first working superradiant THz user facility driven by a quasi-cw SRF accelerator [6]. The primary application of TELBE in the materials and life sciences is to utilize the transient THz fields as a novel highly selective excitation for non-linear dynamics [3]. These dynamic processes are typically studied by means of pump-probe experiments on few 10 fs (FWHM) timescales involving synchronized external laser systems. The main motivation for the developments presented here is that ultrafast experiments at TELBE require a novel pulse resolved diagnostic and data acquisition system in order to achieve the excellent dynamic range and time resolution required to probe the often subtle fingerprints of the induced transient states of matter. This has to be done by correcting for fluctuations in the THz pulse parameters post-mortem, specifically arrivaltime and intensity, since the ELBE accelerator lacks suitable beam-based feedbacks.

This work yielded the development of two main diagnostic systems at TELBE, one prototype THz arrivaltime monitor capable of few 10 fs (FWHM) resolution and one pulse-resolved intensity monitor. As shown later, the former has been used in several successful time-resolved experiments performed at TELBE. The latter is still in the testing phase and has only been used in one example experiment, shown in section 3.3. Figure 3.1 shows the layout of the pulse-resolved arrivaltime system and intensity monitor as well as two measurements taken of the arrivaltime and intensity fluctuations.

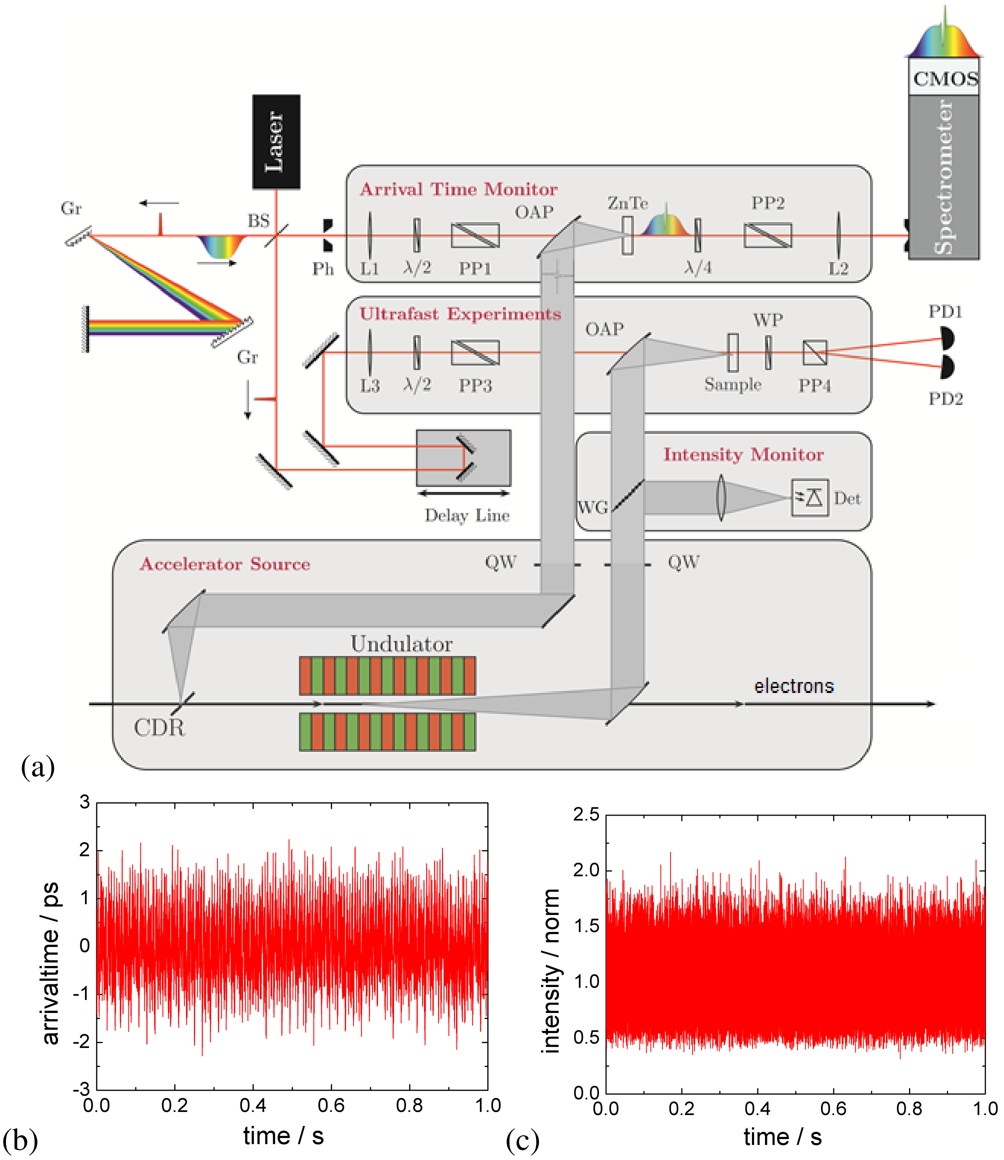

Figure 3.1: (a) Schematic diagram of the developed pulse-resolved diagnostic at the TELBE facility, combining a 30 fs (FWHM) resolution arrivaltime monitor with a pulse intensity monitor. (b) Arrival time of THz pulses over 1 second showing an arrivaltime jitter of around ±2 ps (FWHM). (c) Intensity of the THz pulses from the undulator tuned to 300 GHz taken over 1 second. Data taken using the thermionic injector, with a beam energy of 24 MeV and a bunch charge of 70 pC. Adapted from [7].

3.1.1 THz intensity instabilities and correction

One of the challenges at TELBE is to account for changes in intensity of the THz pulses. Intensity measurements can be performed alongside the experiment, as shown in Figure 3.1 a. A wire grid polarizer is used as a beam splitter, and a small portion of the THz beam acting as a pump excitation is diverted into a purpose-built pyroelectric detector. The most important factors for choosing the specific pyroelectric detector, developed at DESY for the TELBE intensity monitor, are its sufficiently high speed and robustness in handling (see Section 2.3.1 for more information). These pyroelectric detectors have a relatively high noise floor of ±50 mV [53]. One must also be careful not to put too much intensity onto the detector. If the intensity is too high, the detector no longer has a linear response. In this specific case, the linear regime is when the output signal remains below 1 V. Combined with the noise floor of ±50 mV this results in a relatively poor S/N ratio. Nevertheless, many revealing observations can be made. Figure 3.2 shows that intensity fluctuations can be considerable and in the range of 50% or more. Figure 3.3 shows the spectral content of a typical pulse intensity measurement, taken over 1 second. Major frequencies are marked. A zoom in on the lower frequencies clearly shows 50 Hz (labeled in red), representing line noise, and many higher harmonics. A detailed discussion of the observed intensity instabilities follows in section 3.1.2. Such an analysis can help in identifying the origin of different instabilities.

These instabilities can come from any number of sources, from fluctuations in the bunch charge to beam position instabilities to electronic noise in the detection setup. Note that more than half of the intensity instabilities occur with frequencies below 10 kHz (see Figure 3.3 a). This would allow for the employment of moderately fast beam-based feedbacks to stabilize the intensity, given that the exact origins of the instabilities are known. In this work the determination of the pulse-resolved intensity fluctuations serves to correct for them in experimental data. Moreover, these instabilities in pulse energy can be harnessed to provide a pulse-energy-resolved measurement utilizing the intensity fluctuations as fast modulation of the pulse intensity. One example of such a measurement is shown in section 3.3 where the fluence dependence of the THz-driven spinwave is determined by including the pulse-resolved intensity measurement into the data analysis.

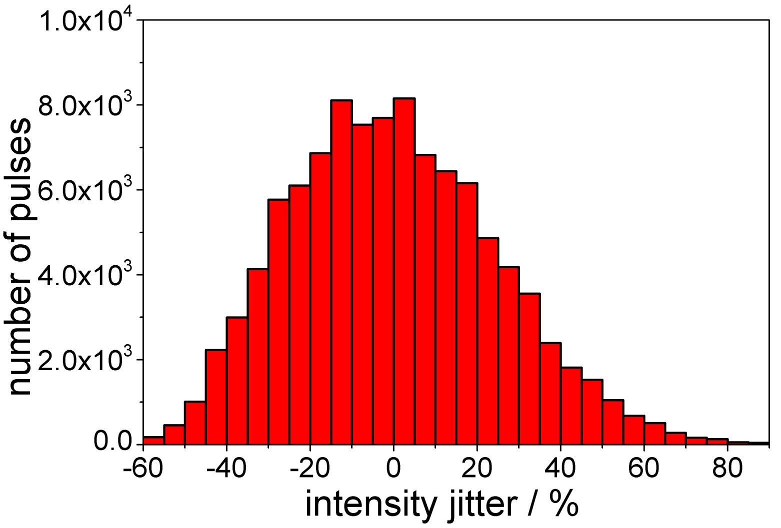

a)

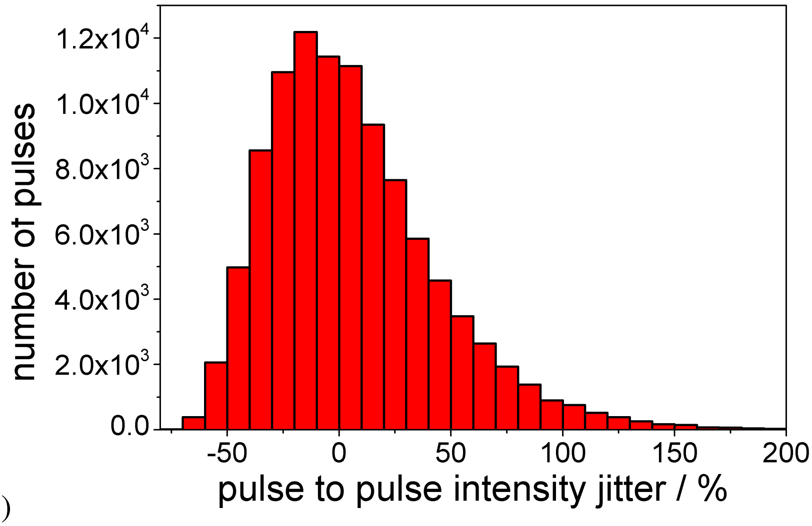

b)

Figure 3.2: (a) Histogram of the change in intensity of pulses from the TELBE undulator source relative to the average intensity. (b) Histogram of the pulse-to-pulse (the change in arrivaltime compared to the previous pulse, rather than to an expectation value) intensity fluctuations taken over 1 second. Note that the uneven distribution here is likely caused by some of the THz pulses being intense enough to enter the non-linear regime of the detector. Data was taken for an undulator tune of 300 GHz at a repetition rate of 101 kHz, with a beam energy of 24 MeV and a bunch charge of 70 pC.

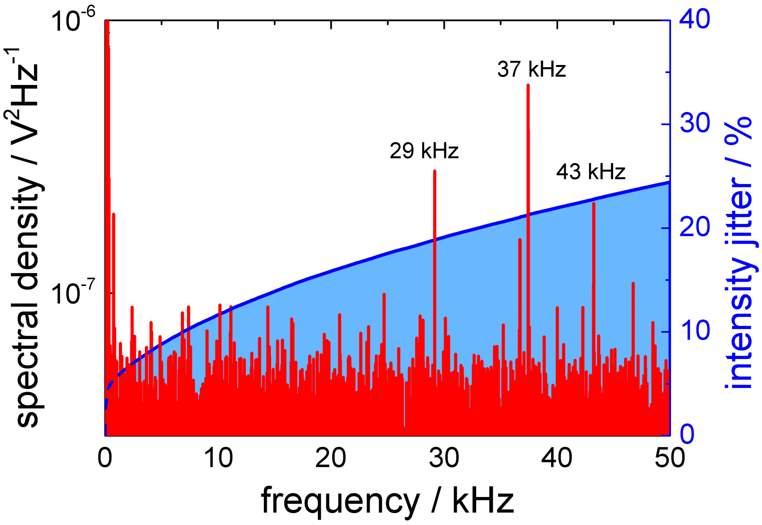

a)

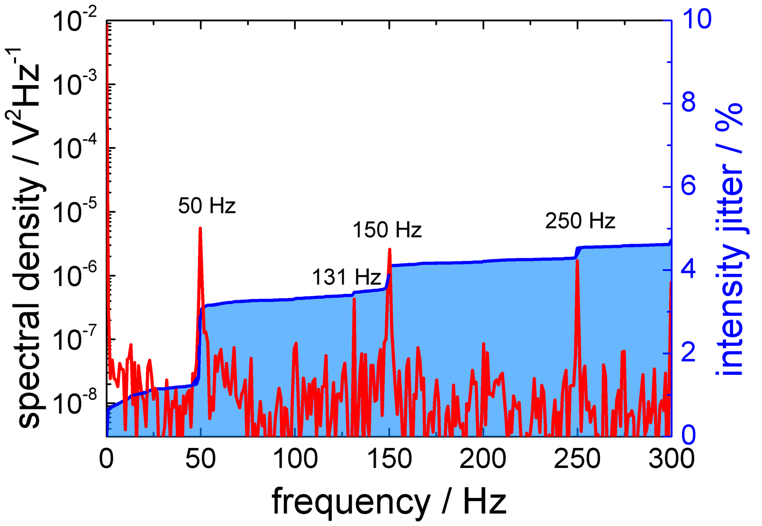

b)

Figure 3.3: (a) Spectrum of the fluctuations in the beam intensity of the undulator pulses at a 300 GHz tune, taken over 1 second. Shaded blue area represents the sum of the intensity fluctuations contributions from each frequency component, which shows fluctuations of up to 25% from the mean. (b) A zoomed in view of the low frequency area of the plot, showing the expected line noise frequency (50 Hz) and higher harmonics. Here one can see that the components below 300 Hz cause intensity fluctuations of almost 5% from the mean, which accounts for almost 20% of the total intensity fluctuations over the course of 1 second. Data was taken at a repetition rate of 101 kHz, with a beam energy of 24 MeV and a bunch charge of 70 pC.

3.1.2 THz arrivaltime instabilities and correction

Accurate timing of an accelerator to an external laser system can be accomplished several ways. One method is based on RF pickups installed in the electron beam pipe, and the signal caused by the Coulomb field of the passing bunch can be used to derive an arrival time with respect to an external laser [54]. One such system, called the beam arrivaltime monitor (BAM) has been installed between the diffraction radiator and the undulator sources of the TELBE facility. As shown later in this work, the arrivaltime jitter determined here unfortunately does not correspond well to the arrivaltime jitter of the actual THz pulses in the TELBE laboratory. This rather surprising find made the development of an experiment-near arrivaltime monitor crucial. The monitor developed for TELBE is based on so-called spectral decoding, which is a single-shot electro-optic technique described in detail in Section 2.3.3. Other techniques were considered, such as temporal decoding [55] and spatial decoding [56]. These were ultimately found to be insufficient for TELBE. Temporal decoding maps time into spatial coordinates via a non-linear process [55]. This process demands a high pulse energy probe laser be used, which are only commercially available with low repetition rates. Spatial decoding [56] maps time into spatial coordinates via a projection of the THz field onto the probe laser profile. The achievable time window for this process at TELBE is 1-2 ps (FWHM). This window is too small for the typical temporal drifts in the ELBE accelerator, which are in the few ps (FWHM) regime.

In contrast, spectral decoding can be performed with nJ probe laser pulses with a sufficiently wide time window. The probe beam for the monitor is currently provided by a commercial amplified laser system [57]. Operating at 202 kHz it provides μJ pulse energies, which is orders of magnitude more than required for spectral decoding. In the work performed here, most of the intensity of the probe laser can hence be used for probing the THz-driven dynamics, as shown in Figure 3.1.

The magnitude of the overall jitter on a 1 second timescale is on the order of 1-2 ps (FWHM) (see Figure 3.4). The jitter from pulse to pulse is on the order of 200 fs (FWHM). Figure 3.5 gives an example phase noise spectrum of the arrivaltime instabilities taken with the experiment-near THz arrivaltime monitor at TELBE. The data was taken at the same rate as the accelerator was operating, 101 kHz, and therefore includes the arrivaltime information of every THz pulse during this time period. Strong spectral components are marked with their frequencies, including the line frequency of 50 Hz and its higher harmonics. As in the case of the intensity instabilities, the dominant jitter components stem from lower frequencies below 10 kHz (see Figure 3.5).

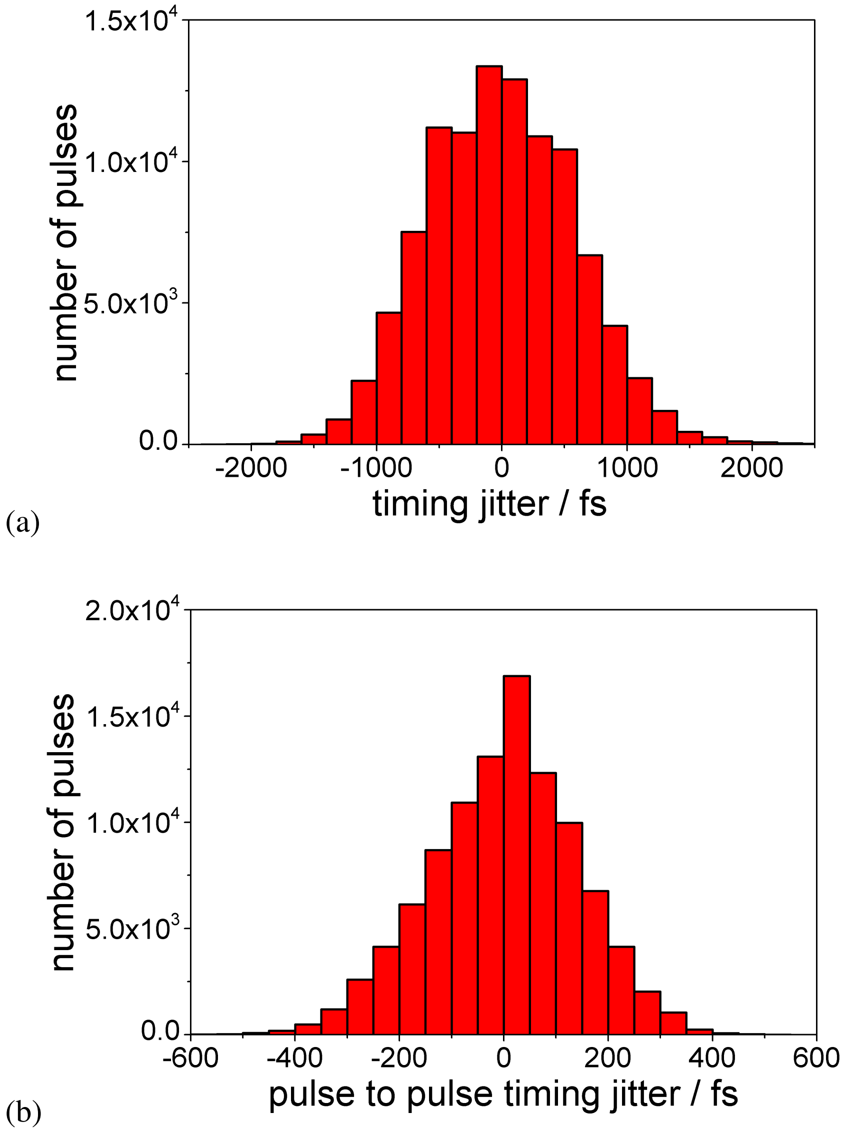

Figure 3.4: (a) Histogram of the arrivaltime relative to the average value. (b) Histogram of the pulse-to-pulse arrivaltime jitter. Data taken at the full 101 kHz repetition rate of the accelerator over 1 second, with a beam energy of 24 MeV and a bunch charge of 70 pC.

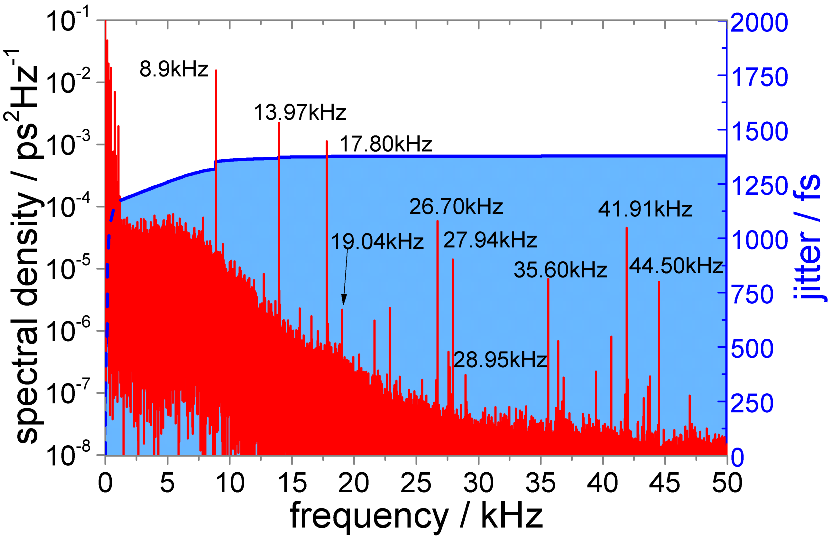

(a)

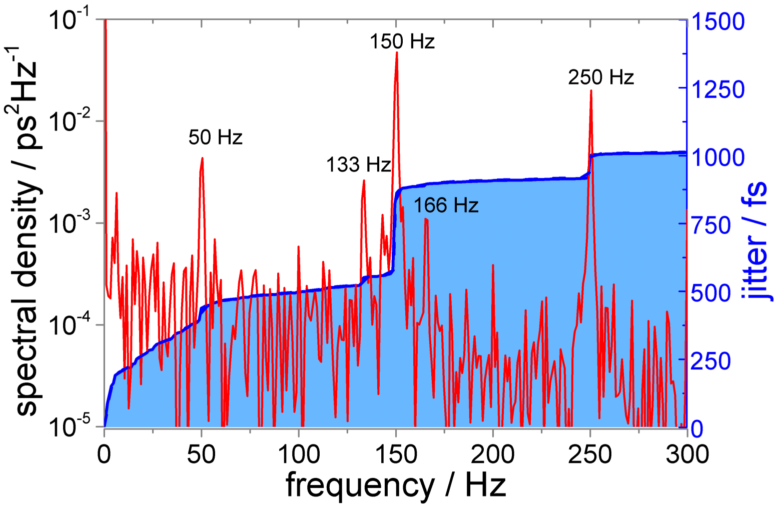

(b)

Figure 3.5: (a) Example of a typical phase noise spectrum of the arrivaltime jitter in the pulses from the CDR source. Shaded blue area represents the sum of the arrivaltime jitter contributions from each frequency component. (b) Zoomed in plot of (a) showing the low frequency components. The 50 Hz line noise is present, as well as some higher harmonics. The relatively large component at 150 Hz possibly originates in a beam position instability, as seen in Fig. 2.5. Low frequency components below 300 Hz contribute around 75% of the total timing jitter. Data taken at the full 101 kHz repetition rate of the accelerator over 1 second, with a beam energy of 24 MeV and a bunch charge of 70 pC.

3.1.3 Laser instabilities and correction

TELBE uses a commercial fs Ti:sapphire laser system provided by Coherent Inc [58]. The system consists of a laser oscillator (Vitara) and a regenerative amplifier (RegA 9000 [57]). The repetition rate of the oscillator was chosen to be 78 MHz to match the 6th harmonic of the master clock speed of the ELBE, which is 13 MHz. This oscillator then provides the seed pulse for the amplifier, and the amplifier provides the laser pulses used in any experiments, with a small portion of the beam diverted for use in the arrivaltime monitor. The laser amplifier system provides 800 nm wavelength pulses with a bandwidth of 10 nm, a 100 fs (FWHM) pulse duration, and pulse energies of up to 6 μJ. The typical repetition rate value is 202 kHz and the specified power drift rate is less than 4% over one hour with a pulse to pulse energy stability of about 2% FWHM [57]. Synchronization between the laser system and the master clock of ELBE is accomplished by a commercial system called Synchrolock-AP, also manufactured by Coherent, Inc [59]. Measurement of phase noise in the synchronization of this system with the master clock showed a timing jitter of 423 fs (FWHM) [60].

The intensity instabilities are corrected, in part, by setting the laser system repetition rate to double the THz rate. This gives two laser pulses per THz pulse. One pulse is used to sample the THz, and the other pulse is not altered and acts as a reference. The two pulses are then subtracted from one another, removing any shared intensity changes originating from the laser system. In this way drifts in the laser intensity at time scales longer than 5 μs are removed. This also reduces the FWHM of the intensity fluctuations in the final data by nearly a factor of 2 [60]. An example of this is shown in Figure 3.6. The correction removes the slower laser instabilities.

Timing instabilities in the laser system are corrected for by the pulse-to-pulse data analysis described earlier. The arrivaltime measurement provided by the arrivaltime monitor gives the relative arrivaltime between the THz and the probe laser, which includes thereby any laser system timing jitter. The laser arrivaltime jitter is not separable from the THz arrivaltime jitter inside the arrivaltime monitor and, accordingly, the phase noise frequencies detected also contain contributions from the laser instability. This has to be taken into account when discussing the potential origin of the phase-noise frequencies in the arrivaltime in Section 3.1.2.

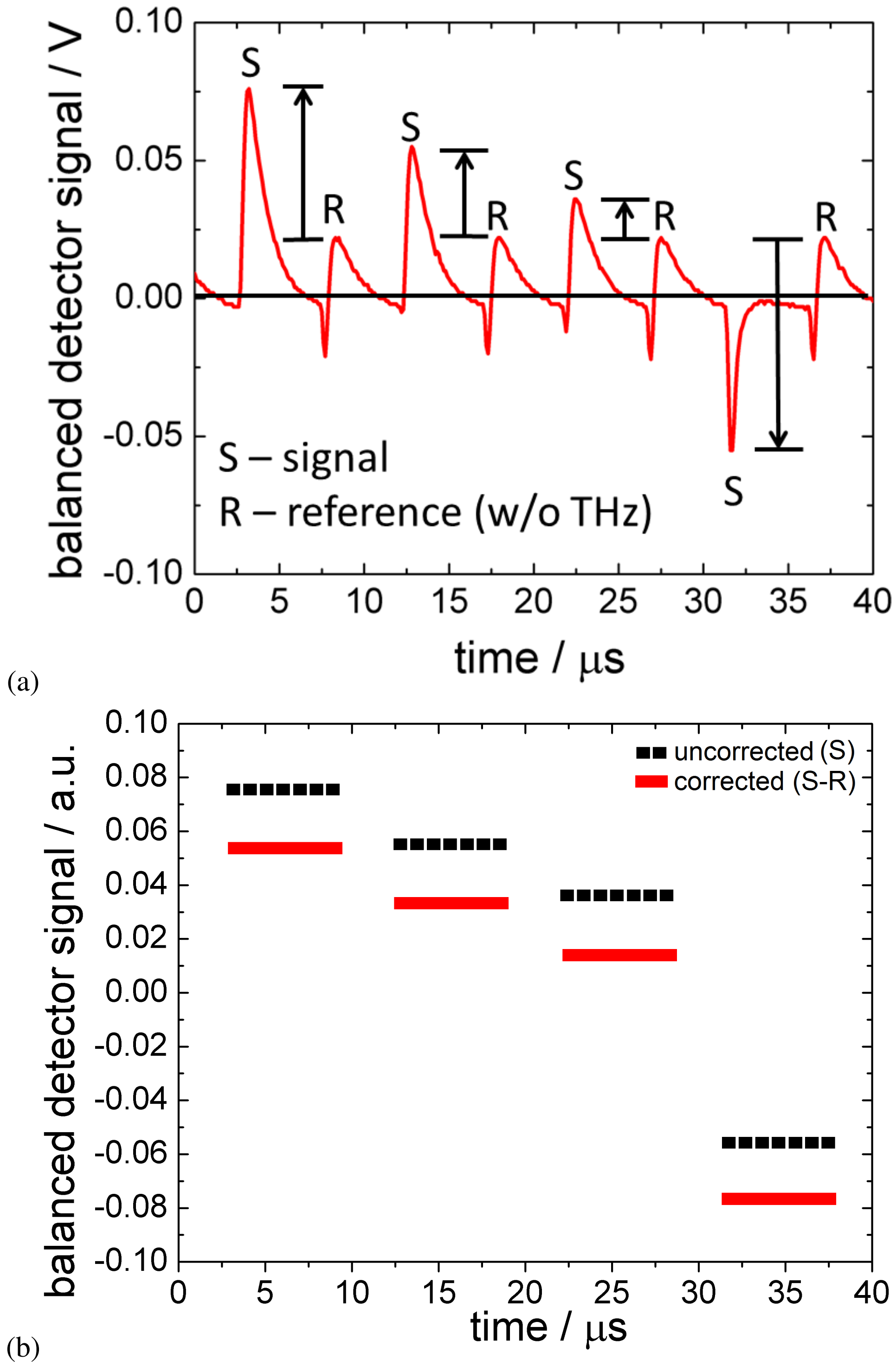

Figure 3.6: (a) Example of the laser intensity fluctuations compensation scheme. This shows a set of 6 measured laser pulses with the laser operating at 202 kHz. The peaks marked with an R are reference signals. These are unmodulated laser pulses that have not been affected by THz. The signals marked S are the signal pulses, which are modulated by the THz pulses. To perform the laser intensity correction, every S pulse has the R pulse that follows subtracted from it. (b) Calculation of the signal for corrected (red) and uncorrected (black dashed) data.

3.1.4 Benchmarking of the Pulse-Resolved Data Acquisition System

The developed monitor systems, in combination with the pulse-resolved data acquisition and data analysis (see Figure 3.7), shall eventually serve to enable world class, ultrafast THz pump-probe experiments. The two most important parameters to establish to this end are the achievable time resolution and dynamic range. Benchmarking these values is an important step to show TELBE to be competitive with laser-based THz experiments in measurement quality, while providing all the additional advantages of an accelerator-driven source, e.g. high repetition rate, unique spectral density, and variable THz pulse form.

First, the benchmarking of the achievable time resolution shall be described. In early pump-probe experiments the time resolution was determined by the cross-correlation of the pump and probe pulse durations because the pump pulses were not carrier envelope phase (CEP) stable [61]. At the low THz frequencies available from TELBE the pump pulse duration is in the few ps (FWHM) regime, which in a classical pump-probe experiment would require a relatively modest synchronization of only 1 to 2 ps (FWHM). In contrast, the THz pulses from TELBE, as well as from most laser-based THz sources, are carrier-envelope phase (CEP) stable. This allows study of phenomena on sub-cycle timescales, which is an important new field in THz research [3]. The time resolution in these modern THz pump-probe experiments in this case is given solely by the duration of the probe laser pulses and the accuracy of the arrivaltime measurement. The current probe laser pulse duration is 100 fs (FWHM), but an eventual upgrade to shorter pulse duration is already being discussed. It is therefore important to establish the timing accuracy of the arrivaltime monitor on few 10 fs (FWHM) timescales.

In order to verify a time resolution in the few 10 fs (FWHM) regime, despite the currently available 100 fs (FWHM) probe pulse duration, two different approaches were chosen. First, the effect of shifting the CDR pulse arrivaltime, acting as a timing signal, against the temporal position of the electric field of the undulator pulses, as determined by sequential electro-optic sampling (EOS), was explored (see Figure 3.8). This was done by shifting the CDR pulses in time with an opto-mechanical delay stage. At each position of the stage, the electric field of the undulator pulses was measured using sequential EOS. The position in time of the observed electric field was used as a time reference, and the changes in its position were recorded as the CDR pulse was delayed (see Figure 3.8 a). The resulting shifts are shown in Figure 3.8 b. The thereby observed deviation from the expectation value is less than 30 fs (FWHM), as shown in Figure 3.8 c.

The second approach involves analyzing the arrivaltime-corrected data from a sequential EOS measurement of the electric field of a 0.9 THz undulator pulse (see Figure 3.9). The time-slice at the zero crossing is another representation of

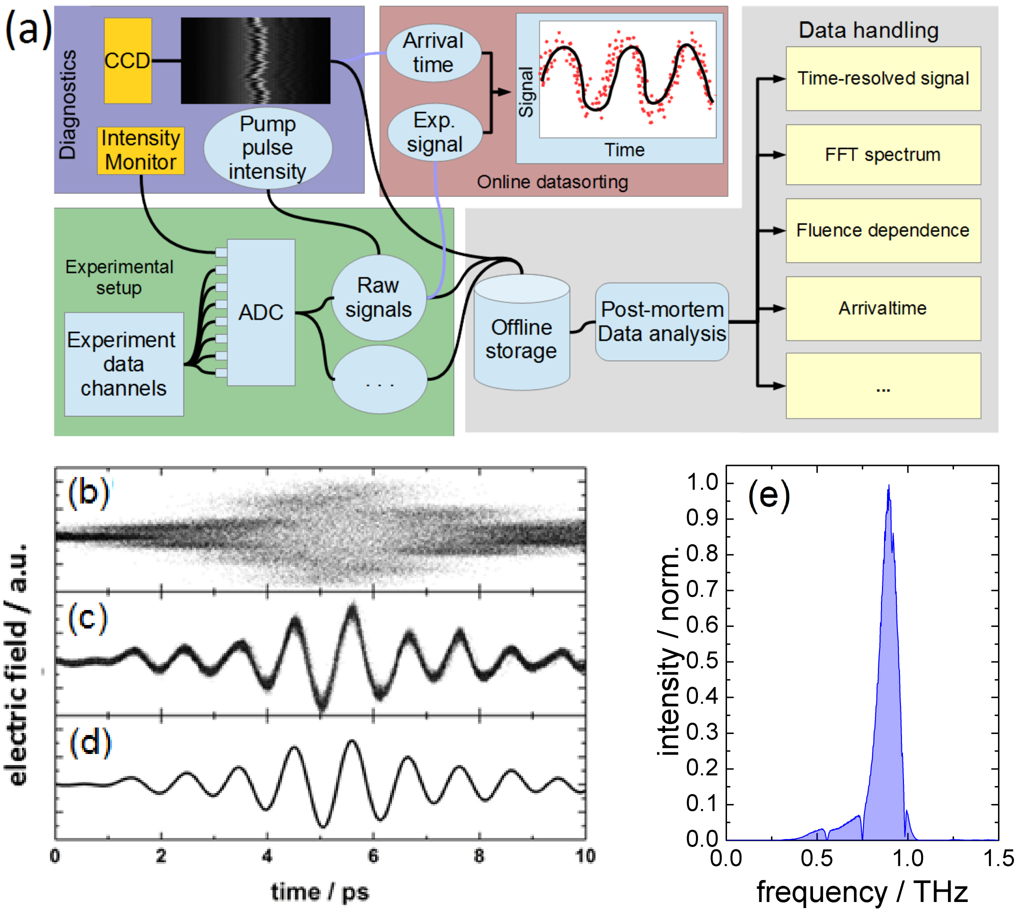

Figure 3.7: (a) Schematic of the pulse-resolved data acquisition system developed in this work. This diagram shows how the arrivaltime and intensity monitors are integrated into the experimental setup. The current system is capable of recording up to eight experimental data channels per pulse at a maximum repetition rate of 101 kHz. After acquisition the data is immediately written to disk, where it can be processed later. Presently no data can be taken while writing to disk and the writing process is slower than the data acquisition by a factor of about 3. The system hence currently has a duty cycle of about 25%. The system is also capable of online data sorting, at the cost of slowing down data acquisition. (b) Raw, unsorted data from a sequential EOS measurement of a 0.9 THz undulator pulse. Timing data is solely from the optical delay stage position. (c) Same measurement after the arrivaltime data from the monitor is added to the individual points. This provides a much more accurate picture of the pulse by adding more accurate timing data. (d) Same measurement again, but with the points collected into 50 fs wide bins and averaged. This reduces the intensity noise. (e) Shows the spectrum obtained from the time-resolved measurement in (d). Taken from [7].

the accuracy of the timing correction. Assuming that intensity fluctuations can be fully corrected or neglected, the time-slice distribution should also yield a value of 30 fs (FWHM). A slightly large value of 50 fs (FHWM) is observed, likely because of contributions from intensity instabilities, as shown in Figure 3.9 b.

The experimentally established achievable time resolution of 30 fs (FWHM) is fully competitive with all-laser-based THz pump-probe setups. In the following it shall be analyzed which individual contributions add up to this value to establish how the time resolution can be further improved.

The limit for the intrinsic minimum timing accuracy $\Delta t_{experiment}$ to be achieved by the arrivaltime monitor shown earlier in Figure 3.1 can be considered as a combination of discrete sources of jitter. Considered this way, the total experimental minimum jitter is a combination of the intrinsic jitter between the undulator pulses and the CD radiator $\Delta t_{intrinsic}$, the transport jitter arising from small instabilities in the separate optical paths in the monitor $\Delta t_{transport}$, and the temporal resolution of the utilized single shot EOS technique $\Delta t_{monitor}$. This can be represented as the following equation:

$$\Delta t_{experiment} = \left(\Delta t^2_{intrinsic} + \Delta t^2_{transport} + \Delta t^2_{monitor}\right)^{1/2} \tag{3.1}$$

where $\Delta t_{experiment}$ is the minimum time resolution for the experiment. The intrinsic jitter between the undulator pulses and the CD radiator is difficult to measure directly as detection of both pulses in the single shot EOS leads to strong interferences. The thereby determined value of 58 fs (FWHM) [6] can hence only serve as an upper limit. However, another likely better estimate can be derived from an earlier experiment at the FLASH FEL which also combined two independent radiators, placed sequentially in a linear accelerator, in an ultra-fast pump-probe experiment. In this case the first radiator was a VUV undulator, and the second radiator was a superradiant THz undulator. THz streaking [62] allowed the deduction of an intrinsic synchronization between the two radiators of 12 fs (FWHM) including several 10 meters of beam transport.

The temporal resolution of the single shot electro-optic sampling can be estimated from several factors. These are parameters such as the length of the chirped laser pulse, the characteristics of the spectrometer, and the pixel size of the readout line camera. The setup at TELBE uses a pulse stretched to 8 ps (FWHM), and the spectrometer outputs a line just under 1 cm in length. Combined with a pixel size of 10 μm, this gives a final temporal resolution of the monitor of $\Delta t_{monitor}$ = 12 fs. Figure 3.10 a shows one method for obtaining an upper limit on the temporal resolution of the monitor. The points from the zero-crossing of a 0.9 THz pulse are taken and their line width analyzed. The calculated 56 fs (FWHM) distribution is an upper limit, likely broadened from the previously measured 30 fs (FWHM) by fluctuations in the electric field measurements. Figure 3.10 b shows four images

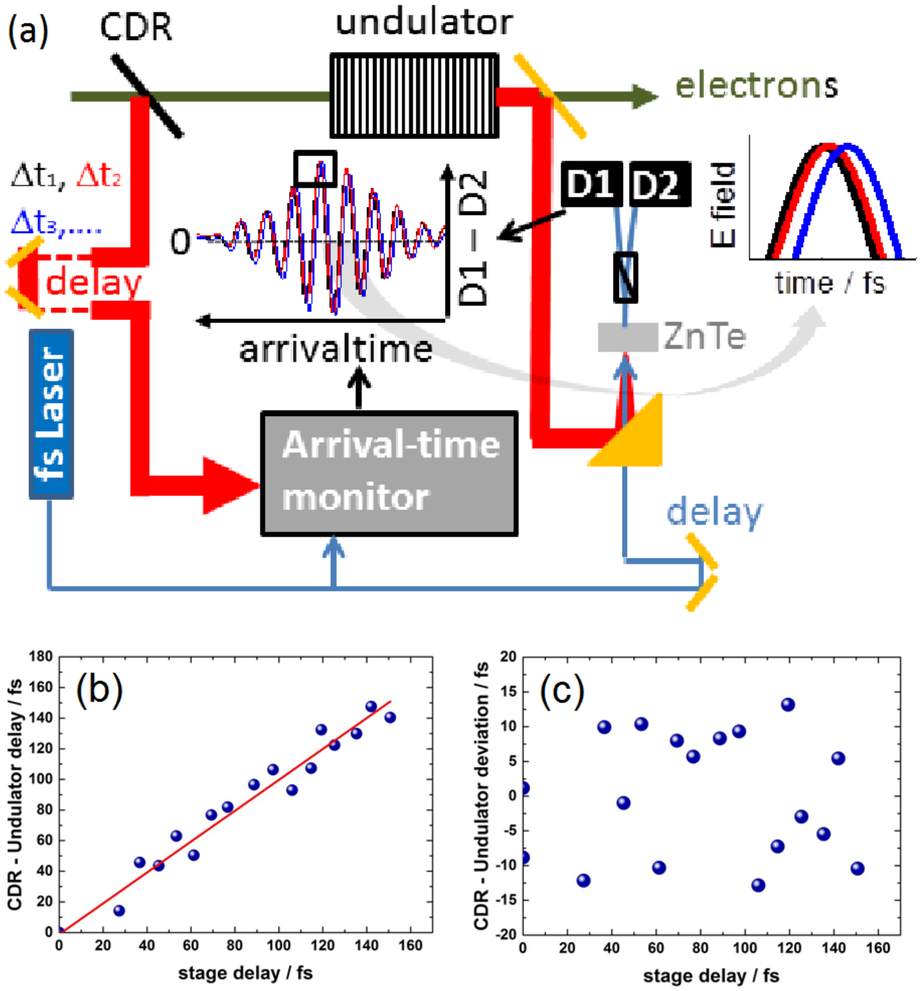

Figure 3.8: (a) Sketch of the scheme employed in THz pump laser probe experiment, with the inset showing an example of the area of the THz pulse used to determine relative arrivaltime (b) Measured CDR pulse delay (red line) versus the observed temporal position of the pulses from the undulator after arrivaltime correction. This establishes an uncertainty/jitter of less than 28 fs (FWHM) [7]. (c) Deviation between the expected value from the CDR delay position and the observed time shift of the undulator pulses. Taken from [6] [7].

from the arrivaltime detector of CDR pulses, taken 10 μs apart. Zooming in to the peak shows the limit of the resolution of the arrivaltime monitor, which is 12 fs.

The final contributor to the experimentally observed jitter $\Delta t_{transport}$ stems from the several meters long independent laser beampaths inside the TELBE laboratory. In the current setup the arrivaltime monitor and the experiment are on two separate laser tables at opposite corners of the laboratory. Assuming the earlier derived estimates for $\Delta t_{monitor}$ and $\Delta t_{intrinsic}$, as well as the experimentally observed $\Delta t_{experiment}$ value of 30 fs (FWHM), yields a 25 fs (FWHM) contribution for this component, which in general compares well to measurements performed on the stability of the laser paths. One can therefore state that the experimentally observed time resolution can be well understood assuming reasonable contributions of different obvious jitter sources. There is obviously room for improvement which could yield an eventual time resolution of 1 fs (FWHM) or better as discussed later in the outlook section.

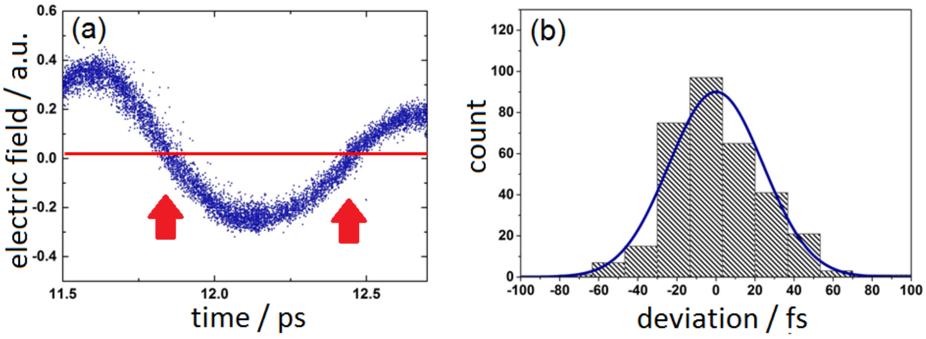

Figure 3.9: Benchmarking of the time resolution. (a) A zoom into the jitter-corrected electro-optic sampling data of 0.9 THz undulator radiation. The temporal width of the distribution at the zero crossing is an estimate for the achieved time resolution of 30 fs (FWHM). (b) Slice through the distribution of the arrival times at the zero-field crossings at 11.8 ps and 12.5 ps yielding a temporal resolution of 56 fs (FWHM). Taken from [7].

Of equally crucial importance for the eventually planned THz pump-probe experiments is the achievable data quality, typically expressed as dynamic range. Dynamic range is defined here as the ratio of the maximum signal to the noise level [63]. The experiment chosen to illustrate the dynamic range achievable at TELBE was a sequential EOS measurement of a 0.9 THz pulse from the undulator. Data from an area with no signal, approximately 11-12 ps before time zero, was compared to the maximum signal measured from the undulator pulse (see Figure 3.11). From the time domain measurement shown in Figure 3.11 a, a dynamic range of 1/(5.5e-5) = 20000, or 86 dB, can be deduced. Evaluation of the frequency domain data shown in Figure 3.11 b shows that up to the third harmonic of the undulator can be observed, together with the water absorption lines up to 3 THz. This yields a dynamic range in the frequency domain of at least 1/1e-6 = 1000000, or 120 dB. These values compare well to all-laser based THz time-domain setups. [63].

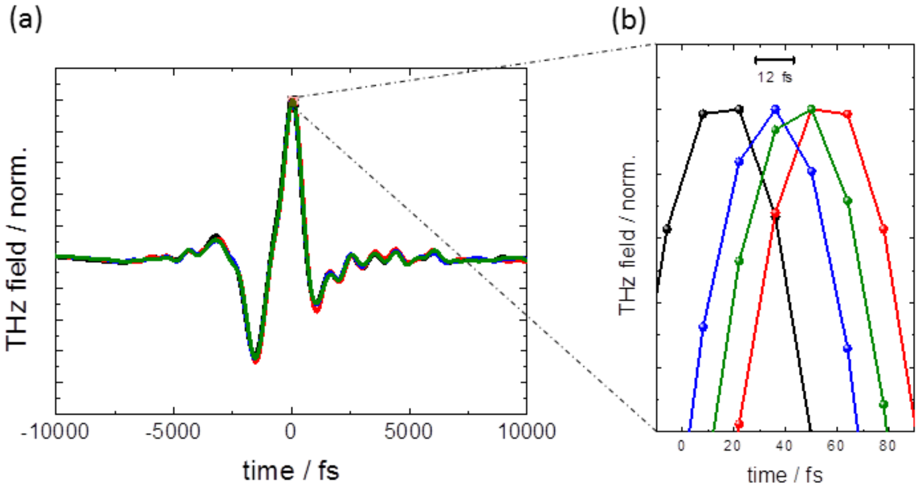

Figure 3.10: (a) Four consecutive single-shot measurements of THz pulses from the coherent diffraction radiator. (b) Magnified section around the signal maxima. They show the temporal resolution of the spectral decoding setup resulting from the combination of chirp, spectrometer characteristics, and pixel size of the readout camera. The repetition rate in these measurements was 100 kHz. Taken from [7].

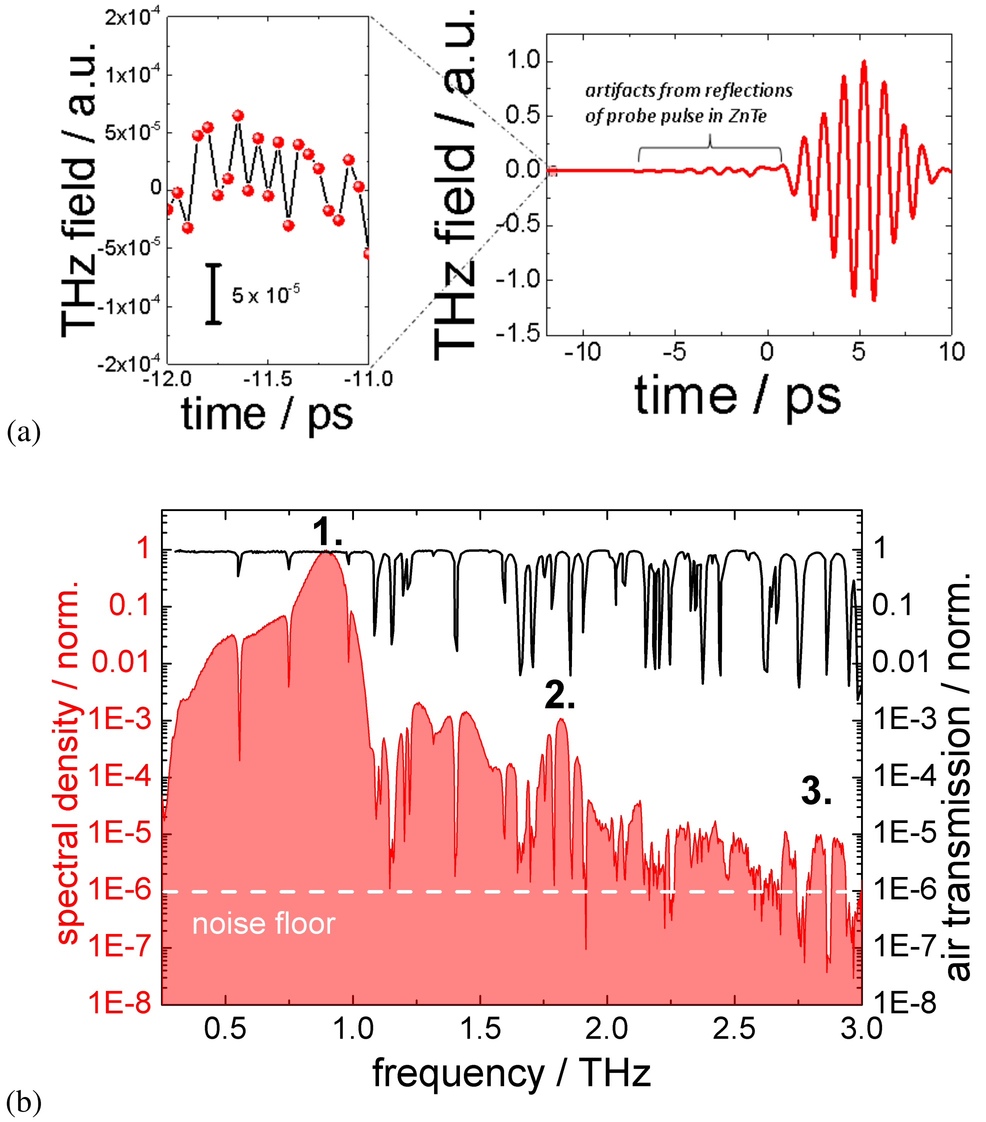

Figure 3.11: (a) Benchmarking the dynamic range in the time domain. THz-electro-optic measurement of the radiation emitted from the undulator source tuned to a frequency of 0.9 THz (right) and a zoomed view of the 11-12 ps time interval before the temporal overlap of the THz pump and laser probe (left). This time is sufficiently early to avoid interference from artifacts due to reflections of the probe laser in the electro-optic crystal. This measurement gives a dynamic range of 4e8, or 86 dB, in the time domain. (b) Benchmarking the dynamic range in the frequency domain. Resulting THz frequency-domain spectrum when evaluating the full time-domain measurement over 120 ps on the left, and plotted on a logarithmic scale with water absorption spectrum on the right. Higher harmonics up to the 3rd order are observed. The measurement was performed in atmosphere and the narrow water absorption lines are clearly resolved up to 3 THz. The dashed white line represents the detection limit. This measurement thereby gives a dynamic range of better than 1000000, or 120 dB, in the frequency domain. Taken from [7].

3.2 Characterization of TELBE sources

There are different fundamental characteristics of THz sources that make them interesting candidates for studying linear and nonlinear THz-driven phenomena, namely the spectral content, beam profile, and intensity. Aside from these, the achievable stability and the achievable time resolution are also of crucial importance. Accelerator-based photon sources can have superior photon beam parameters compared to tabletop sources, however the challenge lies in the often large instabilities and poor synchronization with fs laser systems that can diminish these advantages. At TELBE these instabilities are measured pulse-resolved and can be corrected providing an excellent dynamic range and time resolution (see previous chapter). Analysis of the characteristic frequencies of these instabilities may help in identifying their fundamental origin and assist with their subsequent removal. This would help to reduce the big data challenge that comes with the pulse-resolved data acquisition, as is discussed in the outlook of this thesis. The final section of this chapter is devoted to this analysis. In the following the properties of the two superradiant THz sources at TELBE, the coherent diffraction radiator and the undulator, are examined and their characteristics measured. For each source the results from calculations are presented first, and then compared to the experimentally derived parameters.

3.2.1 Undulator

The fundamentals of undulator emission characteristics are described in the basics section 2.2.2. Here properties, resulting from the specific design of the TELBE undulator beamline in combination with superradiance, are discussed and compared to the experimentally observed parameters. The TELBE THz facility aims to produce a frequency range from 0.1 to 3 THz. The electron beamline around the THz radiators and the THz photon beamlines are hence built specifically to have a suitably large acceptance angle. The acceptance angle of 71 mrad provided for the undulator source leads to the situation that a considerable amount of radiation outside the so-called undulator cone of the fundamental wavelength (see equation 2.16 for details) is received in the TELBE laboratory. The undulator is furthermore operated with K-values exceeding 1 and hence starts to exhibit wiggler-like parameters [35]. This results in a much richer harmonic spectrum than expected for classical undulator radiation. The spectral content and the beam profile can be calculated by numerical simulations using the Synchrotron Radiation Workshop (SRW) software [64] (see Figure 3.12). At small opening angles the expected harmonic spectrum for undulator radiation is observed. At the acceptance angle of 71 mrad, which corresponds the the TELBE undulator beamline, a quasi-continuous spectrum made up of the broadening of even and uneven harmonics appears (see

Figure 3.12 a). Note that the fundamental and all uneven harmonics exhibit a bell-shaped beam profile (see Figure 3.12 b), while all even harmonics have no intensity in the center of the beam (see Figure 3.12 c).

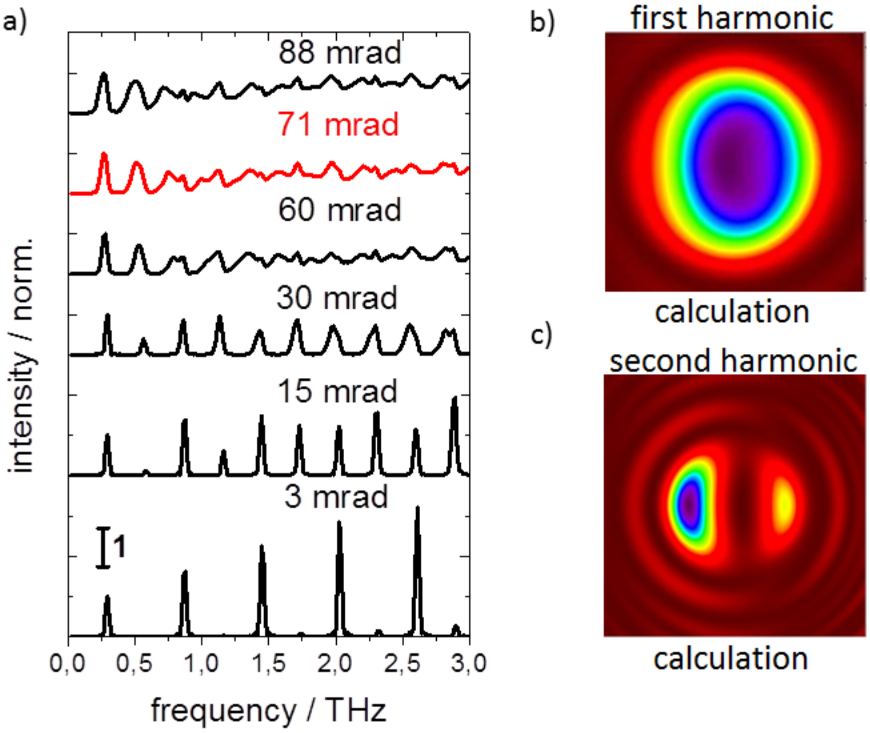

Figure 3.12: a) Calculated harmonic spectra of the undulator radiation for different acceptance angles. The acceptance angle realized in the TELBE facility is 71 mrad (marked in red). Wider and narrower acceptance angles are shown to illustrate the relationship between this parameter and the harmonic content of the undulator beam. b) Calculation of a beam profile of the fundamental for a tune to 0.37 THz. c) Calculation of a beam profile of the second harmonic of a tune to 0.68 THz. Calculations were carried out using Synchrotron Radiation Workshop (SRW) [64], a numerical radiation modeling software package. All calculations assumed a beam energy of 24 MeV, with b) and c) using the 71 mrad acceptance angle of undulator beamline at the TELBE facility. Taken from [6].

A typical experiment aims at utilizing the laser-like fundamental or first harmonic, while the rest of the harmonic spectrum is neglected and often even filtered out. The undulator at TELBE [65] is designed to be tunable through a broad range of fundamental frequencies between 0.1 and 3 THz, and the emission characteristics also depends on the undulator frequency. Figure 3.13 shows a simulation of the dependence of the intensity in the fundamental frequency on the undulator tune. The simulations used the SRW numerical simulation software package [64]. This simulation shows that the intensity of the fundamental of the TELBE undu-

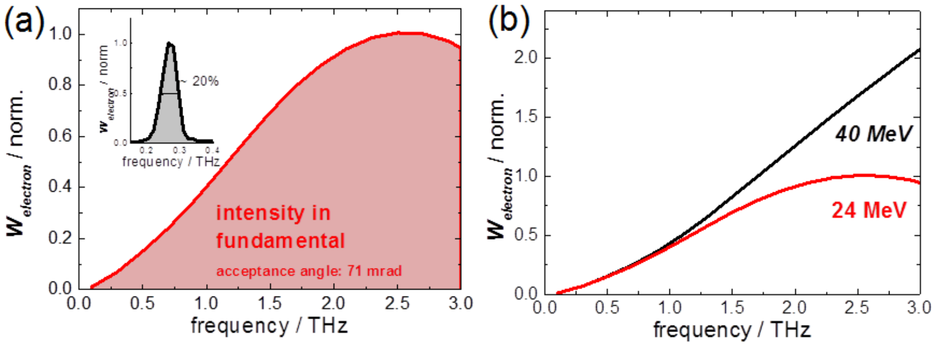

Figure 3.13: (a) Calculated intensity in the fundamental of undulator tunes between 0.1 and 3 THz (red-shaded) with a beam energy of 24 MeV. (inset) Calculation of the spectrum of an undulator fundamental for a tune to 0.28 THz with a beam energy of 24 MeV (b) Effect of electron beam energy on intensity in the fundamental of undulator tunes between 0.1 and 3 THz. 24 MeV (red) is the commonly used beam energy setting, and 40 MeV (black) is the design maximum beam energy for ELBE. All calculations used the SRW numerical simulation software package [64], and assume an undulator beamline acceptance angle of 71 mrad. Adapted from [6].

lator peaks around 2.5 THz for a typical beam energy of 24 MeV. The emission characteristics also depend on the beam energy [36]. The peak of the emission shifts to the higher frequencies with increasing beam energy as is shown in Figure 3.13 b. If higher THz frequencies are required one should hence operate at the highest possible beam energy available, which at ELBE is 40 MeV. As described earlier in the basics chapter the overall frequency spectrum is dominated by the superradiance and hence the bunch formfactor. This is shown in Figure 3.14 where the calculated undulator spectrum is compared to an experimental measurement. As can be seen, the higher harmonic spectral content is largely suppressed by the bunch formfactor.

Measured properties

An important feature of any light source is the beam profile. This affects, amongst other things, the ability to achieve a small focus, which is of critical importance in the high-field THz experiments performed at TELBE. Figure 3.15 shows the beam profile of the undulator fundamental for a tune of 1.4 THz taken with a THz beam profiler. The measurement proves the bell-shaped intensity distribution expected from the calculations. At 1.4 THz, spot sizes below 300 μm have been achieved (depending on the utilized focusing elements).

Figure 3.16 shows the measured spectral content of different undulator fundamentals between 0.15 and 2.5 THz. This illustrates the tunability and narrow

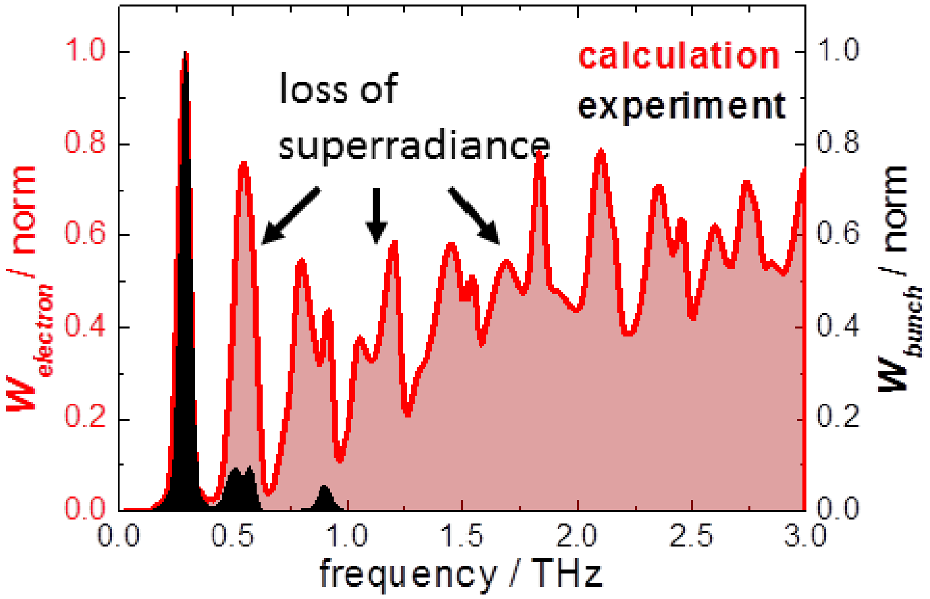

Figure 3.14: Comparison of a calculated spectrum (red-shaded) and a measurement for a tune to 0.28 THz (black-shaded). The calculation does not include the bunch formfactor. The suppression of higher harmonic content observed in the experiment is due to the decrease of the bunch formfactor. Note all the calculations were performed assuming a beam energy of 24 MeV and a beamline acceptance angle of 71 mrad. Taken from [6].

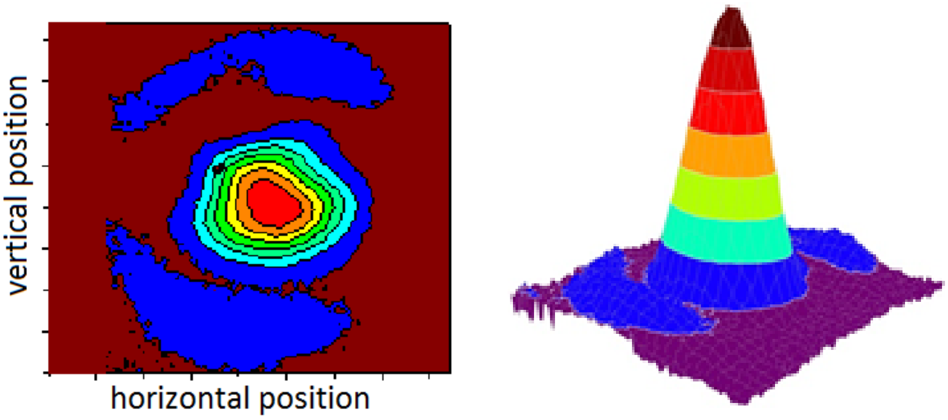

Figure 3.15: Beam profile of 1.4 THz undulator tune measured at TELBE using a SPIRICON THz beam profiler [50]. The expected bell-shaped intensity distribution is observed. Adapted from [6].

bandwidth achievable at TELBE. As is shown later, the spectral density of these fundamentals can exceed those of tabletop sources by more than one order of magnitude [6]. Another important property is the inherent carrier-envelope-phase (CEP) stability. When utilizing the pulse-resolved data acquisition and correction developed in this work, the CEP-stable multi-cycle THz transients shown in Figure 3.16 b can be measured with 30 fs (FWHM) time resolution.

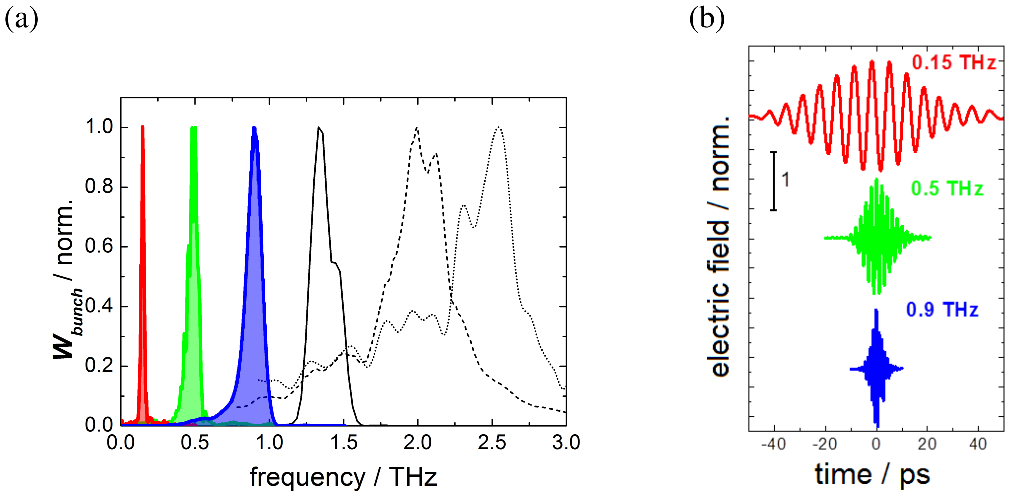

Figure 3.16: (a) Spectra of the THz pulses for undulator tunes of 0.15 THz (red), 0.5 THz (green), 0.9 THz (blue), 1.4 THz (black), 2.1 THz (dashed), and 2.5 THz (dotted).
(b) Electric field transient of undulator pulse for the first three undulator tunes shown in in a. The top two electric field transients were measured through 20% band-pass filters around the center frequency to filter out the harmonic spectrum. Adapted from [6].

An illustration of the unique parameter space TELBE operates in is shown Figure 3.17. Although not operating yet with the design bunch charge of 1 nC, pulse energies beyond 1 μJ are achieved at 100 kHz repetition rate. This is two orders of magnitude higher than any laser-based THz source operating at the same repetition rate. The pulse energy is furthermore concentrated in a narrow frequency bandwidth, leading to a unique spectral density. Shown in Figure 3.17 a is the scaling between bunch charge of the electron bunches driving TELBE and the resulting pulse energies. In the superradiant regime this scaling should go with the power of 2. Because the spontaneous radiation is orders of magnitude weaker, the nonlinear dependence is also observed for only partially superradiant regimes, while the actual observed intensity is of course lower.

As described in section 2 and shown in Figure 3.16, the spectral content and the overall pulse energy emitted are dominated by the superradiance or the form-factor, respectively. The currently achievable maximum pulse energies for the TELBE undulators are shown in Figure 3.17 b. The observed maximum values are, aside from the form factor, determined by the bunch charge, which is cur-

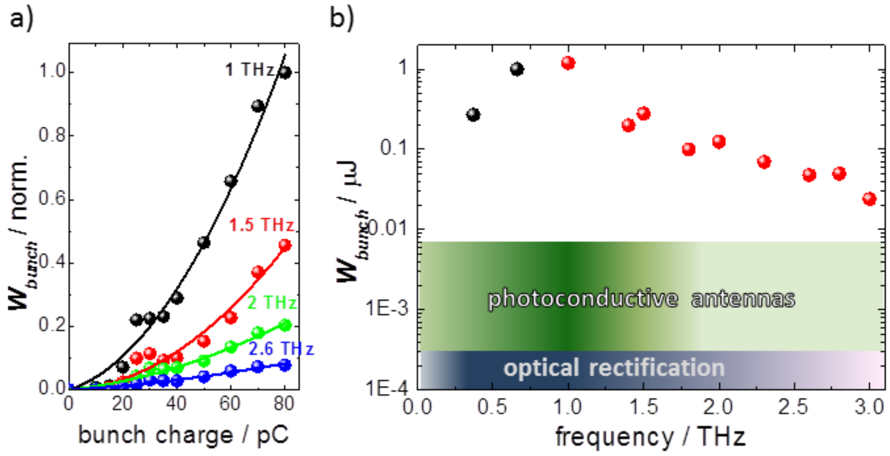

Figure 3.17: Dependence of pulse energy W_{bunch} on bunch charge and THz frequency. a) Measured charge dependence of the emitted THz pulse energy in the fundamental for undulator tunes between 1 and 2.6 THz and 2nd order polynomial fits. b) Maximum pulse energies observed during the first commissioning shifts of the prototype facility (full circles) at a repetition rate of 100 kHz and with a bunch charge of 100 pC. The already demonstrated pulse energies exceed the currently most intense high-repetition-rate laser-based sources (shaded) by up to 2 orders of magnitude. Note, the laser-based sources are broadband and have a distribution of spectral weight over many frequencies as indicated by the color tone in the respective shaded areas. Experiments aiming at driving a narrowband low frequency excitation resonantly thereby benefit additionally from the considerably higher provided spectral density. Taken from [6].

rently limited to 100 pC. Nevertheless, the observed pulse energies exceed those of table-top laser-based THz sources with the same repetition rate by 2 orders of magnitude. As can also be seen the THz intensities rapidly decrease for frequencies above 1 THz due to the loss of formfactor, and hence superradiance. The decrease towards lower frequencies likely stems from the emission characteristics of the undulator shown in Figure 3.13 as the formfactor can be considered to be unity, and the diffraction losses for the Gaussian beam-like undulator radiation are negligible down to 300 GHz.

3.2.2 CDR / CTR source

The CDR/CTR (see section 2.2.2 for more information) source at TELBE was designed to be a broadband THz source which can operate alongside the undulator. The diffraction screen has comparatively large dimensions of 215 x 150 mm and a central aperture of 4 mm. The acceptance angle of the beamline is 300 mrad.

This shall allow the efficient generation and transport of a THz spectrum down to 100 GHz to the TELBE laboratory. Figure 3.18 shows an analytical calculation of the spectral content of the TELBE DR/TR source. When using the diffraction radiator (DR) it is possible to generate spectral content in usable amounts up to 2 THz while only minimally affecting the quality of the electron beam passing through. In fact, as is shown later, the same electron bunch can then be used to emit a pulse from the undulator source a few meters downstream without an observable degradation of THz pulse parameters. Higher frequencies and intensities can also be generated when operating the screen as a coherent transition radiator. For this mode, the screen is moved upwards by 1.2 cm so that the electron beam is impacting the screen. In this case a flat response of the emission characteristics is expected at higher THz frequencies. The drawback is that operation as a CTR source does not allow parallel operation of the undulator and all of the electrons are lost in, or in close vicinity to, the screen. Towards lower frequencies DR and TR emission falls off in a similar manner due to diffraction effects during beam transport. The emitted spectrum of the diffraction radiator also depends on the beam energy, as shown in Figure 3.18 b. As is also the case for undulator radiation discussed earlier, higher beam energies will help to generate higher THz frequency components. A beam energy of 40 MeV would allow generation of usable THz intensity up to 3 THz.

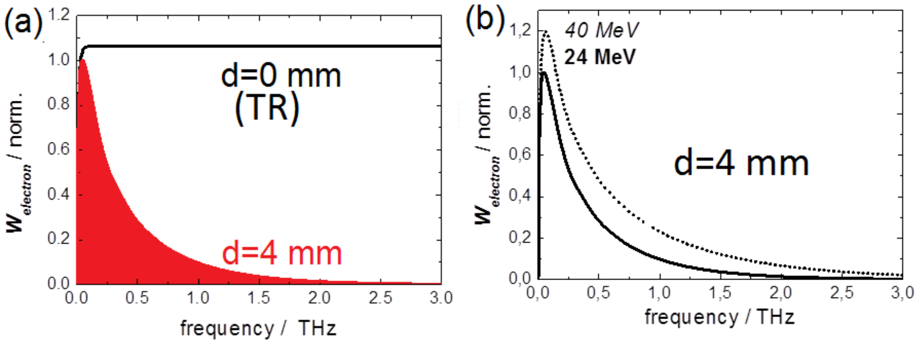

Figure 3.18: (a) Calculation of the intensity spectrum from a DR assuming the screen dimensions and aperture size employed at the prototype facility. Calculation performed with a beam energy of 24 MeV and the corresponding acceptance angle of the DR optical beamline, which at TELBE is 300 mrad. Shaded spectrum is for a diameter of 4 mm, which matches the physical setup of the radiator at TELBE. (b) Calculation of the dependence of the spectrum on the electron beam energy. Calculations were performed in Matlab using the analytical equations [27] shown in section 2.2.2. Adapted from [6].

Figure 3.19 shows calculations of the expected beam profile of coherent diffraction radiation assuming different polarization filters. The beam profile of diffraction (and also transition) radiation forms a donut-like shape with zero intensity

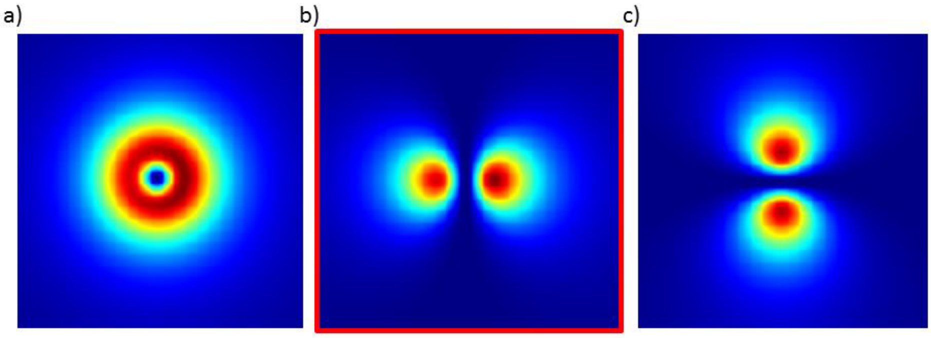

Figure 3.19: Analytical calculations of the beam profiles for diffraction radiation for a) the full beam, b) the horizontal polarization component and c) the vertical polarization component. Calculations were performed in MathCAD using the formulation that appears in [66] and including the specific screen dimensions and aperture size for the TELBE DR source. Adapted from [6].

in the center and radial polarization (for details see section 2). The THz beam at TELBE passes through two Brewster-angle windows in the beamline into the TELBE laboratory that are mounted in a geometry that causes a predominant horizontal polarization. Figure 3.19 b represents the beam profile that in this case is expected in the TELBE laboratory. Filtering of one polarization component of the radially polarized beam results in the appearance of an asymmetric two-lobed beam profile.

Measured properties

Figure 3.20 shows a comparison between the calculated, spectral content of a DR pulse and a typical spectrum measured in the TELBE laboratory. The calculations assume the DR screen dimensions and beamline acceptance of the TELBE facility, and neglect diffraction and superradiant effects. Most of the difference between calculation and experiment at low frequencies can be attributed to diffraction effects, while higher frequency losses are likely due to the loss of superradiance. The notches in the spectrum are atmospheric water lines. Figure 3.21 shows a typical CDR beam profile, measured with a THz beam profiler. The expected double-lobed appearance is shown, resulting from selecting the horizontal polarization component of the radially polarized source. Interestingly a relatively deep focus is observed in the TELBE laboratory, as is shown in Figure 3.22. This likely is caused by the 45° tilt of the DR screen, which causes one side of the screen to be closer to the plane of observation than the other.

Figure 3.23 a shows the spectrum derived from the Fourier transform of a time-domain sampled THz pulse. The measurement was performed with a particularly

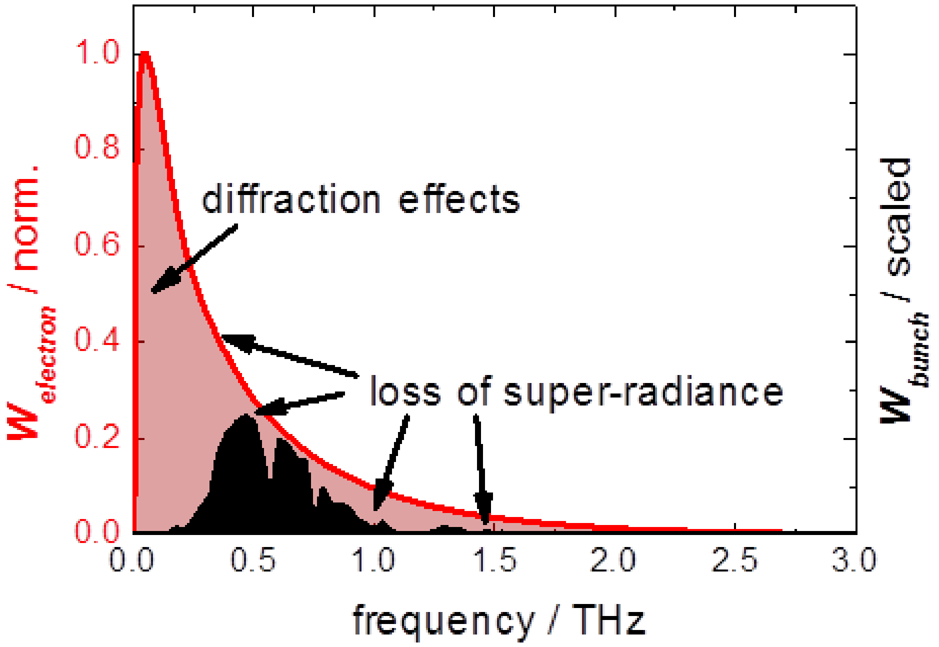

Figure 3.20: Comparison of the calculated spectrum (red-shaded) and a scaled typical measurement (black-shaded). The calculations assume a zero-length bunch, an acceptance angle of 300 mrad, and neglect diffraction in the optical transport and superradiance effects. The notches in the measured spectra are due to water absorption lines. Beam energy was 24 MeV with a bunch charge of 70 pC. Taken from [6].

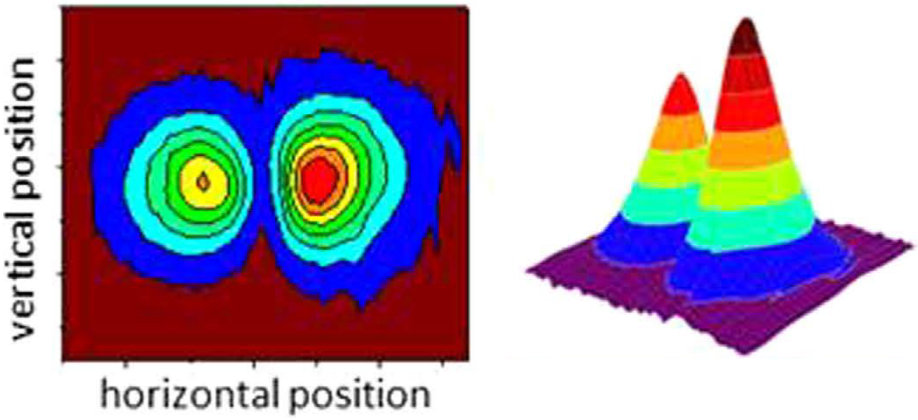

Figure 3.21: Beam profiles of diffraction radiation determined with a THz beam profiler [50]. The expected two-lobed beam profile is observed when measuring the focal position of the right diffraction lobe. Beam energy was 24 MeV with a bunch charge of 70 pC. Adapted from [6]

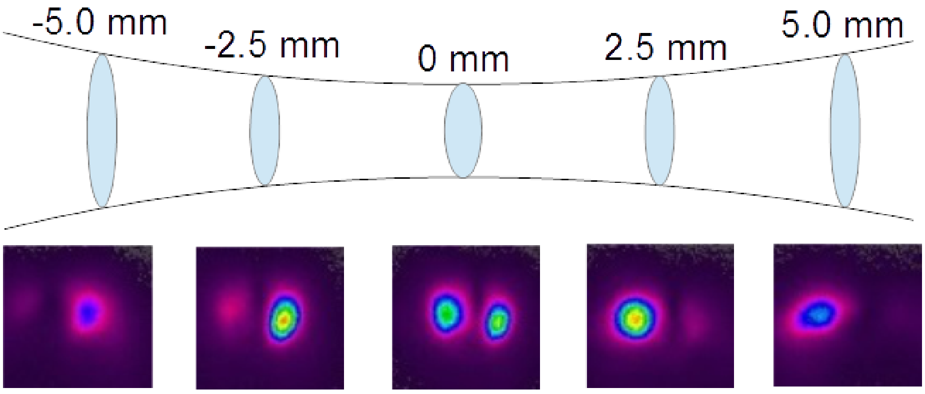

Figure 3.22: Beam profile of the diffraction radiation beam, determined with a THz beam profiler [50]. One can clearly see the changes in the spot shape, size, and intensity as the profiler moves through the focus. The two focus points in the middle image are the two lobes expected when a beam with radial polarization passes through a linear polarizer, which in this case was two Brewster angle windows. Two separate foci for the left and right lobes can be observed. The most likely explanation is that this stems from the fact that the radiation is oriented with an angle of 45° to both the THz and electron beam and hence also represents a ’deep’ source. Beam energy in these measurements was 24 MeV with a bunch charge of 70 pC.

thick electro-optic crystal to avoid diffraction effects in the detection scheme. This particular bunch compression scheme led to a near-ideal quadratic bunch charge dependence (as is shown in Figure 3.23 b).

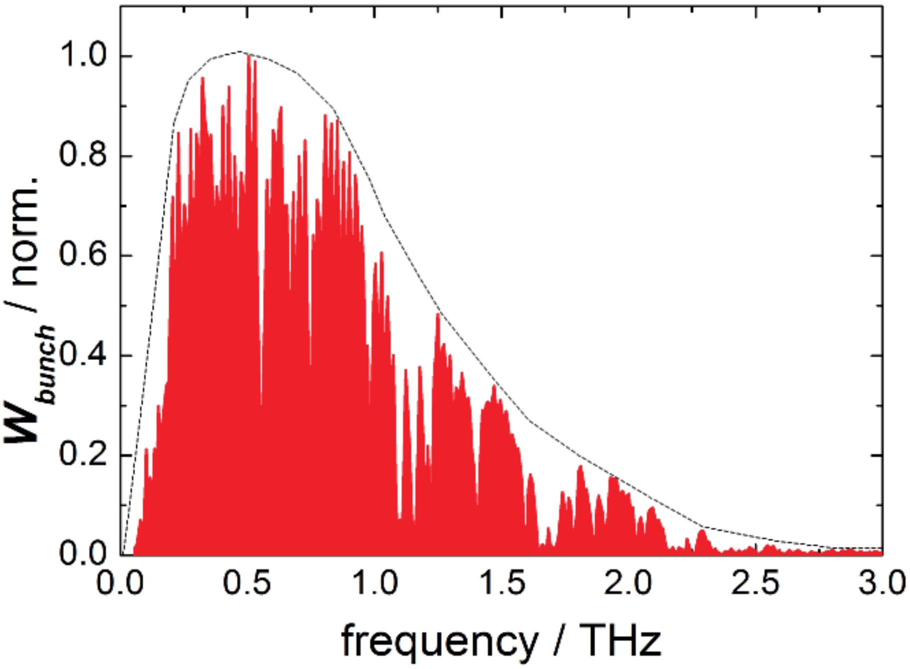

(a)

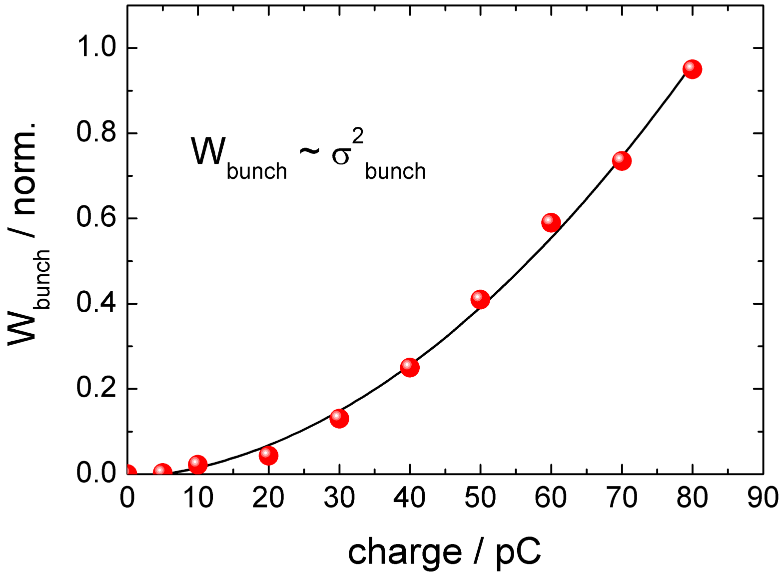

(b)

Figure 3.23: (a) Spectrum of a typical CDR pulse measured by electro-optic sampling. The notches in the frequency domain spectra are due to water absorption lines from passage through air. Additional fringes are due to reflections in the ZnTe crystal. (b) Plot of CDR pulse energy versus bunch charge. The bunch charge was varied from 0 to 80 pC. The expected quadratic relationship between bunch charge and pulse energy is, for this bunch compression scheme, clearly observed. Measurements were performed with a beam energy of 24 MeV. Adapted from [6].

3.2.3 Comparison of Pulse-to-pulse Stability of Undulator and DR source

The TELBE facility currently operates two superradiant THz sources, a CDR/CTR source and an undulator source, which have been characterized individually in the previous sections. As discussed, the THz emission characteristics are distinctly different, offering TELBE users the choice to work with either quasi-single-cycle or multi-cycle THz pulse forms, or even both. In the following, fundamental properties of these two sources that are of vital interest for users of the TELBE facility shall be quantitatively compared. Namely, the maximum achievable pulse energy together with the achievable intensity- and timing-stability. The earlier discussed pulse-resolved data acquisition system developed in this work has been used for the pulse-resolved characterization of the DR source and the undulator source in parallel. Thereby the measurements can be directly compared. At the end of this section the characteristic frequencies of the observed instabilities are discussed in order to get some understanding of their possible origin.

Figure 3.24 shows a measurement of the charge-dependence of the DR and undulator pulse energy source performed in parallel. As can be seen, while the dependence is qualitatively similar, the pulse energy of the diffraction radiator received in the TELBE laboratory is about one order of magnitude lower than that of the undulator. This is, on first sight, somewhat surprising as both sources experience the same bunch formfactor and the actual emission characteristics suggest that the emitted pulse energies emitted from both sources should be on the same order [67]. In the following paragraph an attempt is made to explain this discrepancy.

One important influence is the polarizing effect of the Brewster angle windows which removes the vertical polarization component of the CDR beam and thereby reduces the CDR pulse energy already by a factor of 2. The second dominant origin of loss will be diffraction effects. These losses will be severe, but are hard to quantify. The donut-like profile of the beam will show a much higher degree of diffraction than undulator radiation of the same frequency because the latter is a near-ideal Gaussian-like beam. Furthermore, a considerable part of the spectrum of the CDR is at low frequencies where the formfactor is 1 but diffraction is large (see Figure 3.20).

As can be seen in Figure 3.24, the CDR intensity needed to be scaled by a factor of 8 to bring it in line with the intensity of the undulator. Since the present optical transport of the CDR/CTR beam is based on simulations assuming Gaussian beams, a loss factor of 4 due to diffraction effects is not unrealistic. Another observation is that the observed charge dependence of both sources does not exhibit the expected quadratic behavior. This likely stems from the fact that the actual bunchform for this particular bunch compression setup varies for different bunch charge regimes. It should be noted that quadratic charge dependencies of the pulse energy have been observed for other accelerator settings (see, for example, Figure 3.23 b).

While the absolute pulse energy of the CDR is lower, its pulse-to-pulse energy fluctuations are significantly higher than that of the undulator, as can be seen in Figure 3.25 a, which shows histograms of the intensity changes for both of the sources over a time period of 60 seconds. The undulator exhibits a pulse-to-pulse fluctuation of 13% (FWHM). In contrast the intensity of the CDR source is fluctuating by 21% (FWHM).

One typical origin for intensity instability in superradiant THz sources are fluctuations in the charge or length of the bunches. No evidence for pulse-to-pulse changes in bunch length have been observed in the single-shot THz spectra of the CDR pulses (see Figure B.3 in the Appendix). Hence, to this end one could tentatively assume that the instability of both sources is dominated by fluctuations in bunch charge. Due to the quadratic charge dependence in the superradiant regime a charge instability of 3.6% (FWHM) would be consistent with an instability of 13% (FWHM) as observed for the undulator source. The CDR source sees the exact same electron bunch and hence should experience the exact same relative intensity instability while in fact an instability of 21% (FWHM), a factor of 1.3 higher, is observed. One reason to explain this may be the fact that the CDR source is expected to be more strongly affected by minimal instabilities in the electron beam position, since in the current ELBE accelerator the diameter of the electron beam is only slightly smaller than the 4 mm aperture in the DR screen. Already if small portions of the electron beam impact on the DR screen transition radiation is generated which has a significantly higher intensity than diffraction radiation and leads to an increase in the total intensity from the source. At the same time the intensity of the undulator should drop because some charge is thereby lost. The measurement of the intensity drifts on a minute timescale shown in Figure 3.25 b clearly indicates that this process is actually occurring. As can be seen, this type of instability affects the undulator intensity by roughly one order of magnitude less. This can be tentatively understood when considering that transition radiation actually adds frequency components to the CDR radiation (see Figure 3.18). An analysis of the observed distinct noise frequencies of the instability shows that some of the strongest intensity instabilities of the CDR radiation (e.g. one with the line frequency of 50 Hz) also exhibit the characteristic out-of-phase behavior. The additional instability of the CDR source can therefore tentatively be attributed to instabilities in beam position, which show up predominantly in the CDR pulse intensity while affecting the undulator pulse energy only in a negligible way.

The timing stability between the undulator and CDR source is difficult to measure directly in parallel because the THz pulses from both sources interfere in the spectral decoding setup, leading to erroneous results. In the future a second parallel operating arrivaltime monitor is planned which would allow a clean measurement of the CDR and undulator jitter in parallel. Despite the technological challenges, direct measurement of the timing jitter between the CDR and undulator sources has been attempted and gave the results shown in Figure 3.26. The observed timing jitter of ~ 50 fs (FWHM) is clearly larger than the upper limit achieved in the indirect benchmarking experiment discussed earlier in Figure 3.9. As is discussed in section 3.1.4, most of the arrivaltime jitter is probably resulting from constraints given by the bandwidth of the fs-laser and the pixel size of the camera in the spectral decoding setup, as well as instabilities in the optical transport of the fs laser, so that the actual intrinsic jitter between CDR and undulator may be well in the sub-10 fs (FWHM) regime and hence similar to values observed in a similar arrangement in the FLASH X-ray FEL [62]. While this intrinsic jitter is very small, the jitter of the THz pulse from both sources with respect to the synchronized fs-laser is larger than 1 ps (FWHM) (see Figure 3.4).

To summarize, the intensity/pulse energy of the undulator source is roughly one order of magnitude (factor of 8) higher than that of the CDR source, which can be tentatively understood from polarization filtering and diffraction losses in the optical transport into the TELBE laboratory. The pulse-to-pulse stability of the intensity is, with 13% (FWHM), considerably better for the undulator source than for the CDR source with 21% (FWHM). The origin for this is likely the stronger impact of the beam position movements on the intensity of the CDR source. Finally, the arrivaltime jitter of the two sources, with respect to the RF-synchronized fs laser system, is equivalent. It can only be measured directly for the CDR source and, as can be seen in Figure 3.4, exhibits a value of 1.4 ps (FWHM) when measured over 1 second.

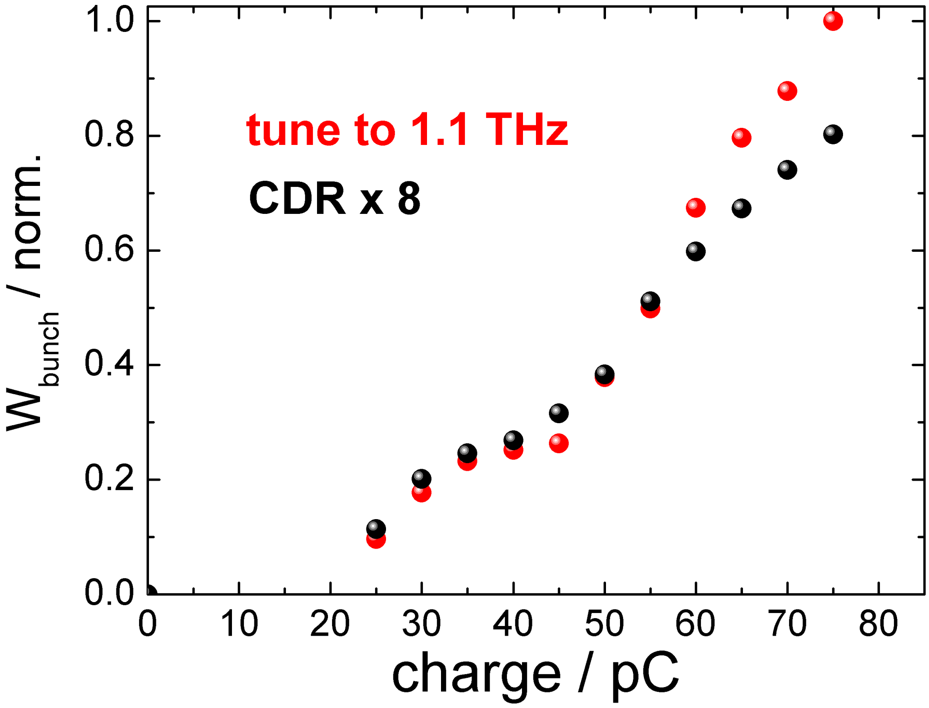

Figure 3.24: Comparison of the charge dependence of the pulse energy for an undulator tuned to 1.1 THz and the coherent diffraction radiator (CDR). The pulse energy of the CDR source has been scaled by a factor of 8 to line up with undulator power. As can be seen, CDR and undulator pulse energies show qualitatively the same charge dependence. The charge dependence is not showing a simple quadratic behavior, indicating a change of bunch form with increasing charge for this specific bunch compression. Note that for other accelerator settings near-ideal quadratic charge dependencies have been observed, as e.g. shown in Figure 3.23.

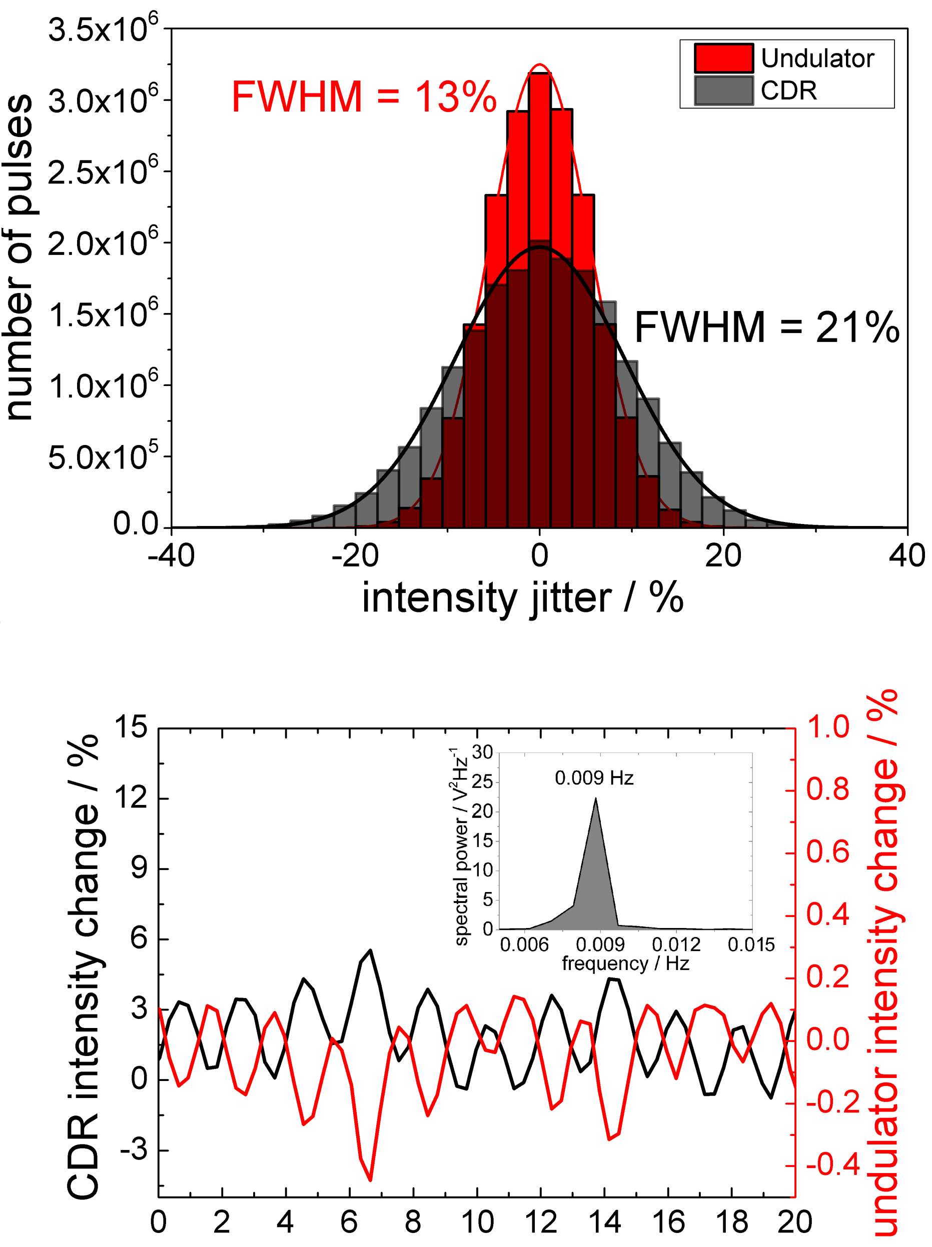

(a)

(b)

Figure 3.25: (a) Histogram of the intensity fluctuations between the CDR and undulator sources over 60 seconds, relative to the mean. It is thought that the greater variation on the CDR pulse intensity is probably due to beam movement causing part of the electron bunch to impinge on the CDR screen, causing additional intensity from residual transition radiation. (b) A plot showing the changes in intensity for both TELBE sources over a time frame of 20 minutes. This illustrates how the undulator dims when the CDR intensity spikes, showing the likely effects of the electron beam position moving and causing some electrons to hit the CDR screen and generate more intense CTR radiation. This reduces the bunch charge going into the undulator, which shows up as a much smaller, but nevertheless present, decrease in pulse intensity.

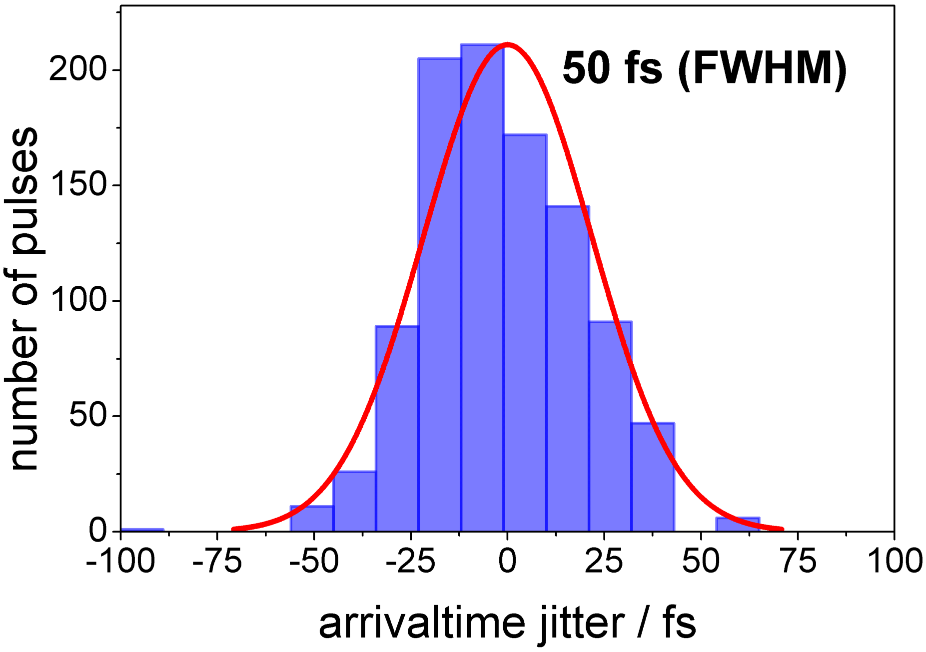

Figure 3.26: Distribution of timing jitter between the undulator and the DR source measured over 1 second. Note the observed comparatively large value of 50 fs (FWHM) is owed to the technological challenge of measuring the CDR and undulator THz pulses in parallel in one arrivaltime monitor. As discussed earlier, the real jitter is significantly smaller. Measurement taken with a beam energy of 24 MeV, bunch charge of 70 pC, and 300 GHz undulator tune. Taken from [6].

At the end of this section an attempt shall be made to identify characteristic frequencies in the different intensity and arrivaltime instabilities and discuss their potential origin. Since CDR and undulator intensity, as well as the arrivaltime of the CDR pulses, are measured in parallel the hope is that selective appearance of frequencies in the different intensity and arrivaltime monitors may indicate whether they originate from the accelerator itself, or from e.g. instabilities in the fs laser systems. Additionally, the determined CDR pulse arrivaltime jitter is compared to the measurements performed with the FLASH-type BAM positioned only roughly 1 m downstream of the CDR source. One interesting finding of this work is that the jitter frequencies observed with the BAM [54] only show up to a small degree in the arrivaltime of the actual THz pulses in the experiment. This makes clear that many of the observed characteristic frequencies may be due to instabilities in the detection (e.g. in the fs laser system) and may not originate from the accelerator. All observed characteristic frequencies are listed together in a survey table in the Appendix (see table B.2). The observed frequencies range from the sub-Hz range up to 48 kHz. The highest measurable frequency would be given by the Nyquist Frequency [68], which for a 100 kHz sampling rate is 50 kHz. It should furthermore be noted that frequencies above 50 kHz can show up as aliased frequencies of lower value (for instance, using a 100 kHz sampling rate, an 80 kHz component could show up as a peak at 20 kHz). Instabilities that do not show a perfectly sinusoidal behavior furthermore can produce higher harmonics in the observed frequency components (e.g. many higher harmonics of the line frequency of 50 Hz are observed which, at least partially, may result from this effect). In the following the different frequencies are discussed and ordered in different tables according to their appearance in the different intensity and arrivaltime monitors. Note that apart from 50 Hz, higher harmonics of the line frequency are not listed.

Table 3.1 lists all frequencies which show up in the intensity fluctuations of both superradiant THz sources and at least one of the two independent arrivaltime monitors, as these have the largest likelihood of originating in the accelerator. These frequencies are all in the low frequency regime (less than 1500 Hz) and predominantly consist of multiples of the line frequency of 50 Hz. There are, however, three frequencies at 132, 166, and 527 Hz that are clearly not higher harmonics of the line frequency. Table 3.2 lists frequencies which show up only in the intensity of both of the THz sources, but not in the arrivaltime. Three distinct frequencies are observed at 0.009, 160, and 193 Hz, all of which show the phase shift of pi (180 degrees) between undulator and CDR, which indicates that they are caused by electron beam position instabilities. Table 3.3 lists the frequency components that are only present in the intensity instabilities of only one of the two sources and are not present in any arrivaltime measurement. Here it is not clear whether this stems from the fact that the influence of a particular instability

Freq. (Hz)	50	132	166	527
CDR intensity	+++	+++	++	+
Undulator intensity	++	++	++	
CDR arrivaltime	++	+	+	
BAM	++			+++

Table 3.1: Frequency components visible in intensity fluctuations and in at least one arrivaltime measurement. These frequencies arise from instabilities in the accelerator that affect both intensity and arrivaltime (e.g. beam energy). Since they show up in multiple independent monitors their origin in the undulator is certain. Note that line frequency multiples are not shown. +:weak ++:medium +++:strong

on the intensity of one source is significantly lower or if the instability originates somewhere unique to either one of the sources. As shown earlier, instabilities in the beam position show up much more strongly in the CDR intensity than in the undulator intensity. This may lead to the fact that the faint influence on the undulator intensity is not observed for the majority of the frequencies given in Table 3.3. This may explain the exclusive appearance of, in total, 12 frequencies between 68 Hz and 48 kHz in only the CDR intensity. In contrast, only three frequencies, apart from the line frequencies and higher harmonics, show up exclusively in the undulator intensity (8089 Hz, 36.265 kHz, and 36.365 kHz). Therefore one may attribute these three frequencies to instabilities in the undulator power supply with some confidence.

It is interesting to note that only two frequencies show up exclusively in both independent arrivaltime measurements, at 12.8 and 22.7 kHz (see table 3.4). See table B.1 in the Appendix for a list of frequencies that only show up in one arrivaltime measurement. The fact that these two frequencies show up in both monitors leads to the conclusion that they very likely originate from an accelerator instability that does not, or at least only very little, affect the THz intensities. To summarize, the analysis of the selective appearance in the different monitors allows for suggesting some assignments of different frequencies to particular instabilities in the accelerator, the fs-laser system, and the undulator power supply.

Freq. (Hz)	0.009	160	193
CDR intensity	+++	++	+
Undulator intensity	+++	+	+

Table 3.2: Frequency components only visible in intensity fluctuations in both THz sources. Since they show up in the intensity of two different sources measured with two independent monitors their origin in the accelerator is certain. All components shown here are out of phase by a factor of pi. As discussed in the text, this behavior indicates that they originate from beam position movements. Note that line frequency multiples are not shown. +:weak ++:medium +++:strong

Freq. (Hz)	68	3634	8089	8273	11908	14312	16520	29295	31085	36265	36365	36734	42993	46628	48250
CDR intensity	+	+		+	++	+	+	+	+			+	+	++	+
Undulator intensity			+							+	+				

Table 3.3: Frequency components only visible in intensity of one THz source (CDR or undulator) that do not show up in arrivaltime. The intensity measurement of both sources is performed in parallel by direct detection with two pyrodetectors of the same type [40]. The origin in the accelerator is therefore relatively certain, as they only show up in one of the two sources. Because they show up in only one of the two sources an origin specific to the actual THz source itself is also a logical possibility. Note that line frequency multiples are not shown. +:weak ++:medium +++:strong

Freq. (Hz)	12732	22869
CDR arrivaltime	+	++
BAM	+	++

Table 3.4: Frequency components seen in both arrivaltime measurements, but not in the intensity instabilities. Because they show up in two independent arrivaltime monitors, the involved fs laser systems can be excluded, and these frequencies must originate in the accelerator. Since they do not show up in the intensity instability, some causes (e.g. beam position instabilities) can be excluded. Note that line frequency and multiples are also seen here but are not shown. +:weak ++:medium +++:strong

3.3 THz pump-fs laser probe experiments

One main motivation in establishing the TELBE THz facility is performing ultrafast pump-probe experiments. In this type of experiment the electric or magnetic field in the THz pump pulse acts as excitation of dynamics in matter. This dynamic in turn is then probed stroboscopically by ultra-short (light) pulses, typically with the sub THz cycle resolution. This class of pump-probe experiments [3] is only a very recent extension of techniques in ultrafast science, because CEP-stable THz pulses of sufficient strength have only been available for less than 15 years. Tabletop laser-driven THz sources exist, but are limited in repetition rate to the few kHz regime. Furthermore, they cannot provide multi-cycle/narrow-band THz pulses with high fields in the low THz frequency regime. Although TELBE is not yet operating at its design parameters it already provides a unique combination of high pulse energy, high field, and high repetition rate (see Figure 2.1 b). Thereby experiments that require better dynamic range than available at lower repetition rates will benefit. Moreover there are a number of ultrafast probe techniques, such as TR-ARPES [69] or TR-SNIM [70], that can only be usefully employed at repetition rates higher than a few 10 kHz. While techniques like TR-ARPES and TR-SNIM are sophisticated and are currently designed and constructed in dedicated projects at the TELBE facility, two first benchmark experiments were performed as part of this work aiming to establish the performance of TELBE in state of the art THz pump-laser probe experiments. Both experiments probe THz driven coherent spin excitation. The reason for this is threefold. Firstly, since the frequency range of TELBE with high pulse energies currently lies between 0.3 and 1.2 THz, only a limited number of low energy degrees of freedom can be addressed, one of which are spin excitations such as anti-ferromagnetic and ferromagnetic modes in anti-ferromagnetic or ferrimagnetic films. Secondly, coherent THz excitation of spinwaves is one of only a few examples where the origin of THz driven processes is undisputed. Finally, prototype magnetic materials exist where the required magnetic order is present at room temperature so that this type of experiment did not require sophisticated cryogenic sample conditions.

3.3.1 Coherent THz control of spinwaves probed by transient Faraday rotation

Faraday rotation is a method of measuring magnetization of a sample by recording the change in polarization of a probe laser beam measured after transmission through the sample. As established by T. Kampfrath et al [3] in a seminal tabletop laser-based experiment, the transient magnetic field of sufficiently strong single-cycle THz pulses can interact with the spin degree of freedom via the Zeeman torque (see Figure 3.27 a). This sets off a coherent spinwave which, given the THz field is strong enough, can be probed by the transient Faraday effect via the polarization rotation of NIR laser probes. The pulse energy in the original experiment [3] was 1 μJ, equivalent to the pulse energy of the undulator pulses tuned to the resonance frequency of 1 THz. Because the spectral bandwidth of the undulator pulses from TELBE is much narrower, the actual spectral density in the resonance, in this case the antiferromagnet NiO, is more than one order of magnitude higher. This in turn results in a dramatically larger amplitude of the spin deflection angle in comparison to the tabletop experiment (see Figure 3.27 b).

In the experiment, the coherent spin excitation of a 50 μm thick NiO film was probed. The actual data quality is exceptional as can be seen in Figure 3.28 a, where the spectrum of the experimentally determined Faraday signal is shown on a logarithmic scale. The excellent dynamic range of up to 20000, or 43 dB, in the frequency domain can be utilized to extend the technique of the THz pump-Faraday probe to nanofilms. One example is shown in Figure 3.28 b where a measurement of the coherently excited ferromagnetic mode in a 46 nm Mn_3Ga film is shown, which results in a moderate dynamic range of 8 dB [71]. Presently TELBE is the only place in the world where this type of measurement can be performed on magnetic nanofilms. Finally, the pulse resolved data acquisition, along with the high repetition rate, opens up possibilities for measuring important dependencies of the THz driven processes very efficiently in parallel. One example is shown in Figure 3.28, where the atypically large fluctuations of the intensity in the TELBE undulator source during the THz excitation measurement of NiO was utilized to determine the important fluence dependence of the THz excitation (see Figure 3.29). Intensity data was recorded for each pulse, and by separating the data into groups by THz intensity, multiple plots were created each with a different pump intensity. The peak spectral power was then calculated for each plot.

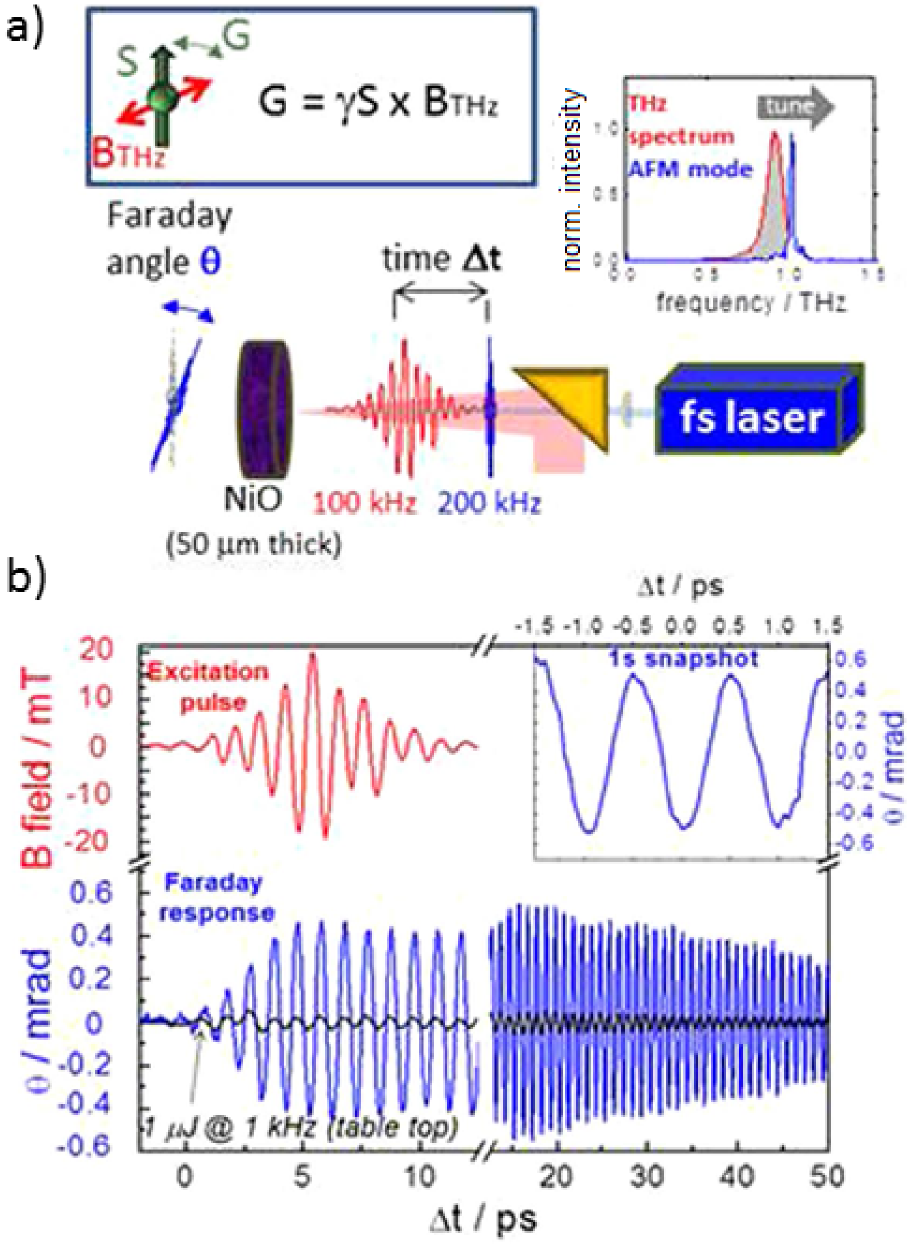

Figure 3.27: a) Experimental scheme for transient Faraday measurements on THz driven spin precession. The TELBE undulator source, even at the preliminary parameters, exceeds the spectral density of table-top THz sources by a factor of 36. b) Benchmark experiment performed at TELBE on a 50 micron thick NiO sample. The Faraday signal from the tabletop THz excitation (black) is much smaller than that after excitation with the narrow-band, multi-cycle THz pulses from the TELBE undulator. Note that the actual pulse energy was 1 μJ equivalent in both experiments and the higher amplitude is a result of the considerably larger spectral density. (top right) 1 s snapshot utilizing data from 10^5 THz pulses . In this case the delay between THz excitation and laser results purely from the arrivaltime jitter. Taken from [6].

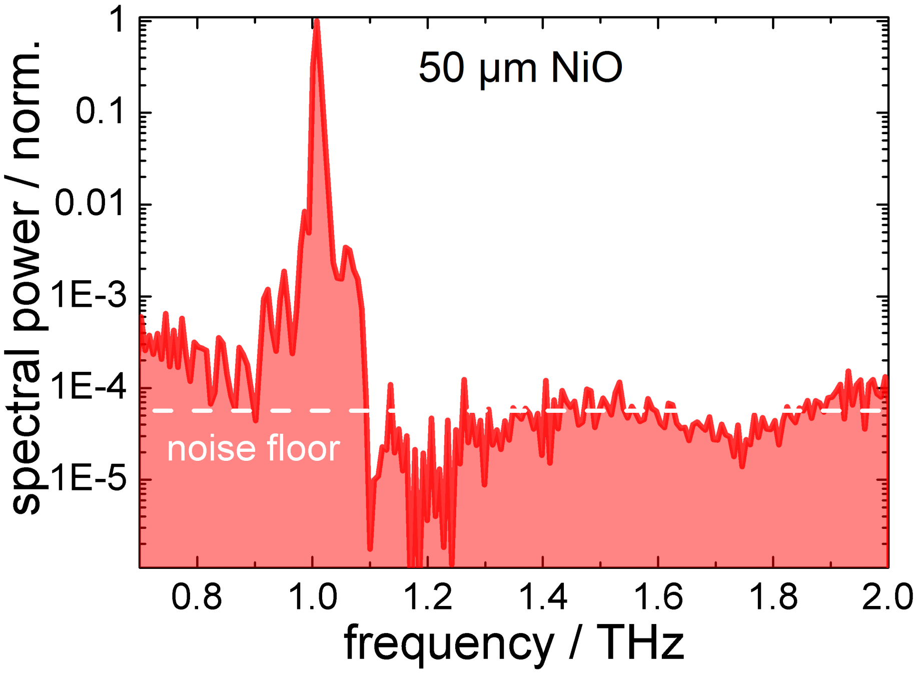

(a)

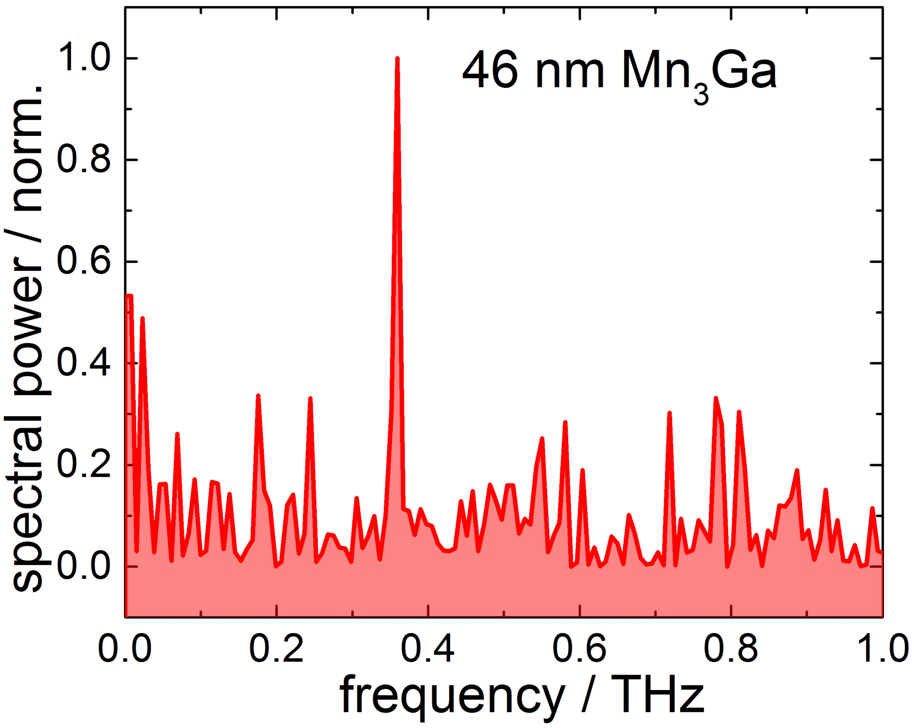

(b)

Figure 3.28: (a) Fourier transform of the transient Faraday rotation in a 50 μm thick NiO sample excited by THz pulses from the undulator tuned to the AFM resonance. An excellent dynamic range of better than 20000, or 43 dB, is observed. Adapted from [7]. (b) Fourier transform of the transient Faraday rotation in a 46 nm thin film Mn_3Ga sample excited by THz pulses from the undulator tuned to the FM resonance at 0.36 THz. Dynamic range of 7, or 8 dB, is shown. Adapted from [71]. Both measurements used a 24 MeV beam with 70 pC bunch charge and a repetition rate of 100 kHz.

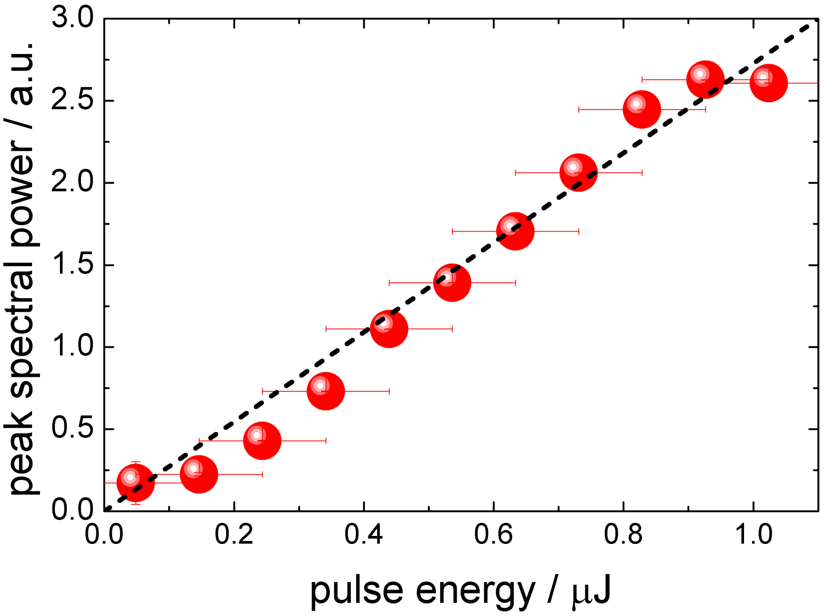

Figure 3.29: Plot of the fluence dependence of the THz driven spinwave excitation of a 50 μm thick NiO film. The THz pulse energy was recorded for every pulse by the pulse-to-pulse data acquisition system. Subsequent analysis allows assignment of different pulse energies to the observed peak spectral power of the THz driven spin deflection. In this particular beamtime the pulse energy varied between ~0 and 1 μJ, which allowed the determination of the fluence dependence over the full range from almost 0 to the maximum pulse energy. The expected linear dependence of the peak spectral power on the pulse energy of the THz excitation pulse was observed. Beam energy was 24 MeV and the bunch charge was 70 pC. Taken from [7].

3.3.2 Coherent THz control of spinwaves probed by THz emission spectroscopy

The second benchmark experiment is also probing THz driven coherent spin precession, but by use of so-called THz emission spectroscopy. In this case the spin deflection is probed via the emitted coherent THz waveforms. As was recently observed [72] [71], the coherent precession of magnetization leads to the emission of THz pulses with the frequency and damping of the precession. This technique has several advantages over probing THz driven coherent spin excitation via the Faraday effect: (i) in-plane precession can also be probed and (ii) the magnetic materials are not exposed to NIR fs laser pulses. The latter point means that in a THz pump-THz emission probe experiment at TELBE the magnetic resonance is exclusively excited. The observed frequencies and damping coefficients are therefore not affected by excitation of hot electrons as can be the case for fs laser probing via transient Faraday rotation. The principle of the measurement is shown in Figure 3.30 a. The narrow-band THz pulses from the undulator source are used to excite the coherent spinwave. The coherent spin precession leads to the emission of a coherent THz waveform with the resonance frequency of the spinwave. This emission is refocused by two off-axis parabolic mirrors and detected in the time domain by electro-optic sampling. The emitted THz waveform can be separated from the THz excitation pulse by utilizing the fact that the phase of the emitted THz pulse can be shifted by 180° by means of a small external magnetic field. The measurement, which in this case was performed on a 200 μm thin film of another prototypical antiferromagnet, $YFeO_3$, is shown in Figure 3.30 b with the resulting spectrum shown in Figure 3.30 c. As can be seen, THz emission with an exceptional dynamic range of 200000, or 55 dB, in the frequency domain can be achieved.

As in the case of THz pump-NIR laser based Faraday probe experiment, THz emission spectroscopy of the type described above benefits tremendously from the unique combination of intense, tunable narrow-band THz pulses and the high repetition rate available at TELBE.

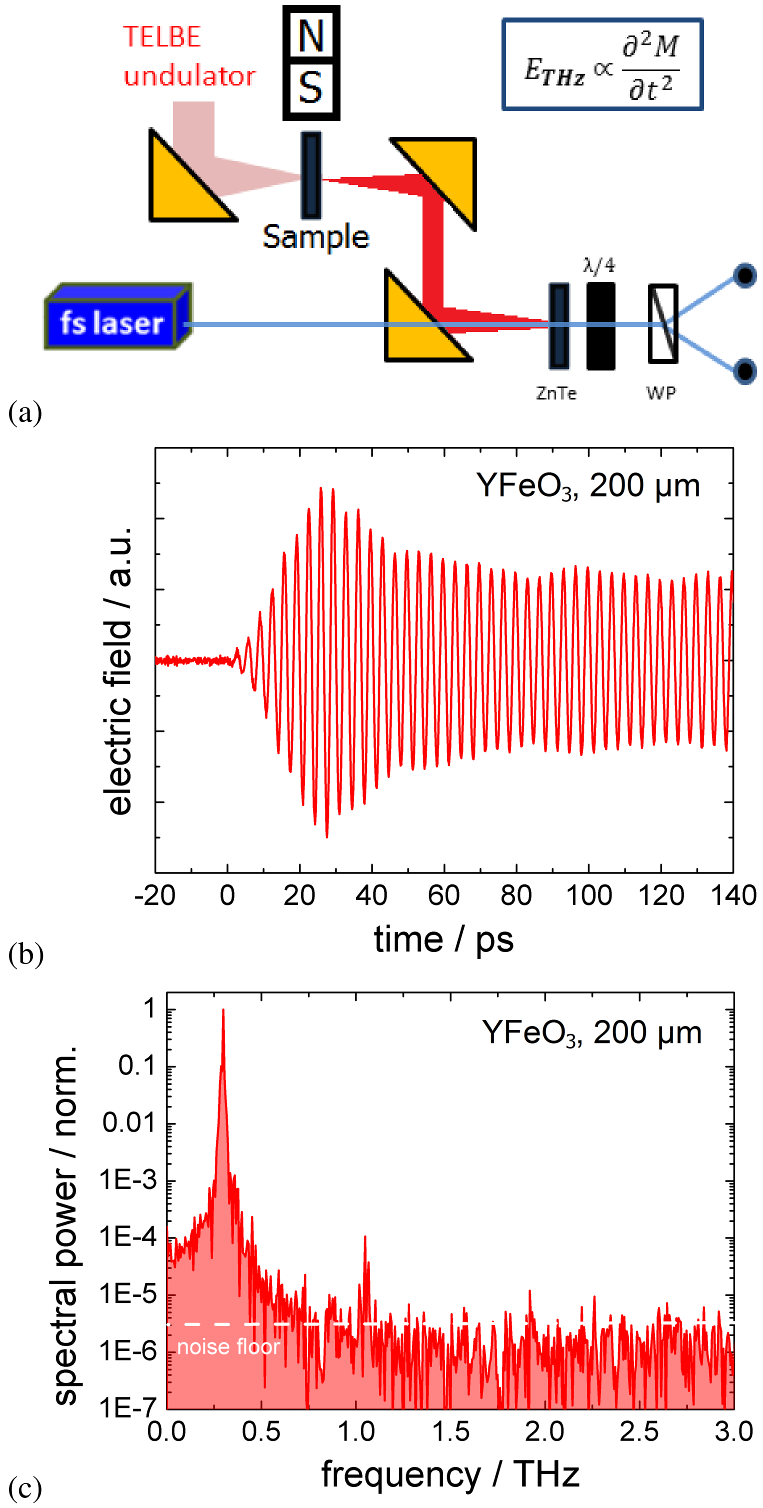

Figure 3.30: (a) Recently established scheme at TELBE for THz emission spectroscopy from THz driven spinwaves and (b) demonstration experiment detecting THz emission from the ferromagnetic-like mode in a 200 μm YFeO$_3$ driven by the THz undulator tuned to 0.3 THz center frequency. Note, the residual pump THz pulse has been removed from the data by adding 2 measurements with a reversed weak in-plane magnetic field of +/- 100 mT. (c) Fourier transform of (b), showing the strong peak at 300 GHz, which is the resonance frequency of the ferromagnetic-like mode in YFeO$_3$. The dynamic range of 200000, or 55 dB, can also be seen.

Chapter 4

Summary

4.1 Pulse-resolved data acquisition system

In this work, a pulse-to-pulse data acquisition system was developed for use at repetition rates of 100 kHz. For each pulse, several data channels can be taken. Currently an image file containing the arrival time information, the THz pulse intensity, and the actual experimental data (e.g. the signal from a balanced detector) are recorded (see Figure 3.7). This data can be used to improve the dynamic range and time resolution in time-resolved experiments. The developed system was characterized over the course of this work and an excellent performance could be established. A time resolution of 28 fs (FWHM) (see Figure 3.8) and a dynamic range of 120 dB (see Figure 3.11) was established in benchmark THz pump-probe experiments. A current drawback is the fact that online datasorting and the overall data handling only allow operation with roughly a 25% duty cycle. For every 1 second of data taken at 100 kHz, roughly 3 seconds are required to write the data to storage. This is because the hardware is not currently capable of doing the necessary processing at the required speed. As described in the outlook, a project has been started to achieve a 100% duty cycle by means of implementing FPGA architecture to achieve the necessary speed to process data between pulses, as well as improving the transfer rate of data to storage (see Figure 5.1).

4.2 Characterization of TELBE sources

Once the data acquisition system was developed, tested, and characterized it became possible to utilize it to characterize the THz sources available from TELBE. Because the work done in this thesis was primarily performed during the commissioning of TELBE, the accelerator was operating in diagnostic mode. This mode limited the beam current to below 10 μA, resulting in a repetition rate of 100 kHz with the desired bunch charge range of up to 100 pC. The multi-cycle superradiant undulator source has tunable central wavelength which can be varied between 0.1 and 3 THz (see Figures 3.16 and 3.17), with a bandwidth of 20%. The pulse energy varies based on the central frequency, with a peak of 1.3 μJ at 1 THz (see Figure 3.17 b). The drop in intensity towards higher THz frequencies is due to losses in the electron bunch formfactor (see Figure 2.6). The beam profile of the undulator was the expected bell shape.

The single-cycle superradiant THz source is a coherent diffraction radiation (CDR) source. This is a broadband source (0.1-2.5 THz) with a peak intensity at around 0.5 THz (with some dependence on the accelerator settings). The peak is caused by an intensity falloff towards lower frequencies caused by diffraction losses in the transport beampipe, and a falloff towards higher frequencies caused by a combination of the electron bunch formfactor and the 4 mm central aperture (see Figure 3.23). The maximum CDR pulse energy received in the TELBE laboratory is in the 100 nJ range. The expected beam profile consists of two lobes, and this was observed (see Figure 3.19).

Calculations were performed to model the expected THz parameters of the superradiant sources at TELBE, such as spectral content, beam profile, and intensity. After taking the diffraction losses and polarization effects from the Brewster angle windows into account, these calculations fit well with observations. Note that the actual beam dynamics in the ELBE accelerator still have not been fully established. Work on this is ongoing and is being undertaken by the beam dynamics experts, and has also been the focus of another PhD project[73]. In this thesis, the spontaneous source emissions characteristics have been established as well as scenarios for the required bunch length for reaching the THz design parameters. Assuming a Gaussian bunch form, a bunch length of 30 fs (FWHM) is required to achieve the initially prospected maximum intensity at 3 THz [74].

The development of the pulse-to-pulse data acquisition system also created a way to measure pulse-to-pulse instabilities in the accelerator. By taking a measurement of the arrivaltime and intensity of every pulse, the arrivaltime jitter and intensity instabilities were systematically characterized. The intensity instabilities were surprising, with the undulator being much more stable than the CDR source (13% intensity fluctuation for the undulator, versus 21% for the CDR source, as shown in Figure 3.25). This rather significant difference has been attributed to beam position changes within the accelerator that affect the CDR source more than the undulator source. Arrivaltime jitter was also characterized to the highest frequency possible, up to 50 kHz. It was only directly determined for the CDR source, with the understanding that the undulator was intrinsically synchronized due to the sharing of electron bunches. This intrinsic synchronization was measured to be 28 fs (FWHM) (see Figure 3.8). The typical arrivaltime jitter of the THz sources, then, was shown to be 1.38 ps (FWHM) over the course of 1 second (see Figure 3.5 a). On longer timescales the arrivaltime will drift over larger time ranges (Figure 5.1 in the outlook). One important finding from these measurements is that the majority of the timing instabilities originate from instabilities with frequencies below 300 Hz. Overall, 75% of the contribution to the jitter (roughly 1 ps (FWHM)) stem from this range (see Figure 3.5 b). It was also shown that there is little correlation between the BAM and the arrivaltime monitor in measured jitter frequency components [75], leading to the conclusion that many of the BAM frequencies arise from instabilities within its own fs laser system, rather than originating from the accelerator. The THz-based arrivaltime monitor developed within this thesis also suffers from this, but there are some frequencies that have been clearly shown to originate in the accelerator because they also show up in the intensity instabilities (see Table 3.1). Furthermore, there are two high frequency components that appear in both the BAM and THz pulse arrivaltime monitor at 12.7 and 22. 9 kHz. Complimentary measurements indicate that they may originate from instabilities in the thermionic injector [21].

4.3 THz pump-fs laser probe experiments

The TELBE facility, in combination with the pulse-resolved data acquisition system, has been successfully employed in two different benchmark THz pump-Faraday rotation probe and THz pump-THz emission probe experiments. Furthermore, THz time domain spectroscopy (TDS) of the THz pulses from TELBE has been performed. The latter THz spectroscopy technique was shown to exhibit an excellent dynamic range of 10^6, which has not previously been seen at accelerator-based THz sources. However, the most obvious application of a high-field source such as TELBE is not linear spectroscopy, but instead the interrogation of dynamics driven by high-field THz pulses. Due to the currently limited frequency range between 0.1 and 1 THz the scientifically most interesting processes to this end are coherently driven spin excitations. In the first benchmark experiments, the THz driven spin excitation in NiO [6] and in a Mn_3Ga nanofilm [71] were probed by transient Faraday rotation. The resulting dynamic range allows the extension of this technique to nanofilms for the first time. The second benchmark experiment investigated the achievable data quality in a more recently developed technique which is based on the detection of the weak THz emission from the coherently driven spin excitation. The benchmark experiment, performed on $YFeO_3$, showed that an exceptional data quality can be achieved (dynamic range of 55 dB, see Figure 3.30). Both experimental classes have since become the focus of the majority of the experimental proposals for user experiments at the TELBE facility.

Chapter 5

Outlook

5.1 Improvement of THz pulse parameters

Although the actual beam dynamics, bunch compression strategies, and the development of the SRF injector were not part of this thesis, but were the responsibility of the respective experts at HZDR, some outlook should still be given here. The current pulse properties of the THz sources have not yet met the design goals put forth before the construction of TELBE (see Figure 2.1). There are several improvements planned to bring the pulse up to specifications. Currently, the ELBE accelerator produces bunches with a minimum bunch length of around 1 ps (FWHM). This yields maximum pulse energies of 1 μJ only up to frequencies 1 THz. Assuming a purely Gaussian bunchform, to obtain the originally intended optimal pulse energy also up to 3 THz [74], a bunch length of less than 30 fs (FWHM) is required (see Figure 2.6 b). One result of this work is that new beam dynamics simulations are being performed by experts at HZDR to reestablish the feasibility of their earlier handwaving prediction. Another problem is the still not fully operational SRF injector [76] which so far inhibits the high charge regime, and the prospected increase of the optimal pulse energy up to the 100 μJ regime could not yet be shown. A first beamtime utilizing the SRF injector was performed recently, however only at low charge and so far only moderate bunch compression was achieved. The hope is to operate TELBE with the high bunch charge mode of operation during 2017.

5.2 Arrivaltime sorting at sub-1 fs resolution

The current arrivaltime monitor that was developed in this thesis as part of the pulse-to-pulse data acquisition system has an optimal timing resolution of 12 fs (FWHM), as determined by the physical properties of its the design. In the following it shall be discussed if and how a sub-fs time resolution can be achieved. At the moment the time resolution is limited by three main contributions: the 8 ps (FWHM) wide time window, the 1.59 nm/mm linear dispersion of the spectrometer, and the 10 μm pixel size of the camera [7].

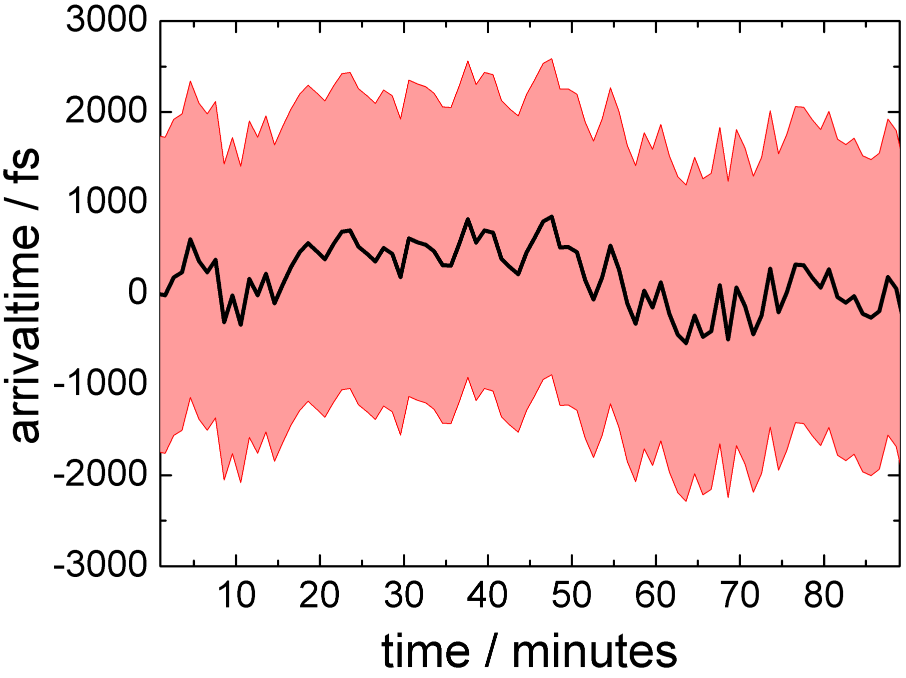

Figure 5.1: Illustration of the typical drift of the THz pulse arrivaltime over a 90 minute interval. The instability of the arrivaltime on such timescales, which correspond to a typical time for 1 minute in a THz pump-probe experiment is here 3.44 ps (FWHM). Note that this value is FWHM, hence approximately 0.5% (around 27000) of the pulses will arrive outside of this time window. Sometimes also large drifts beyond 5 ps (FWHM) have been seen, hence a time window of ~8 ps (FWHM) is used in the arrivaltime monitor to make sure the arrivaltime of most pulses if captured. The black line is the average arrivaltime over 1 minute, and the red area denotes the total arrivaltime jitter during that minute.

The 8 ps (FWHM) wide time window is a limit on the arrivaltime resolution of the monitor because it means the spectral decoding probe pulse must be stretched to this length to ensure that the THz pulses are always in this time window, despite the considerable few ps (FWHM) drift and jitter observed on longer time scales (see Figure 5.1). By stabilizing the timing jitter and drift to below 1 ps (FWHM), it would be possible to reduce the size of the time window. This would in turn increase the timing resolution of the monitor as a whole by a factor of 8, resulting in an absolute precision of 1.5 fs. Stabilization of SRF accelerators by active feedback has recently been shown down to even sub-100 fs (FWHM) [13], so achieving 1 ps (FWHM) stability at ELBE is feasible.

The linear dispersion of the spectrometer affects how large a slice of time each pixel of the readout camera sees. This means that if one were to replace the currently used Princeton Instruments SP2500 spectrometer with a Princeton Instruments SP7500 [77], which has a linear dispersion of 1.03 nm/mm, you would decrease the size of the time window that one pixel occupies. This has the effect of stretching the current time window over more pixels. In the current setup, that would change the time per pixel from 12 fs to 8.3 fs. Combined with the earlier discussed reduction of the time window, this would result in an absolute time resolution of 1.0 fs.

The pixel size of the camera limits the resolution much the same way the linear dispersion does. It creates a limit on how small a time slice each pixel can see. In the current setup the camera has a 10 μm pixel width [78]. There are currently commercial cameras available with up to 100 kHz repetition rate and a pixel size of 7 μm. Utilizing this type of camera would change the resolution from 12 fs to 8.4 fs. Combining this improvement with the others mention above would result in an absolute time resolution of 0.72 fs.

Improving the time resolution of the arrivaltime monitor is only one part of the necessary steps to achieve an overall resolution below 1 fs for the final data. The timing jitter between the CDR and undulator, for example, is in the range of 10 fs. In order to eliminate this it would be necessary to use the THz source acting as the experimental pump in the arrivaltime monitor itself. There are difficulties associated with this when the undulator is the source because of the long pulse length and multi-cycle nature, but solutions have been discussed and could be put into action in the medium term. At the few-fs timescale, smaller effects like acoustic vibrations in mirrors and thermal expansion effects on the laser path length become significant, so they also must be addressed e.g. by implementing active feedback in the laser path. Once that is achieved, however, sub-1 fs timing is clearly feasible at TELBE.

5.3 Online data-sorting at full duty cycle

There are challenges yet to be addressed regarding the arrivaltime system. The currently implemented prototype system has a duty cycle of about 25%. This means that if TELBE is operating at 101 kHz quasi-cw, the system can take data on every pulse for 1-2 seconds before it must stop to write the data to storage. The goal is to further develop the system to make it capable of taking data while writing to storage at the same time, allowing a 100% duty cycle at 101 kHz. This will of course also increase the rate that data is generated, so another challenge that must be addressed is increasing the availability of storage and the speed that data is transferred to this storage. Table 5.1 shows a table of data bandwidths required for various configurations of the arrivaltime monitor. Finally, after the data is taken it must be processed into a time-resolved image of the experiment. This can take several hours using current methods and depending on the size of the data set that was recorded. The next development at TELBE will be to increase the duty cycle of the acquisition to 100% and implementing some online processing, which requires several developments in both hardware and software.

Repetition rate	Camera	ADC 14 bits 8 channels	Data rate	Storage needed for 30 shifts of 12 hours each
101 kHz	Commercial	10 MS/s	505 MB/s	654 TB
101 kHz*	Commercial	10 MS/s	143 MB/s	185 TB
4.5 MHz	KALYPSO	5 GS/s	10.3 GB/s	13.3 PB
4.5 MHz*	KALYPSO	5 GS/s	6.3 GB/s	8.2 PB
13 MHz	TBD	15 GS/s	29.8 GB/s	38.6 PB
13 MHz*	TBD	15 GS/s	18.2 GB/s	23.6 PB
DALI 2025				
10x100 kHz	Commercial?	10 MS/s 14 bits	5 GB/s	6.54 PB
10x100 kHz	Commercial?	100 MS/s 16 bits	19.7 GB/s	25.6 PB

Table 5.1: Table of current and future data usage for TELBE data acquisition system. *Preprocessed, which means calculating the arrivaltime of the pulse online and only saving that data instead of the entire image of the pulse used by the arrivaltime monitor. Commercial camera currently in use is a Basler Sprint SPL4096 line scan camera, capable of repetition rates up to 140 kHz when using 2048 pixels. Data rate is the number required to calculate the required bandwidth of the network connection as well as the write speed of the storage system in order to take data continuously. KALYPSO refers to a fast line array currently under development [79].

5.3.1 Hardware

On the hardware side the current camera in use will still be adequate, but the computer hardware is not. A new system must be built that is capable of pulling the arrivaltime monitor data from the camera, processing it to get an arrival time (this process currently happens offline), and then saving this data to long term storage in between pulses. At the same time, data from the experiment must also be pulled from the analog-to-digital converter (ADC) and saved concurrent with the arrivaltime data in such a way as to make sure these two data sets are associated correctly with each other. Analysis of the data taken from the ADC is still planned on being processed afterward, so that several methods can be attempted to make sure the best quality signal is extracted from the raw data. The hardware needed to record, process, and export these two data sets in less than 10 μs (which is the time between pulses) means going to a system in which each data point is addressed as it comes in, instead of simply being recorded. A switch to an architecture based on a field-programmable gate array (FPGA) is planned, as this type of system should be fast enough to perform these fairly basic calculations and then output the data in the time required.

5.3.2 Software

Moving to a new architecture requires rewriting the whole data acquisition system, although the planned changes in performance would require this even if the hardware were to remain the same. It is changing from a burst-acquire, post processing system to a real-time acquisition and processing system. Some of the work currently done offline, in which the raw data is processed to extract the arrival time and experimental signal, is being done instead at the time of acquisition, before the data is saved. This greatly reduces the needed network bandwidth for moving the data to storage, but also reduces the tremendous amount of storage needed for even a few hours of measurements. Table 5.1 gives a table of the bandwidth required to save the data taken in various combinations of hardware while maintaining a duty cycle of 100%, as well as the permanent storage needed to store 30 shifts worth of data (15 days of continuous acquisition).

Appendix A

Software

A.1 Data acquisition software

The data acquisition software was written in LabVIEW to control hardware primarily manufactured by National Instruments, but is flexible enough to be used with other hardware as well. The biggest challenge to taking data from the fast sources in use a TELBE is synchronization. Getting every piece of data correctly correlated is still a challenge and will be the target of some additional future development. The interface screen was designed to be relatively simple to operate while still providing a large variety of monitoring options to allow a user to keep track of the conditions of the experiment. For instance, the default view when not actively taking data shows an image of the CDR pulse as seen by the arrivaltime monitor. A user must make certain that the timing pulse doesn't drift out of the time window, or timing information will be lost. Figure A.1 gives an example of that a user would see if they chose the option to view an online sorted step from the experiment. This can be used as a quick diagnostic to determine if there is a readable signal at a given time.

When the acquisition is started the software first resets the ADC, then routes the timing signal from the timing input connection on the ADC through an internal signal route to the image capture card. Next, a veto signal is sent to the external pulse generator to pause the pulse output which is used as a trigger signal. Then the software allocates memory to store the images of the CDR pulses. There is currently enough memory in the system to store 2 seconds of arrivaltime data and 2 seconds of data from the ADC. Next, the image capture card is initialized and the image capture is begun. It is important to remember that at this point the trigger signal is paused. Once everything is running the veto signal going to the pulse generator is removed, and ideally the ADC and image capture card both receive the next trigger pulse at the same time. In practice the image capture card sometimes skips one trigger pulse, which requires correction later. Now the data acquisition has started and continues for 2 seconds. The image array fills with line arrays of pixel values, and a separate array fills with data from the ADC at the same time. When acquisition is complete the data is then moved to disk for storage A.2. Figure A.3 gives an example of the data taken by the image capture card. Each horizontal line is one CDR pulse. Figure A.4 shows 1 ms of the raw ADC data, before any processing is performed. Figure A.5 gives an example of three single experimental data points. Each of these plots represents one ADC data point, to be associated with one CDR image as represented by a single line in the arrivaltime image. This also illustrates the double-frequency probe pulse strategy, with the first pulse shown being the signal pulse, and the second pulse shown being the background pulse to be subtracted from the signal.

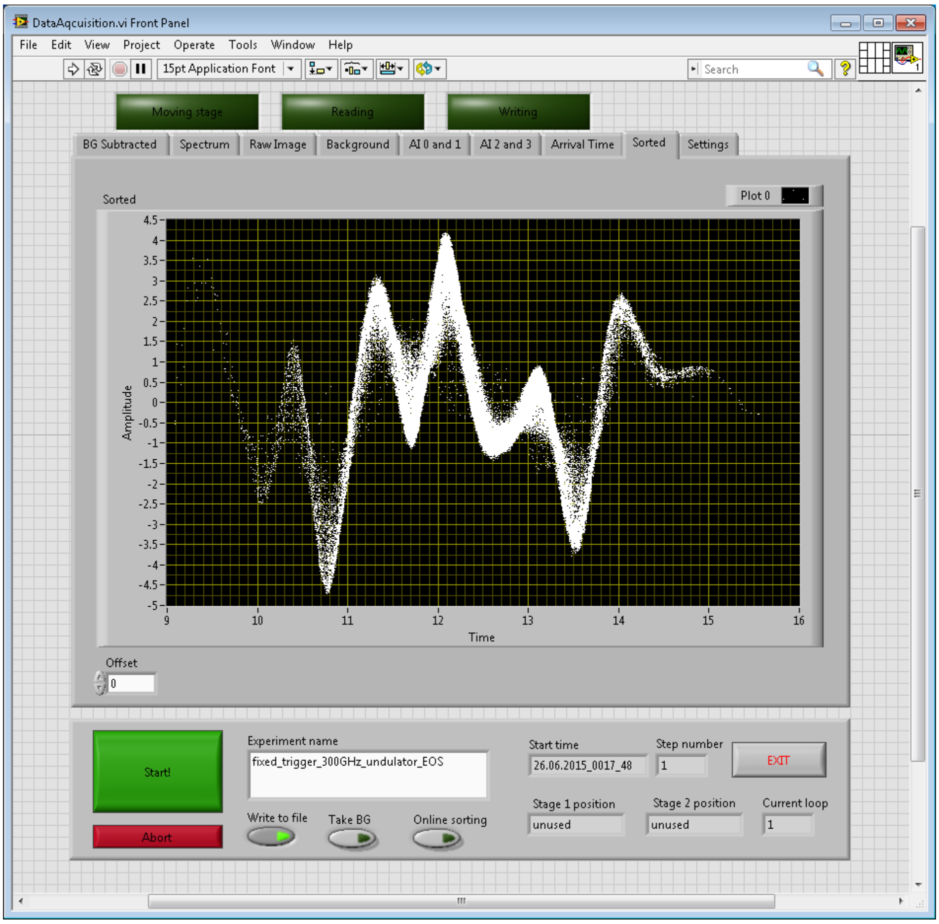

Offset: 0

Experiment name: fixed_trigger_300GHz_undulator_EOS

Start time: 26.06.2015_0017_48

Step number: 1

Stage 1 position: unused

Stage 2 position: unused

Current loop: 1

Figure A.1: Image showing one of the interface screens of the data acquisition software. This particular tab contains an online representation of the sorted data that is being currently acquired. Because this step requires a significant delay to process it is normally disabled.

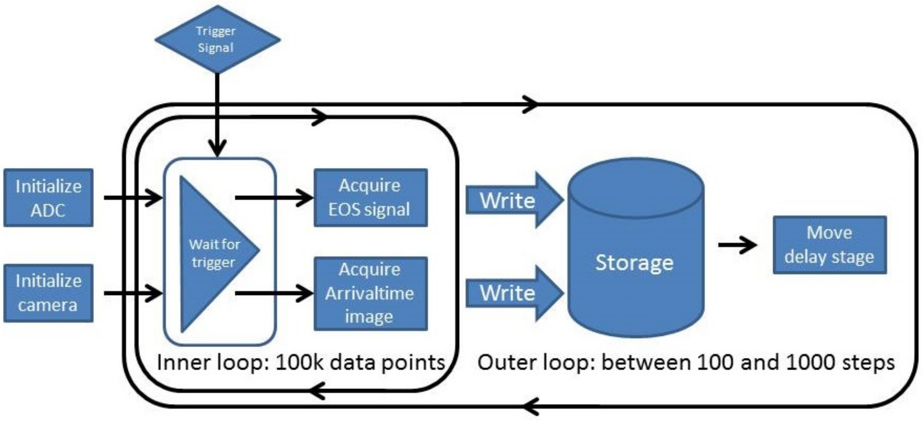

Figure A.2: Chart demonstrating the basics of the data acquisition system used to gather the data for our experiments. Initializing the hardware and synchronizing the data collection were the main tasks, and writing the data to disk in a usable format was the final step.

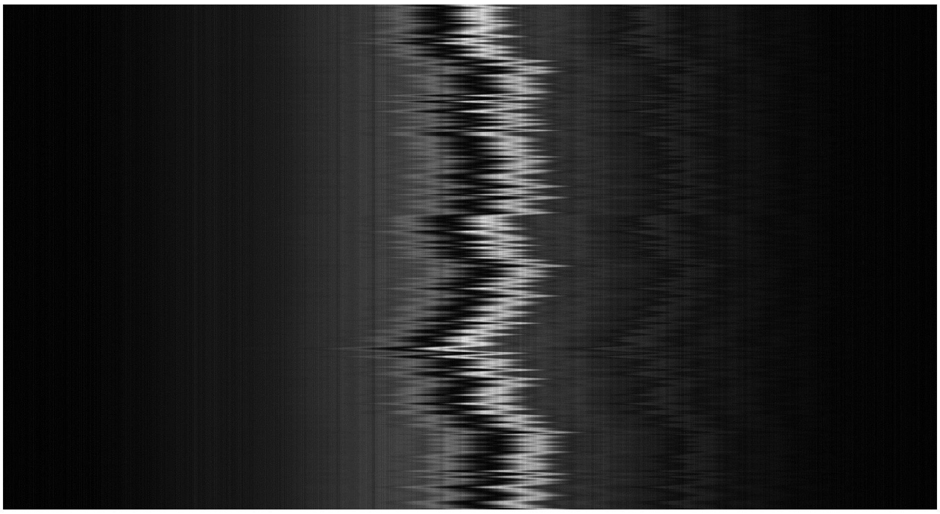

Figure A.3: Image showing an example of the raw arrivaltime data. The data is recorded as an uncompressed TIFF image.

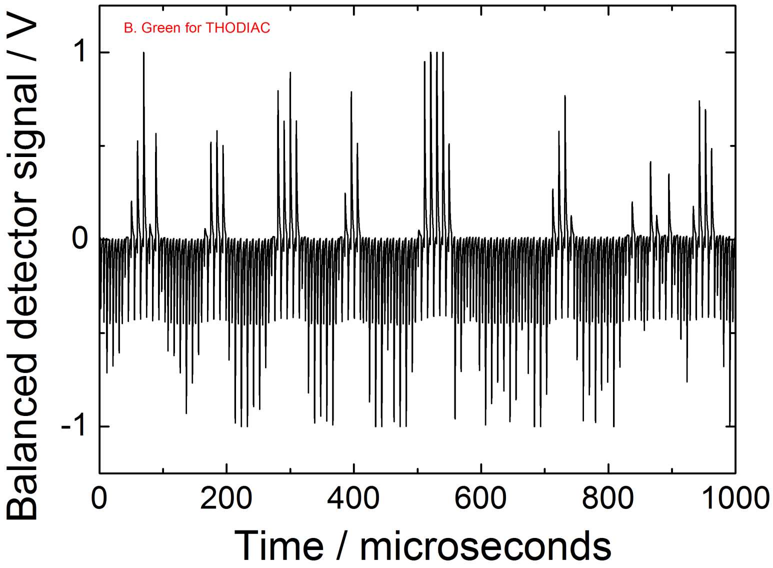

Figure A.4: Image showing an example of the raw balanced detector data. The data is recorded as a 16 bit binary array.

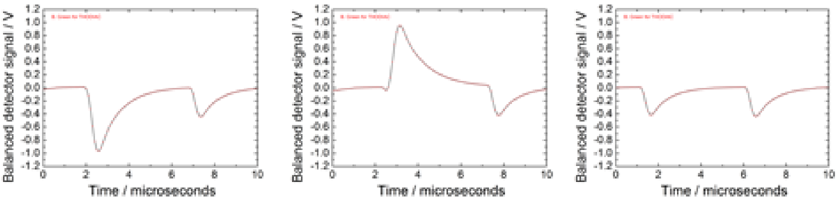

Figure A.5: Example of a balanced detector output with a negative signal (left), positive signal (center), and a zero signal (right). Using a sum or mean of the data points, along with subtracting the background signal (the pulse on the right side of each graph) allows the zero-signal balanced detector output to give a result of zero.

A.2 Data sorting program

The first step is to take the raw line image and convert it into a time value. This is done by first converting each line in the image to an array of integer values, then filtering each array to remove high-frequency noise which can interfere with peak finding. Then, a peak finding algorithm finds the pixel where the peak occurs. Using a previously measured calibration value, each pixel is assigned a time (for instance, if each pixel represents a 10 fs slice of time, so the fourth pixel would correspond to an arrival time of 40 fs) and this is the arrival time of this particular pulse.

Next, the pump-probe experiment output is processed. This data consists of an array of single-precision points taken at a rate of 10 MHz, so each point represents the voltage reading from the detector at 100 ns intervals. The first step is to calculate a signal strength based on this array of data points. The described system uses a sum of the points, but could also use a mean or some other measure, to obtain a single numeric value to represent signal strength. Simply using the highest data point value introduces high-frequency noise into the signal, as well as never returning a zero value due to imperfect balancing in the balanced detector, so this is generally to be avoided.

Once both an arrivaltime value and a signal value have been calculated from the raw data, they are matched up so that the arrivaltime measured comes from the same electron bunch that generated the pump pulse in the pump-probe experiment. The width of the signal window is defined by the THz-laser jitter. In the described setup it was limited to a ± 4 ps window, with most points falling toward the center of that range. A number of measurements can be taken sequentially, each time slightly moving the linear delay stage that is part of the probe laser beamline. The sequential measurements can be made to overlap by using small movements, increasing statistics for a better signal to noise ratio, as well as allowing processes hundreds of ps long to be measured with excellent temporal resolution. In this case the software will add a delay to all the points of each step which corresponds to the delay introduced by the movement of the delay stage.

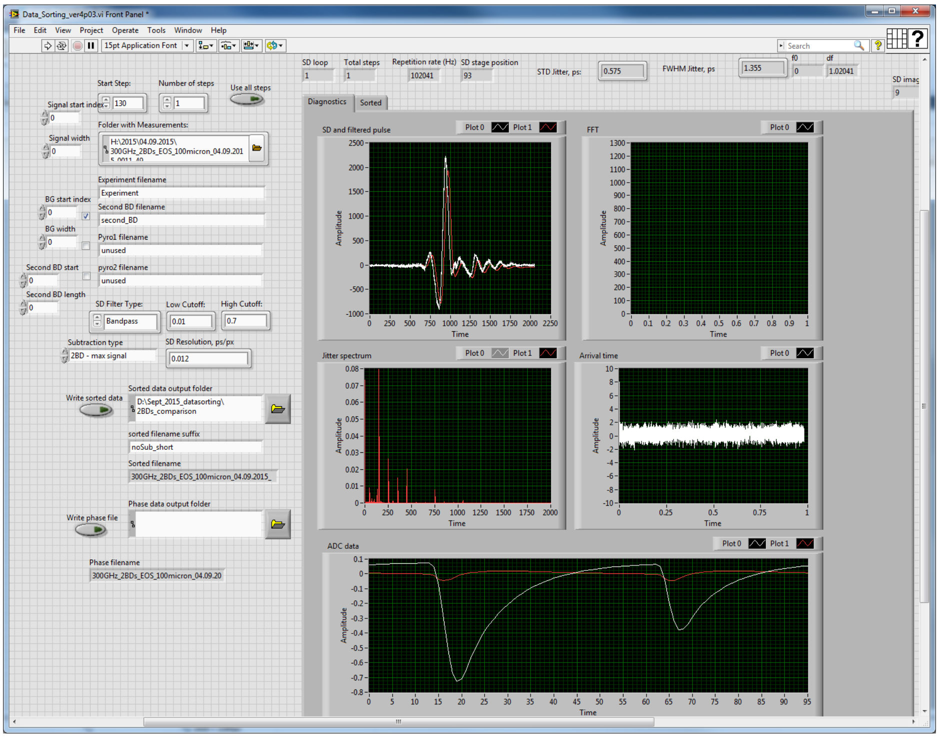
Data_Sorting_ver4p03.vi Front Panel *

Start Step: 130
Number of steps: 1
Signal start index: 0
Signal width: 0
Folder with Measurements: H:\2015\04.09.2015\300GHz_2BDs_EOS_100micron_04.09.201
Experiment filename: Experiment
BG start index: 0
Second BD filename: second_BD
BG width: 0
Pyro1 filename: unused
Second BD start: 0
pyro2 filename: unused
Second BD length: 0
SD Filter Type: Bandpass
Low Cutoff: 0.01
High Cutoff: 0.7
Subtraction type: 2BD - max signal
SD Resolution, ps/px: 0.012
Sorted data output folder: D:\Sept_2015_datasorting\2BDs_comparison
sorted filename suffix: noSub_short
Sorted filename: 300GHz_2BDs_EOS_100micron_04.09.2015_
Phase data output folder:
Phase filename: 300GHz_2BDs_EOS_100micron_04.09.20
SD loop: 1
Total steps: 1
Repetition rate (Hz): 102041
SD stage position: 93
STD Jitter, ps: 0.575
FWHM Jitter, ps: 1.355
f0: 0
df: 1.02041
SD imag: 9

Figure A.6: Image of the interface of the data sorting program. It shows various diagnostics that display how well the program is working and allow the user to control input variables that describe how the data was recorded in order to get the correct output.

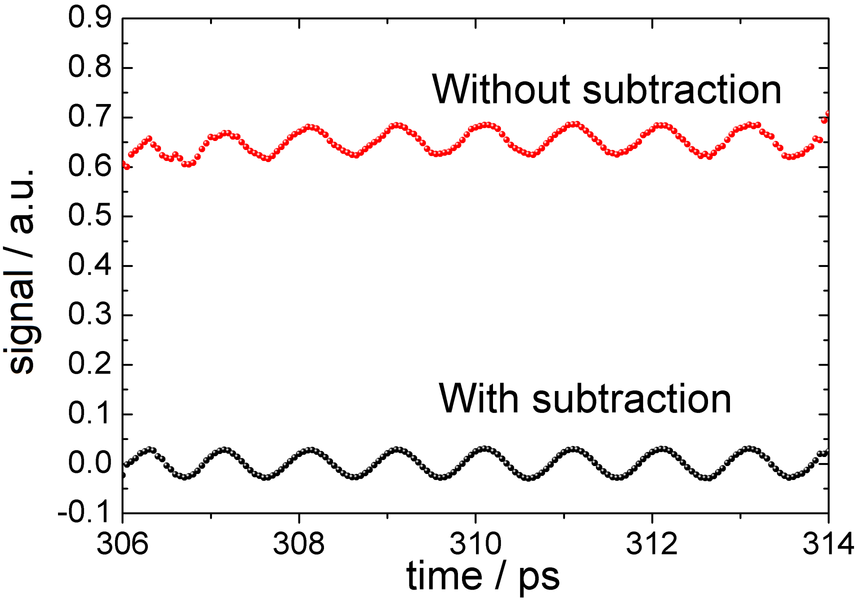

Figure A.7: Example of the 200 kHz laser noise subtraction technique. Red shows a MOKE measurement of a 1 THz oscillation of a 50 μm NiO film, taken with the probe laser operating at the same repetition rate as the THz. Black shows the same measurement, but using a probe beam operating at double the THz repetition rate and subtracting the second, unmodified pulse from the first one. This reduces noise originating in the laser intensity jitter. The effect is most clearly seen as subtraction of a DC value from the signal. There is also some small improvement in the noise visible with subtraction. Data taken with 101 kHz repetition rate, 24 MeV beam energy, and 70 pC bunch charge.

Appendix B

Additional figures

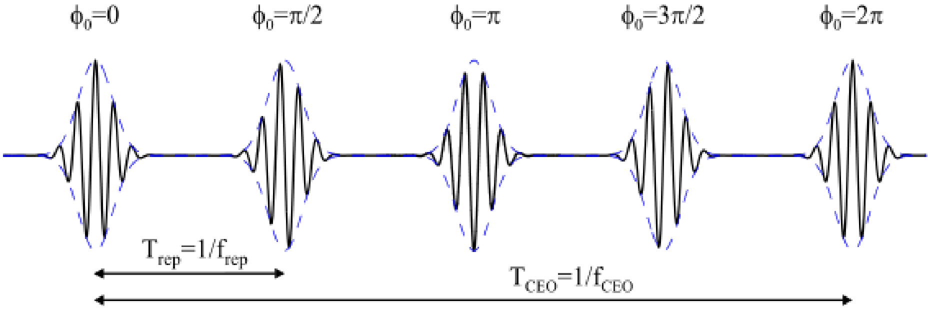

Figure B.1: Carrier envelope phase in the time domain: A pulse train of five consecutive pulses with linearly varying CEP is depicted. Depending on its value the relative delay between the carrier (black) and the envelope (blue dashed) is different. Taken from [80].

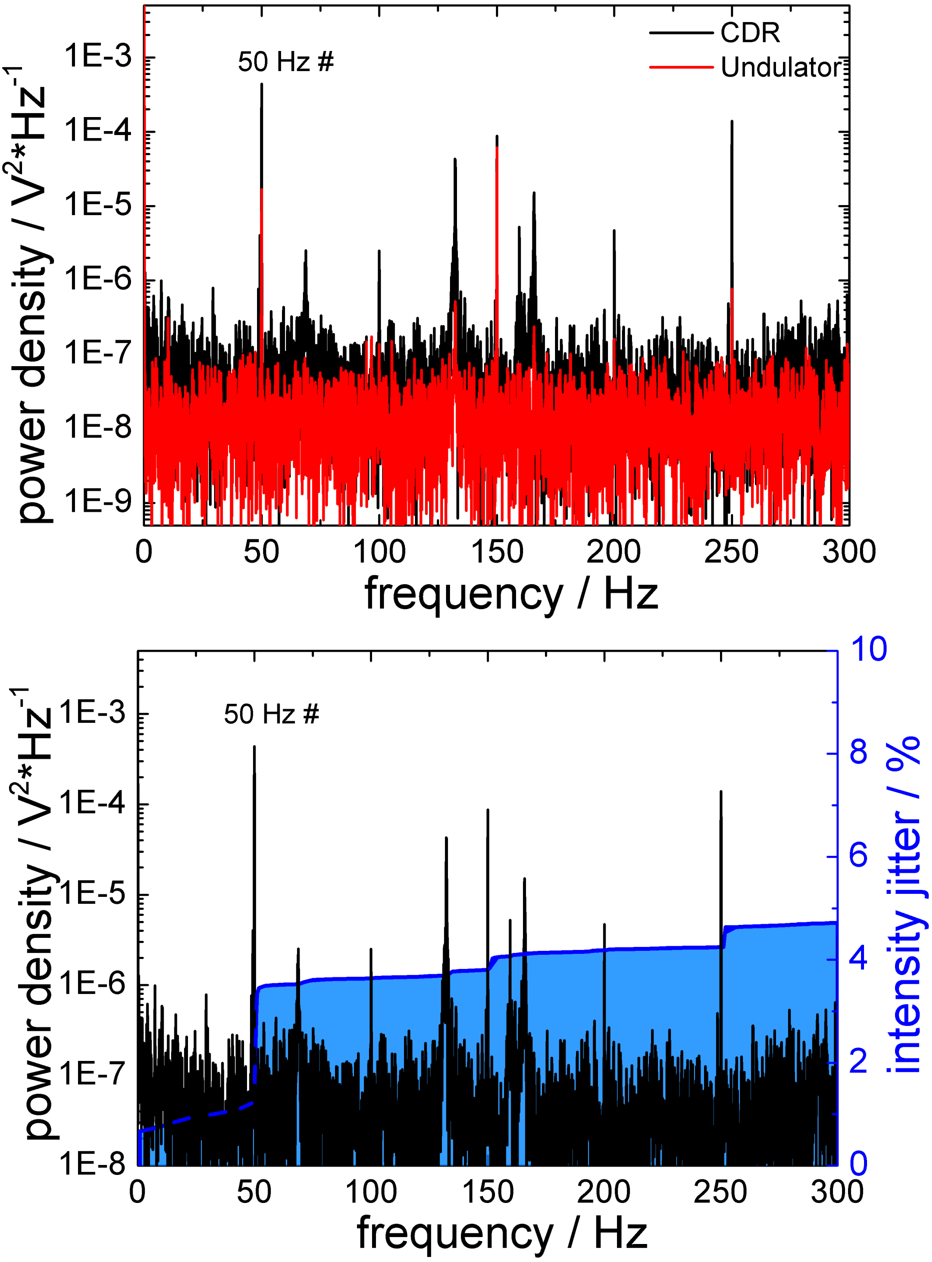

Figure B.2: Low-frequency portion of the spectrum of the intensity fluctuations of the CDR and undulator sources at TELBE. It can seen that a subset of frequencies are shared in between the CDR and undulator sources. The frequency of 50 Hz marked with a # is 180° out of phase between the two sources, and can be attributed to instabilities of the beam position.

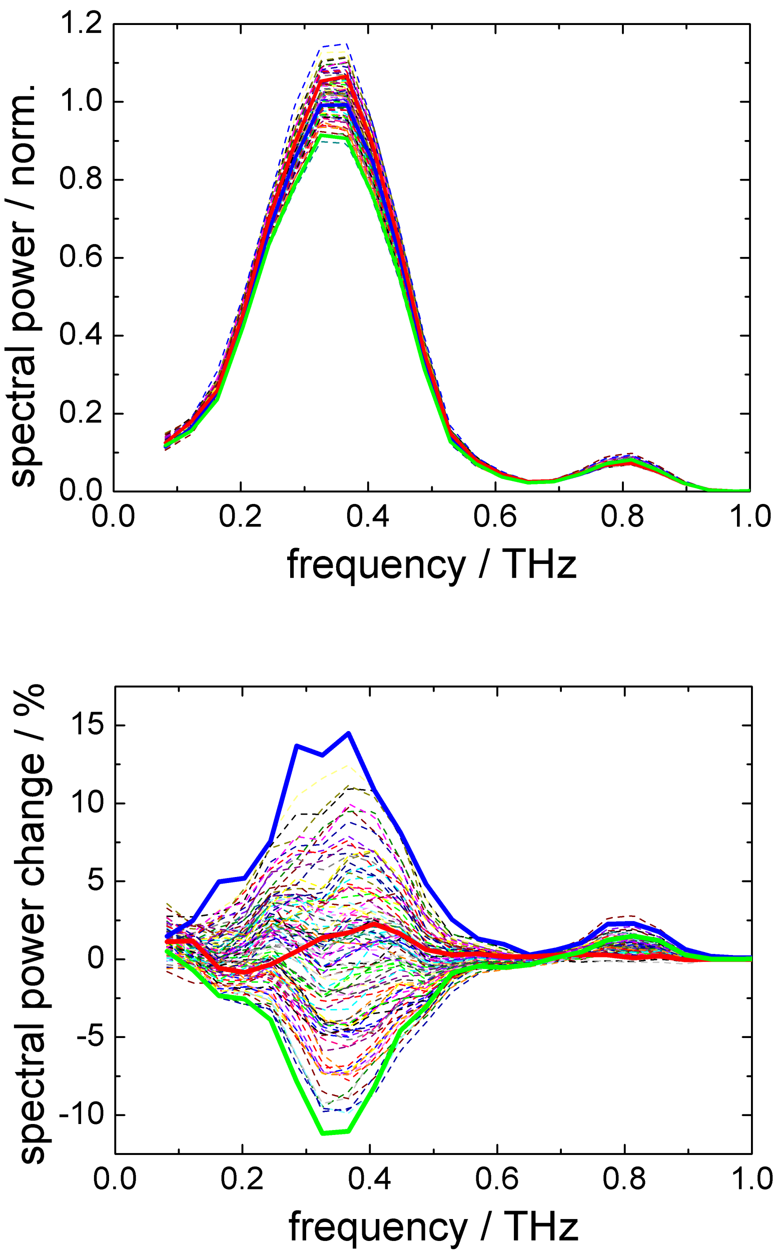

(a)

(b)

Figure B.3: (a) Spectra from selected CDR pulses used in the arrivaltime monitor, taken over 1 second. Most changes are in intensity, with the overall shape of the spectrum remaining stable. (b) Difference spectra to illustrate the changes in CDR spectrum over a period of 1 second.

Freq. (Hz)	CDR intensity	Undulator intensity	CDR Arrivaltime	BAM
260				+++
950			+	
7600				+
8900			+++	
10900				+
13969			+++	
16300				++
16564			+	
17100				++
17801			+++	
19036			+	
19500				++
21633			-	
25400				++
26701			+++	
27583			+	
27685			+	
27938			+++	
28955			+	
31300				++
32900				+
33800				++
34600				++
35602			+++	
36399			++	
36838			+	
39000				+
39435			+	
40670			++	
41782			+++	
41907			+++	
42031			+	
42200				+++
43200				++
43612			+	
43775			+	
44503			+++	
46500				+

Freq. (Hz)	CDR intensity	Undulator intensity	CDR Arrivaltime	BAM
46974			+++	
49300				+++

Table B.1: Frequency components only visible in one of the arrivaltime measurements.

Freq. (Hz)	CDR intensity	Undulator intensity	CDR Arrivaltime	BAM
50	+++$^{\#}$	++$^{\#}$		
68	+			
132	+++	++	+	
160	++$^{\#}$	+$^{\#}$		
166	++	++	+	
193	+$^{\#}$	+$^{\#}$		
260				+++
527	+			+++
3634	+			
7600				+
8089		+		
8273	+			
8900			+++	
10900				+
11908	++			
12732			+	+(12.8kHz)
13969			+++	
14312	+			
16300				++
16520	+			
16564			+	
17100				++
17801			+++	
18450	+			
19036			+	
19500				++
20401	+		+	
21633			+	
22869			++	++(22.7kHz)
25400				++

Freq. (Hz)	CDR intensity	Undulator intensity	CDR Arrivaltime	BAM
26701			+++	
27450	+			
27583			+	
27685			+	
27938			+++	
28063	+			++(28.1kHz)
28955			+	
28961	++*	+*		
29295	+			
31085	+			
31300				++
32900				+
33800				++
34600				++
35602			+++	
36265		+		
36315	+++*	+*		
36399			++	
36365		+		
36734	+			
36838			+	
39000				+
39435			+	
40670			++	
41782			+++	
41907			+++	
42031			+	
42200				+++
42993	+			
43200				++
43608	++*	+*		
43612			+	
43775			+	
44503			+++	
46500				+
46628	++			
46974			+++	
48250	+			

Freq. (Hz)	CDR intensity	Undulator intensity	CDR Arrivaltime	BAM
49300				+++

Table B.2: Table showing frequencies common across different measurements, between 50 Hz and 50 kHz, with higher harmonixs of 50 Hz removed. The first column is the frequency, followed by columns showing if that frequency is present in the undulator intensity jitter spectrum, the CDR intensity jitter spectrum, the arrivaltime jitter spectrum, and the beam arrivaltime (BAM) measurements. vw=weak, w=weak, m=medium, s=strong, vs=very strong. Mirror frequencies (components that show up because of undersampling of frequencies higher than the Nyquist frequency cutoff) are shown in parentheses with the source. BAM measurements taken from [75]. # These frequencies are out of phase by a factor of pi, implying they come from part of the bunch hitting the DR radiator. * These frequencies are in phase, implying they are caused by some property of the beam, such as changes in beam energy or bunch charge.

Appendix C

Definitions

ADC	analog to digital converter
BPM	beam position monitor
BS	beam splitter
CCD	charge coupled device
CDR	coherent diffraction radiator
CEP	carrier-envelope phase
CTR	coherent transition radiator
cw	continuous wave
DC	direct current
DESY	Deutsches Elektronen-Synchrotron
EO	electro-optic
EOS	electro-optic sampling
FWHM	full width half maximum
fs	femtosecond
GeV	giga electron volt
GHz	gigahertz
GUI	graphical user interface
GVM	group velocity mismatch
HWP	half-wave plate
HZDR	Helmholtz-Zentrum Dresden-Rossendorf
kHz	kilohertz
MeV	mega electron volt
nC	nano Coulomb
pC	pico Coulomb
ps	picosecond
QWP	quarter-wave plate
quasi-cw	quasi-continuous wave
RF	radio frequency
RMS	root mean square
S/N	signal to noise
SRW	Synchrotron Radiation Workshop
THz	terahertz
μm	micrometer

Bibliography

[1] S. S. Dhillon et al. The 2017 terahertz science and technology roadmap. *J. Phys. D: Appl. Phys.*, 50:043001, 2017.

[2] C. A. Schmuttenmaer. Exploring dynamics in the far-infrared with terahertz spectroscopy. *Chem. Rev.*, 104:1759, 2004.

[3] T. Kampfrath, K. Tanaka, and K. A. Nelson. Resonant and nonresonant control over matter and light by intense terahertz transients. *Nat. Photon.*, 7: 680, 2013.

[4] N. Stojanovic and M. Drescher. Accelerator- and laser-based sources of high-field terahertz pulses. *J. Phys. B*, 46:192001, 2013.

[5] Z. Wu et al. Intense terahertz pulses from slac electron beams using coherent transition radiation. *Rev. Sci. Instr.*, 84:022701, 2013.

[6] B. Green et al. High-field high-repetition-rate sources for the coherent THz control of matter. *Sci. Rep.*, 6:22256, 2016.

[7] S. Kovalev et al. Probing ultra-fast processes with high dynamic range at 4th-generation light sources. *Struct. Dyn.*, 4:024301, 2017.

[8] B. Aune et al. Superconducting TESLA cavities. *Phys. Rev. ST AB*, 3: 092001, 2000.

[9] X. Ding and S. Boucher. A method for establishing Q-factors of RF cavities. *Proceedings of IPAC '10, Kyoto, Japan*, page 3789, 2010.

[10] Mitsubishi Heavy Industries. Mitsubishi heavy industries' normal conducting/superconducting accelerating cavities - contributing to the development of highly-advanced particle accelerator systems. *Mitsubishi Heavy Industries Technical Review*, 53:25, 2016.

[11] H. Padamsee. *RF Superconductivity*. Wiley-VCH, first edition, 2009.

[12] F. Loehl et al. Electron bunch timing with femtosecond precision in a superconducting free-electron laser. *Phys. Rev. Lett*, 104:144801, 2010.

[13] S. Schulz et al. Femtosecond all-optical synchronization of an X-ray free-electron laser. *Nucl. Instr. Meth. Phys. Res. A*, 507:354, 2003.

[14] W. Wuensch et al. A demonstration of high-gradient acceleration. *Proceedings of the 2003 Particle Accelerator Conference*, page 495, 2003.

[15] J. Teichert et al. Results of beam parameter measurement of the ELBE electron accelerator after commissioning. *Nucl. Instr. Meth. Phys. Res. A*, 507: 354, 2003.

[16] P. Michel et al. The Rossendorf IR-FEL ELBE. *Proceedings of FEL 2006*, page 488, 2006.

[17] R. Krause-Rehberg et al. EPOS - an intense positron beam project at the ELBE radiation source in rossendorf. *Appl. Surf. Sci.*, 252:3106, 2006.

[18] E. Altstadt et al. A photo-neutron source for time-of-flight measurements at the radiation source elbe. *Ann. Nucl. Energy*, 34:36, 2007.

[19] R. Schwengner et al. The photon-scattering facility at the superconducting electron accelerator elbe. *Nucl. Instr. Meth. Phys. Res. A*, 555:211, 2005.

[20] F. Gabriel et al. The Rossendorf radiation source ELBE and its FEL projects. *Nucl. Instr. Meth. Phys. Res. B*, 161:1143, 2000.

[21] M. Kuntzsch/HZDR. private communication, 2016.

[22] CPI. Electron sources, 2016. URL `http://www.cpii.com/docs/datasheets/131/Electron%20Guns%20Data%20Sheet6.pdf`.

[23] ELBE. Pulsed injector, 2016. URL `https://www.hzdr.de/db/Cms?pNid=971`.

[24] H. Buettig/HZDR. private communication, 2016.

[25] H. Buettig et al. RF power upgrade at the superconducting 1.3 GHz CW LINAC ELBE with solid state amplifiers. *Nucl. Instr. Meth. Phys. Res. A*, 704:7–13, 2013.

[26] Libera. Performance, Reliability, Cost Effectiveness = Libera Spark, 2016. URL `http://www.i-tech.si/announcements/performance-reliability-cost-effectiveness--libera-spark`.

[27] S. Casalbuoni, B. Schmidt, and P. Schmüser. Far-infrared transition and diffraction radiation. *TESLA Report 2005-15*, 2005.

[28] U. Lehnert/HZDR. private communication, 2016.

[29] G.L. Carr et al. High-power terahertz radiation from relativistic electrons. *Nature*, 420:153–156, 2002.

[30] V. Ginzburg and I. Frank. Radiation of a uniformly moving electron due to its transition from one medium into another. *Zhurnal Eksperimentalnoi I Teoreticheskoi Fiziki*, 16:15, 1946.

[31] M. Castellano, A. Cianchi, G. Orlandi, and V.A. Verzilov. Effects of diffraction and target finite size on coherent transition radiation spectra in bunch length measurements. *Nucl. Instr. Meth. Phys. Res. A*, 435:297, 1999.

[32] V. Ginzburg. *Bull. Acad. Sci. U.S.S.R. Sér. Phys.*, 11:165, 1947.

[33] F. R. Elder et al. Radiation from electrons in a synchrotron. *Phys. Rev.*, 71: 829, 1947.

[34] H. Motz, W. Thon, and R.N. Whitehurst. Experiments on radiation by fast electron beams. *J. Appl. Phys.*, 24:826, 1953.

[35] H. Wiedemann. *Particle Accelerator Physics*. Springer, third edition, 2007.

[36] K-J Kim. Characteristics of synchrotron radiation. *AIP Conf. Proc.*, 184: 565, 1989.

[37] E. R. Caley and J. F. C. Richards. *Theophrastus: On Stones*. Ohio State University Press, 1 edition, 2016.

[38] D. Brewster. Observations of the pyro-electricity of minerals. *The Edinburgh Journal of Science*, 1:208, 1824.

[39] L. D. Landau, E. M. Lifschitz, and L. P. Pitaevski, editors. *Electrodynamics of Continuous Media*. Elsevier, second edition, 2007.

[40] S. Wesch et al. A multi-channel THz and infrared spectrometer for femtosecond electron bunch diagnostics by single-shot spectroscopy of coherent radiation. *Nucl. Instr. Meth. Phys. Res. A*, 665:40, 2012.

[41] DIAS Infrared GmbH. Pyroelectric infrared detectors, 2006. URL `www.dias-infrared.de/pdf/basics_eng.pdf`.

[42] T. Crowe et al. Opening the THz window with integrated diode circuits. *IEEE J. Solid-State Circuits*, 40-10:2104, 2005.

[43] I. Ederra et al. Design and test of a 0.5 THz dipole antenna with integrated schottky diode detector on a high dielectric constant ceramic electromagnetic bandgap substrate. *IEEE Trans. THz Sci. Technol.*, 3-5:584, 2013.

[44] N. Neumann/TU Dresden. private communication, 2016.

[45] M. Schiselski et. al. A planar schottky diode based integrated THz detector for fast electron pulse diagnostics, 2016.

[46] K.-E. Peiponen, J. A. Zeitler, and M. Kuwata-Gonokami, editors. *Terahertz Spectroscopy and Imaging*. Springer, first edition, 2013.

[47] Q. Wu and X.-C. Zhang. Ultra fast electro-optic field sensors. *Appl. Phys. Lett.*, 68:1604, 1996.

[48] P. Planken. Measurement and calculation of the orientation dependence of terahertz pulse detection in ZnTe. *J. Opt. Soc. Am. B*, 18:313, 2001.

[49] Z. Jiang and X.-C. Zhang. Measurement of spatio-temporal terahertz field distribution by using chirped pulse technology. *IEEE J. Quant. Electron.*, 36:1214, 2000.

[50] Ophir Optics. Ophir optics pyrocam 3, 2016. URL `http://www.ophiropt.com/laser--measurement/beam-profilers/products/Beam-Profiling/Camera-Profiling-with-BeamGage/Pyrocam-IIIHR`.

[51] A. Steiger et al. Traceable THz power measurement from 1 THz to 5 THz. *Opt. Express*, 21:14466, 2013.

[52] Ophir Optics. Laser power sensors introduction, 2016. URL `http://www.ophiropt.com/laser-measurement-instruments/laser-power-energy-meters/tutorial/thermal-sensors`.

[53] B. Schmidt/DESY. private communication, 2016.

[54] F. Loehl et al. High bandwidth pickup design for bunch arrival-time monitors for free-electron laser. *Phys. Rev. Lett.*, 104:144801, 2010.

[55] F. Tavella, N. Stojanovic, G. Geloni, and M. Gensch. Few-femtosecond timing at fourth-generation X-ray light sources. *Nat. Photon.*, 5:162, 2011.

[56] J. Shan et. al. Single-shot measurement of terahertz electromagnetic pulses by use of electro-optic sampling. *Opt. Lett.*, 25-6:426, 2000.

[57] Coherent. RegA Data Sheet, 2016. URL `https://cohrcdn.azureedge.net/assets/pdf/RegA-Data-Sheet.pdf#page=1`.

[58] Coherent. Coherent, 2016. URL `https://www.coherent.com/`.

[59] Coherent. Synchrolock-AP, 2016. URL `https://www.coherent.com/lasers/laser/ultrafast-oscillator-accessories/synchrolock-ap`.

[60] S. Kovalev/HZDR. private communication, 2016.

[61] M. J. Rosker, M. Dantus, and A. H. Zewail. Femtosecond real-time probing of reactions. I. the technique. *J. Chem. Phys.*, 89:6113, 1988.

[62] U. Fruehling et al. Single-shot terahertz-field-driven X-ray streak camera. *Nat. Photon.*, 3:523, 2009.

[63] W. Withayachumnankul and M. J. Naftaly. Fundamentals of measurement in terahertz time-domain spectroscopy. *J. Infrared Millim. Terahertz Waves*, 35:610, 2014.

[64] O. Chubar, P. Elleaume, and A. Snigirev. Phase analysis and focusing of synchrotron radiation. *Nucl. Instr. Meth. Phys. Res. A*, 435:495, 1999.

[65] M. Gensch. Superradiant linac-based THz sources in 2013. *Proceedings of FEL2013*, 2013.

[66] D. Suetterlin et al. An analytic formalism for the emission of coherent transition radiation from an oblique finite thin metallic target screen. *Nucl. Instr. Meth. Phys. Res. B*, 264:361, 2007.

[67] M. Schwarz et al. Comparison of various sources of coherent THz radiation at FLUTE. *Proceedings of IPAC 2012*, page 568, 2012.

[68] H. Nyquist. Certain factors affecting telegraph speed. *Bell System Technical Journal*, 3:324, 1924.

[69] W. S. Fann et al. Direct measurement of nonequilibrium electron-energy distributions in subpicosecond laser-heated gold films. *Phys. Rev. Lett.*, 68:2834, 1992.

[70] F. Kuschewski. Optical nanoscopy of transient states in condensed matter. *Sci. Rep.*, 5:12582, 2015.

[71] N. Awari et al. Narrow-band tunable terahertz emission from ferrimagnetic Mn3-xGa thin films. *Appl. Phys. Lett.*, 109:032403, 2016.

[72] Z. Jin et al. Single-pulse terahertz coherent control of spin resonance in the canted antiferromagnet YFeO3, mediated by dielectric anisotropy. *Phys. Rev. B*, 87:094422, 2013.

[73] P. Lu. *Optimization of an SRF Gun for High Bunch Charge Applications at ELBE*. PhD thesis, Technisch Universität Dresden, 2017.

[74] U. Lehnert/HZDR. private communication, 2011.

[75] M. Kuntzsch. *Optische Synchronisation am CW-Beschleuniger ELBE*. PhD thesis, Technisch Universität Dresden, 2015.

[76] P. Murcek et al. The SRF photo injector at ELBE - design and status 2013. *Proceedings of SRF2013*, page 148, 2013.

[77] Princeton Instruments. High-performance imaging spectrographs and scanning monochromators, 2016. URL `http://www.princetoninstruments.com/products/SpectraPro`.

[78] Basler. spL4096-140km, 2016. URL `http://www.baslerweb.com/en/products/cameras/line-scan-cameras/sprint/spl4096-140km`.

[79] L. Rota et al. KALYPSO: A linear array detector for visible to NIR radiation. *Proceedings of IBIC2016*, page 740, 2016.

[80] D. Jones et al. Carrier-envelope phase control of femtosecond mode-locked lasers and direct optical frequency synthesis. *Science*, 288:635, 2000.

Acknowledgments

This thesis encompassed a lot of life-changing events for me. It all started after an international move to a place where I didn't speak the language (and still only barely do, sorry guys). The birth of my son, Marcus, and later the birth of my daughter Ilona. The loss of two cats, my cat Boots who had been with me for 15 years, and my wife's cat Shira, show had been with her for 12 years. I became a godfather to a wonderful little boy, Felix Steinbrück, who I will hopefully get to see more often once this is all finished.

I would first like to thank my ever-patient wife Liz. During the course of this thesis she would often take the kids on trips or wake up with them at night so I would have a chance to work. Without her support I never would have been able to finish.

I would also like to thank my group. Dr. Sergey Kovalev with whom I worked closely to develop the data acquisition and data analysis systems. He provided a lot of expertise on electro-optic sampling and spectral decoding. We also spent many frustrating and fruitful night shifts performing experiments, rewriting software, and aligning lasers. Dr. Jan-Christoph Deinert, who although he showed up towards the end still provided valuable advice for writing. Nilesh Awari and Min Chen, my fellow students in the group who will soon be defending their own theses.

Coworkers at ELBE also provided help and support. Special thanks to Reinhard Steinbrück, who provided not only advice on LabVIEW programming and hardware acquisition but also friendship. Dr. Ulf Lehnert, who provided much valuable information on the ELBE accelerator. Dr. Hartmut Büttig for providing books, papers, and occasional custom hardware as well as being one of the friendliest people I know. Dr. Michal Kuntzsch, whose valuable work and advice on synchronization with the ELBE timing distribution system helped make the arrivaltime monitor possible. Petra Neumann, who put up with my constant questions and inability to properly fill out all types of paperwork. Hannes Vennekate for being helpful and friendly and always having time for a chat about America. Dr. Michael Klopf, for providing wonderful advice and a whole slew of papers and references.

I’d also like to thank the FLASH crew, for hosting me during beamtimes as well as coming to help with beamtimes here: Torsten Golz and Nikola Stojanovic especially.

Thanks go to many other outside collaborators as well. Dr. Nicole Hiller from KIT for being my go-to for any questions regarding thesis writing and near-field electro-optic sampling. Dr. Markus Schwarz, also from KIT, for working with me on simulations and analytical calculations. Dr. Gianluca Geloni from European XFEL and Dr. Vivek Asgekar, visiting us from India, for all their help with undulator simulations and explanations about the SRW software package. Special thanks also go to Dr. Alan Fisher of SLAC, for his help with CDR and CTR simulations as well as inviting me on a fascinating tour of the facilities at SLAC.